博士論文

Effects of Solute Elements in Irradiation Embrittlement of Reactor Pressure Vessel during Long-term Operation

（高経年化した原子炉圧力容器照射脆化における溶質原子の影響）

陳　良

Effects of Solute Elements in Irradiation Embrittlement of Reactor Pressure Vessel during Long-term Operation

CHEN Liang

Supervisor: Prof. SEKIMURA Naoto

Department of Nuclear Engineering and Management

School of Engineering

The University of Tokyo

Abstract

The neutron irradiation embrittlement of reactor pressure vessel steels is an important ageing issue for the safe long-term operation of light water reactors. Structural integrity of the reactor pressure vessel must be demonstrated throughout the entire operating life for normal operation and postulated accident events, notably pressurized thermal shock. This requires prediction of reactor pressure vessel embrittlement based on the understanding of embrittlement mechanisms.

Solute clusters, composed of Cu, Ni, Mn, and Si, are one dominant microstructural feature formed under irradiation which cause hardening and accompanying embrittlement of reactor pressure vessel. The main objective of present study is to understand effects of solute elements, including Ni, Mn, and Si, on formation and growth of solute clusters in reactor pressure vessel. Neutron irradiation following thermal ageing can represent the long-term operation condition for reactor pressure vessel. Considering the interactions of Ni-Mn, Si-Cu, and Si-Ni, the research objectives are categorized as: to study effects of Ni and Mn on nucleation and growth of Cu-rich clusters during neutron irradiation following thermal ageing; to study effect of Si on nucleation and growth of Cu-rich clusters during neutron irradiation following thermal ageing; to study effect of Si on formation of Ni-rich clusters at high dose; to discuss the role of solutes and the embrittlement prediction for long-term operation of reactor pressure vessel.

The model alloys Fe-Cu, Fe-Cu-Ni, Fe-Cu-Ni-Mn, and Fe-Cu-Si were prepared for

neutron irradiation following thermal ageing experiments. Additionally, high dose ion irradiation experiment was carried out on the model alloy Fe-Ni-Si. For the alloys, the microstructural analysis was conducted using atom probe tomography. The major conclusions are as follows:

(1) Mn is found to be critical for the formation of Cu-rich clusters. The addition of Mn to Fe-Cu-Ni reduced the ageing time required to achieve a similar microstructure of Cu-rich clusters from 225 to 90 h. This indicates that Mn can accelerate solute diffusion through thermal vacancies, thus accelerating kinetic process of solute clustering. Different from thermal ageing condition, Mn significantly increased the number density of Cu-rich clusters under the neutron irradiation. It is suggested that Mn may enhance the heterogeneous nucleation of Cu because of its strong interaction with self-interstitial atoms.

(2) A strong thermodynamic relationship between Ni and Mn is found. In the alloys Fe-Cu-Ni-Mn, an increase of Ni alloying content from 0.6% to 0.8% enhanced the Mn concentration in the clusters as well as the Ni concentration. Moreover, for the alloys Fe-Cu-Ni-Mn with different Ni alloying contents, in the clusters, the concentrations of Ni and Mn exhibited 1:1 relationship. The 1:1 Ni-Mn concentration relationship in the clusters remained unchanged from thermal ageing condition to neutron irradiation condition. These results indicate that the 1:1 Ni-Mn relationship can be thermodynamically favoured. This thermodynamic relationship can serve as a driving force for enhanced concentrations of Ni and Mn in the clusters.

(3) Si atoms hardly cluster with Cu, but largely cluster with Ni. Si may refine Cu clusters into small radius under thermal ageing. Except this, evidence for Si to have effect on nucleation and growth of Cu clusters was not detected. The Si concentration in the

clusters in Fe-Cu-Si was very low, indicating that Si atoms hardly cluster with Cu. However, Si should interact with Ni to form high number density of Ni-Si clusters in Fe-Ni-Si.

(4) The role of solutes and the embrittlement prediction for long-term operation of reactor pressure vessel are discussed. The mechanisms found in the present study are represented using prediction formulas. To sophisticate the prediction formulas including fitting parameters, APT database is proposed. Suggestions for future studies are also provided based on the present study.

Table of contents

Chapter 1 Introduction

1.1 Background

Nuclear generated electricity is a source of low-carbon emissions. There are now 449 nuclear power reactors with a total net installed capacity of over 390000 MW in operation in 4 regions, Africa, America, Asia and Europe, and 60 nuclear power reactors under construction [1-1]. Fig. 1.1 shows the operational nuclear power reactors by age [1-1]. Of these 449 nuclear reactors in operation, 270 reactors have been in operation for more than 30 years.

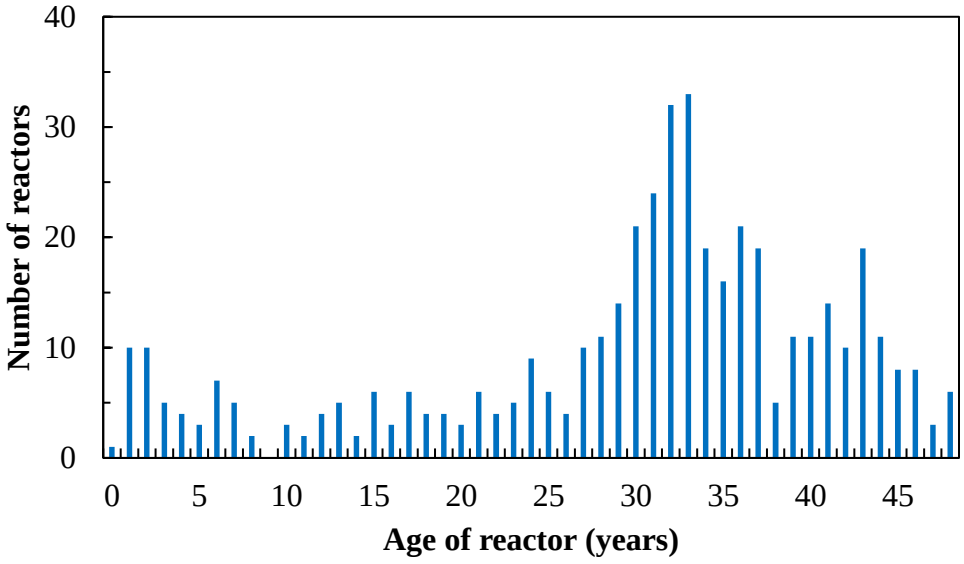

Fig. 1.1 Operational nuclear power reactors by age [1-1]

A specific design basis life was set for the reactors, such as 40 years in Japan and the US. The original design life was determined generally based on fatigue usage calculations rather than material degradation studies. Plant life extension beyond the design life is very attractive to utilities based on technical and economic considerations, and the long-term operation (LTO) strategy of the nuclear power plant (NPP) has been accepted in many

countries.

The reactor pressure vessel (RPV) is the highest priority key component in the NPP aside from the reactor core. The RPV has direct safety significance for confining radioactive materials inside the boundary, and is considered irreplaceable as the replacement will require an extraordinary amount of time and money. The toughness properties of the RPV material are known to degrade during operation because of the neutron irradiation embrittlement, which can lead to safety concerns. For example, a massive failure of the RPV by rupture or brittle fracture of critically sized flaws could seriously damage the reactor core. Structural integrity of the RPV is maintained as long as the RPV materials in the most sensitive location, the beltline region near the reactor core, have adequate fracture toughness. For the safe LTO, structural integrity of the RPV must be demonstrated throughout the entire operating life for normal operation and postulated accident events, notably pressurized thermal shock (PTS). The probabilistic analysis approach for PTS evaluation needs accurate prediction of neutron irradiation embrittlement of the RPV so as to reduce the uncertainties and improve the efficiency in processing plant life extension requests.

The existing embrittlement predictive methods can well predict the RPV embrittlement up to the end of design life. Nonetheless, direct extrapolation of the methods to LTO condition may not be reliable, as they were generally fitted to the surveillance database containing little high neutron fluence data, pertinent to LTO condition. For example, Fig. 1.2 shows the expansion of the range of the residuals when the RPV embrittlement predictions are compared with the data in M. Kirk's Wide-Ranging Database [1-2]. The

expansion in the range of the residuals is enlarged at the higher neutron fluences. In view of improving the predictive capability of embrittlement predictive methods with limited high fluence surveillance data, it is therefore necessary to understand better irradiation embrittlement mechanisms of the RPV.

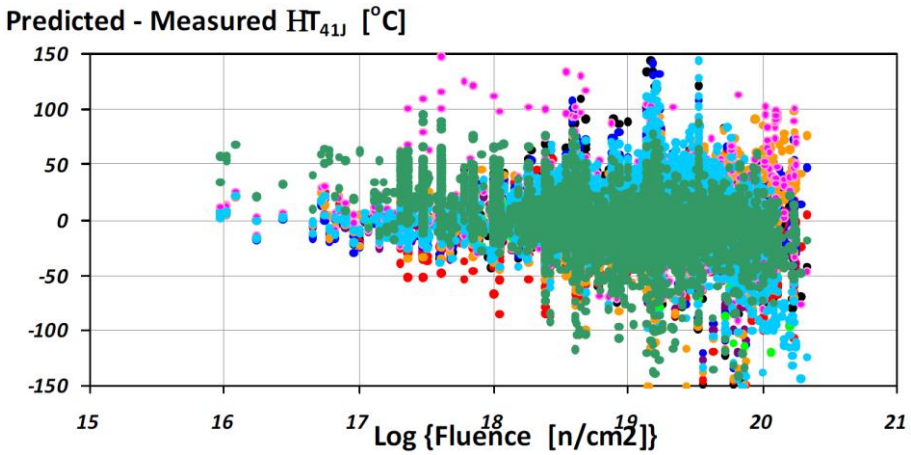

Fig. 1.2 Expansion of the range of the residuals when the RPV embrittlement predictions are compared with the data in M. Kirk's Wide-Ranging Database (Different colored points refer to the residuals produced by applying different embrittlement predictive methods) [1-2].

1.2 Reactor pressure vessel

Large and integrated RPV components have been developed for increased unit capacity, improved safety and reliability, decreased in-service inspection and shortened construction period. High-quality RPV material requires homogeneity, no harmful internal defects, good fracture toughness, low embrittlement susceptibility, good inspectability, weldability, etc. Because of the continuously improved RPV design and

structural integrity approaches, there have not been any RPV failures.

1.2.1 Features of reactor pressure vessel

The examples of the RPVs in pressurized water reactors (PWR) and boiling water reactors (BWR), and their relative sizes are presented in Fig. 1.3 [1-3]. The differences in size between the RPVs of PWR and BWR are primarily because the BWR has a larger core and a steam drying equipment is installed at the top of the RPV of BWR. For example, for a 1065 MW BWR RPV, the height is about 22 m, and the inside diameter is 6.4 m; the typical PWR RPV is about 13.5 m in height and has an inside dimeter of 4.4 m. The thickness of the RPV is chosen based on the requirements on the stress in the RPV wall. The PWR RPV has typically a thickness of about 20-25 cm, while the BWR RPV has typically about 15 cm thickness.

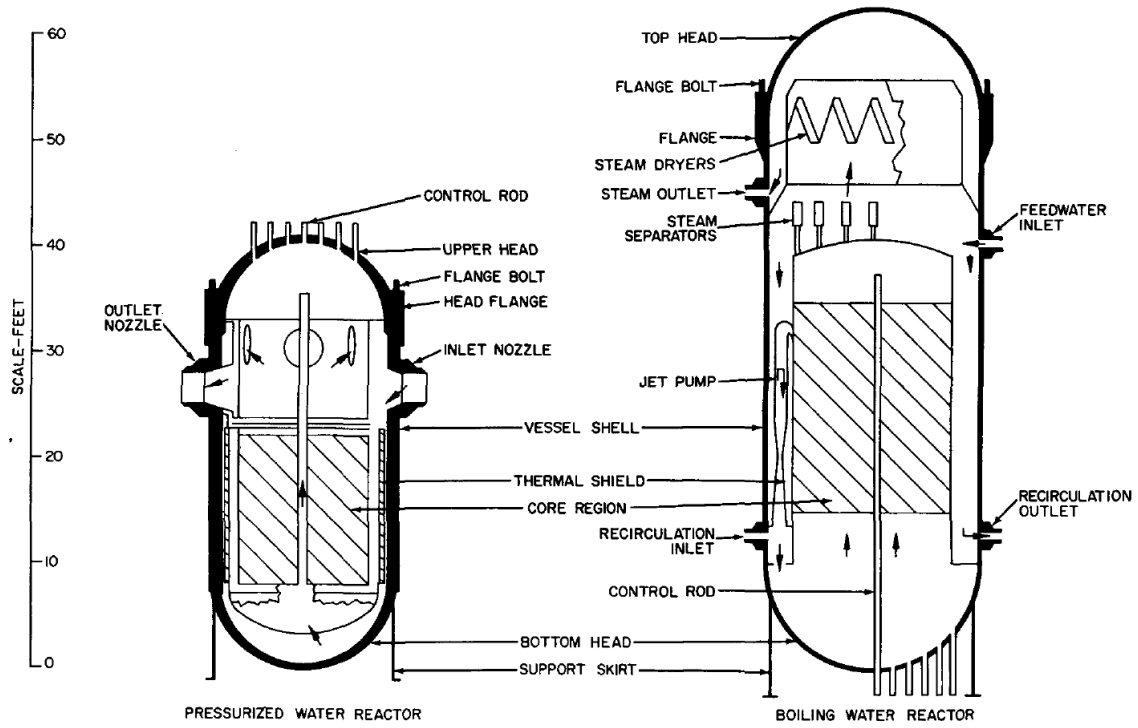

Fig. 1.3 Schematic diagram of the RPVs of PWR and BWR showing relative size [1-3]

1.2.2 Materials for reactor pressure vessel

The materials used for the RPVs developed to attain the safety and reliability as the reactor technology evolved. For example, SA-302 Grade B, is a Mn-Mo steel for plate materials which was used in the quenched and tempered condition for a lot of earlier RPVs made through the mid-1960s. As the commercial nuclear power evolved, the RPVs were required to be larger in size and wall thickness. A RPV material with greater hardenability was necessary. The addition of 0.4-0.7wt.% Ni to SA-302 Grade B provided the required increased hardenability across the entire wall thickness, and this steel was initially known as SA-302 Grade B Modified. Later, it became the designation SA533 Grade B Class 1 and was widely used in the quenched and tempered condition. The forging steels have also developed since the mid-1950s. For example, the Mn-Mo-Ni forging steel, SA-182 F1 Modified was used in the quenched and tempered condition mostly for flanges and nozzles in the 1950s and 1960s. Another forging steel used then was a C-Mn-Mo steel, SA-336F1 which was used both in the normalized and tempered condition and in the quenched and tempered condition. However, large forgings of these materials required cumbersome and expensive heat treatment to reduce H blistering. These steels were eventually replaced with SA 508 Class 2. This steel has been extensively used in the quenched and tempered condition for flanges, nozzles, and ring forgings.

Although many materials are acceptable for the RPVs according to the American Society of Mechanical Engineers (ASME) Code, the basic materials which are now acceptable in the US for most RPVs are limited to SA533 Grade B Class 1, SA 508 Class 2, and SA 508 Class 3, because of special considerations of facture toughness and radiation effects.

In Japan, the plate steel, Japanese Industrial Standards (JIS) G 3120 SQV2A which is equivalent to SA533 Grade B Class 1, is now applied in the in the quenched and tempered condition; the forging steel, JIS G 3204 SFVQ1A which is equivalent to SA 508 Class 3, is now applied. Table 1.1 shows the specifications of the chemical compositions and the mechanical properties of SA533 Grade B Class 1, SA 508 Class 2, SA 508 Class 3, SQV2A, and SFVQ1A [1-4,5].

Table 1.1 Specification of the chemical compositions and the mechanical properties of RPV steels [1-4,5]

Designation	Chemical composition (wt.%)								
	C	Si	Mn	P	S	Ni	Mo	Cr	V
ASME SA533B-1	max 0.25	0.15/0.40	1.15/1.50	max 0.035	max 0.040	0.40/0.70	0.45/0.60		
ASME SA508-2	max 0.27	0.15/0.40	0.50/1.00	max 0.015	max 0.015	0.50/1.00	0.55/0.70	0.25/0.45	max 0.05
ASME SA508-3	max 0.25	0.15/0.40	1.20/1.50	max 0.015	max 0.015	0.40/1.00	0.45/0.60	max 0.25	max 0.05
JIS SQV2A	max 0.25	0.15/0.30	1.15/1.50	max 0.035	max 0.040	0.40/0.70	0.45/0.60		
JIS SFVQ1A	max 0.25	max 0.40	1.20/1.50	max 0.030	max 0.030	0.40/1.00	0.45/0.60	max 0.25	max 0.05

Table 1.1 (continued)

Designation	Yield strength (N/mm^2)	Tensile strength (N/mm^2)	Elongation (%)	Reduction of area (%)
ASME SA533B-1	min 345	550/690	min 18	
ASME SA508-2	min 345	550/725	min 18	min 38
ASME SA508-3	min 345	550/725	min 18	min 38
JIS SQV2A	min 345	550/690	min 18	
JIS SFVQ1A	min 345	550/730	min 16	min 38

The RPVs in the operating NPPs which were made before the early 1970s have relatively high or medium levels of impurity elements, such as Cu and P. The impurity Cu is a harmful element in terms of the degradation of RPV material toughness properties. For example, Fig. 1.4 presents the trend of the Cu content in the RPV steels which were used for the belt-line region materials in Japan [1-5]. The Cu content in the RPVs was greatly reduced in the late 1970s, when the effect of Cu was identified. Regarding the RPVs which were fabricated after the late 1980s, their Cu content is at very low level (less than 0.05wt.%).

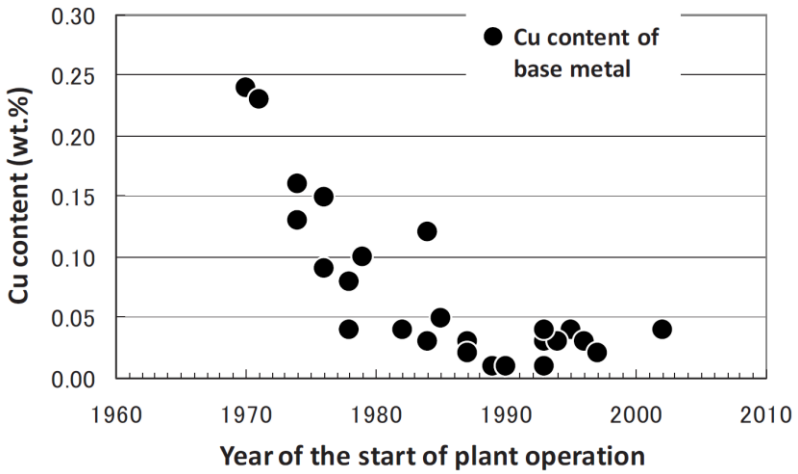

Fig. 1.4 Trend of the Cu content in Japanese RPV steels [1-5]

1.3 Integrity and embrittlement of reactor pressure vessel

The safe operation of RPV is based on maintaining the structural integrity of the RPV and the associated primary pressure boundary system. The structural integrity needs to be periodically assessed as the RPV fracture toughness changes during operation because of the neutron irradiation embrittlement. The RPV surveillance programs are designed to

monitor the changes in toughness properties through the use of small specimens, typically 10 mm square Charpy V-notch (CVN). The CVN test is historically specified as an indirect indexing method for the fracture toughness. The shift in the CVN energy curve was found to be approximately equal to the shift in the fracture toughness curve in terms of neutron irradiation embrittlement [1-6]. Fig. 1.5 shows the CVN energy curve for an unirradiated RPV steel (blue) and irradiated one (red) [1-7]. In the past three decades, direct measurement of the fracture toughness of small irradiated surveillance specimens becomes also possible through an analytical approach developed for ferritic steels, the master curve fracture toughness approach [1-8].

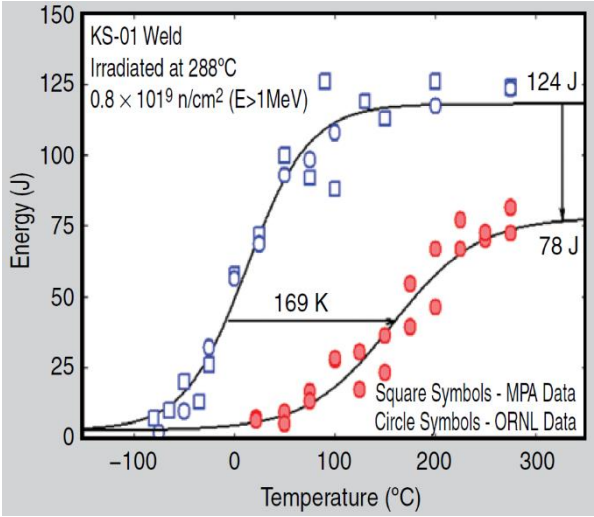

Fig. 1.5 CVN energy curve for an unirradiated RPV steel and irradiated one [1-7]

1.3.1 Fracture toughness of reactor pressure vessel

The fracture toughness of the material, K_{Ic} is a measure of its resistance to failure in the presence of a flaw (or crack) with known or presumed size and a stress which is known or presumed [1-9]. It depends on the temperature T, and the reference transition

temperature TT_{ref}:

$$K_{Ic} = A + B\exp\left[C\left(T - TT_{ref}\right)\right] \quad (1.1)$$

where A is the lower shelf asymptote, B and C are parameters which define the curve shape. The indexing approaches of TT_{ref} differ among the countries. In the US, TT_{ref} is defined as the reference temperature for nil ductility transition (NDT), RT_{NDT}. The initial non-irradiated value of RT_{NDT} is defined in the ASME Code Section III and is determined through the drop weight tests. The irradiated value of RT_{NDT} is defined as:

$$\text{irradiated } RT_{NDT} = \text{initial } RT_{NDT} + \Delta T_{41J} \quad (1.2)$$

where ΔT_{41J} is the shift in transition temperature because of neutron irradiation embrittlement, and is measured at 41 J for the CVN test. The adjusted reference temperature, ART for the temperature indexing is then defined as:

$$ART = \text{irradiated } RT_{NDT} + \text{margin} = \text{initial } RT_{NDT} + \Delta T_{41J} + \text{margin} \quad (1.3)$$

where the margin is to account for the uncertainties in ΔT_{41J} and initial RT_{NDT}, and to provide regulatory comfort. The master curve approach provides an alternative to ΔT_{41J} and is allowed in the ASME code. The reference temperature RT_{T0} is defined using the temperature T_0 at the 100 MPa $m^{1/2}$ fracture toughness level, as:

$$RT_{T_0} = T_0 + 19.4℃ \quad (1.4)$$

The Russian approach [1-10] is different from the US method. In the Russian design code, TT_{ref} is defined through the direct measurement of irradiated T_{KF} which is defined as the temperature at a designated CVN energy level that depends on yield strength in the irradiated condition. In France, RT_{NDT} is used as the indicator of the fracture toughness reference temperature but an ISO Charpy testing standard is used instead of the ASTM standard [1-11]. The Japanese approach [1-12] is similar to the US method using the same

definition of RT_{NDT} as in the ASME Code, and the Germany approach [1-13] is the same as the US method.

1.3.2 Methods for predicting irradiation embrittlement

The shift in transition temperature of fracture toughness, as a measure of the neutron irradiation embrittlement, is generally predicted through the correlations of CVN transition temperature shifts measured in surveillance specimens with various material variables (e.g., chemical composition) and irradiation variables (e.g., fluence). Empirical methods generally predict the embrittlement as a product of a chemistry factor, *CF*, and a fluence factor, *FF*. The formulas have been developed using relatively simple equations with the help of statistical analysis results of the surveillance database and the test reactor database. The embrittlement of RPVs is known to be sensitive to many parameters, such as Cu content, Ni content, Mn content, flux, temperature, and fluence. To accurately predict the long-term integrity of RPVs, it is necessary to use predictive methods considering various parameters and the microstructures which result in the embrittlement based on physical mechanisms. Fig. 1.6 illustrates the development of embrittlement predictive methods [1-9]. The embrittlement predictive methods are very roughly divided into two categories: statistically based methods (the empirical methods as mentioned above), and mechanism guided methods.

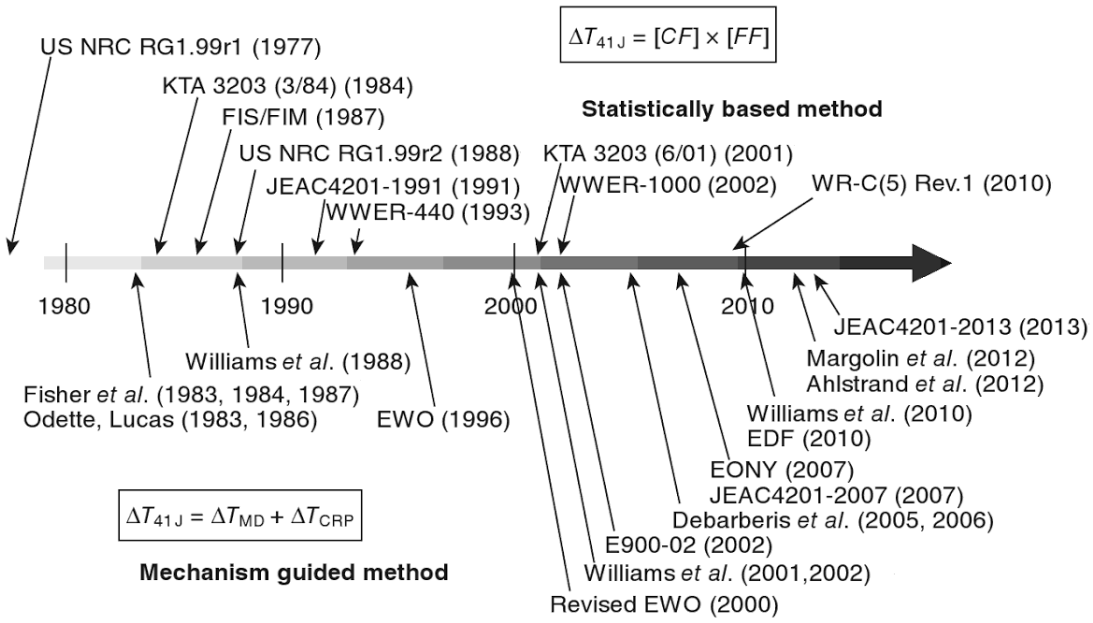

Fig. 1.6 Development of embrittlement predictive methods [1-9]

In Japan, the new embrittlement correlation method, Japan Electric Association Code JEAC4201-2013 is developed based on mechanism guided concept and provides a prediction for the CVN transition temperature shifts ΔT_{41J} using a two-stage model [1-14]. First, the changes in microstructures, including solute atom clusters and matrix damage, under neutron irradiation in the RPV materials are simulated using a set of rate equations; second, the total embrittlement ΔT_{41J} is determined from the microstructures.

The rate equations that describe the microstructures are defined as:

$$\begin{aligned}
\frac{\partial C_{SC}}{\partial t} &= \frac{\partial C_{SC}^{ind}}{\partial t} + \frac{\partial C_{SC}^{enh}}{\partial t} \\
&= \xi_4 \cdot \left((C_{Cu}^{mat} + \xi_1) \cdot D_{Cu} + \xi_2\right) \cdot C_{MD} + \xi_9 \cdot (C_{Cu}^{avail} \cdot D_{Cu} \cdot (1 + \xi_8 \cdot C_{Ni}^0))^2 \\
\frac{\partial C_{MD}}{\partial t} &= \xi_5 \cdot F_t^2 \cdot (\xi_6 + \xi_7 \cdot C_{Ni}^0)^2 \cdot \phi - \frac{\partial C_{SC}^{ind}}{\partial t} \\
\frac{\partial C_{Cu}^{mat}}{\partial t} &= -\upsilon_{SC} \cdot \frac{\partial C_{SC}^{enh}}{\partial t} - \upsilon'_{SC} \cdot C_{SC} \\
\upsilon_{SC} &= \xi_2 \cdot (C_{Cu}^{avail} \cdot D_{Cu})^2 \cdot t_r \\
\upsilon'_{SC} &= \xi_1 \cdot C_{Cu}^{avail} \cdot D_{Cu} \\
F_t &= 1.869 - 4.57 \times 10^{-3} T \\
D_{Cu} &= D_{Cu}^{thermal} + D_{Cu}^{irrad} = D_{Cu}^{thermal} + \mu \cdot \phi^{\alpha} \\
C_{Cu}^{avail} &= max(0, C_{Cu}^{mat} - C_{Cu}^{sol})
\end{aligned} \tag{1.5}$$

where, C_{SC} is the number density of solute atom clusters, C_{MD} is the number density of matrix damage, C_{Cu}^{mat} is the matrix Cu content, C_{Cu}^{sol} is the Cu solubility limit, C_{Ni}^0 is the bulk Ni content, D_{Cu} is a parameter which models the diffusivity of Cu, ϕ is the neutron flux, T is the irradiation temperature, and t_r is the relaxation time. The coefficients in the equations are optimized using Japanese surveillance database.

Regarding the solute atom clusters, C_{SC} is defined as

$$C_{SC} = C_{SC}^{ind} + C_{SC}^{enh} \tag{1.6}$$

where C_{SC}^{ind} is the number density of the clusters through heterogeneous formation induced by neutron irradiation, and C_{SC}^{enh} is the number density of the Cu-rich clusters which are formed by thermodynamic precipitation mechanism and are enhanced by excess vacancies. C_{SC}^{ind} increases with the bulk Cu content and is expressed using a

product of the diffusivity and the matrix damage since the irradiation induced clustering is attributed to solute segregation to the matrix damage [1-15]. For the term C_{SC}^{enh}, the synergistic effect of Cu and Ni is reflected. Regarding the matrix damage, it is primarily relevant to point defect clusters. C_{MD} increases with the bulk Ni content since Ni increases the number density of dislocation loops [1-15]. Meanwhile, part of the matrix damage is consumed as nuclei of the irradiation induced solute atom clusters. In this model, the Cu diffusivity D_{Cu} depends on thermal vacancies and irradiation vacancies. The contribution of the irradiation vacancies D_{Cu}^{irrad} is an exponent function of neutron flux with an exponent less than one since the diffusivity decreases at very high flux levels because of intercascade interaction.

The relationship between the microstructures and the embrittlement ΔT_{41J} is defined as:

$$\begin{aligned}
\Delta T_{SC} &= \xi_{17} \cdot \sqrt{V_f} = \xi_{17} \cdot \sqrt{\xi_{16} \cdot f(C_{Cu}^{mat}, C_{SC}) \cdot g\left(C_{Ni}^{0}\right) + h(\phi t)} \cdot \sqrt{C_{SC}} \\
f(C_{Cu}^{mat}, C_{SC}) &= \xi_{12} \cdot \frac{C_{Cu}^{0} - C_{Cu}^{mat}}{C_{SC}} + \xi_{13} \\
g(C_{Ni}^{0}) &= (1 + \xi_{14} \cdot (C_{Ni}^{0})^{\xi_{15}})^2 \\
h(\phi t) &= \xi_{10} \cdot (1 + \xi_{11} \cdot D_{SC}) \cdot \phi t = \xi_{10} \cdot (1 + \xi_{11} \cdot D_{Cu}) \cdot \phi t \\
\Delta T_{MD} &= \xi_{18} \cdot \sqrt{C_{MD}} \\
\Delta T_{41J} &= \sqrt{(\Delta T_{SC})^2 + (\Delta T_{MD})^2}
\end{aligned} \tag{1.7}$$

The contribution of solute atom clusters to the embrittlement is modelled using the square root of the cluster volume fraction as observed experimentally [1-16]. The cluster volume fraction V_f is determined as a product of the cluster number density C_{SC} and the mean cluster volume that is described with three functions *f*, *g*, and *h*. The function *f* is the mean

Cu amount in the cluster and its product with the function *g* reflects the synergistic effect of Cu and Ni. The function, *h*, which represents cluster growth in size during neutron irradiation, increases with the neutron fluence. The contribution of matrix damage to the embrittlement is modelled using the square root of the matrix damage number density as in a conventional way. Eventually, the total the total embrittlement ΔT_{41J} is determined as the root-sum-square (RSS) of the solute atom clusters contribution and matrix damage contribution.

1.3.3 Pressurized thermal shock

The challenge of pressurized thermal shock (PTS) to the integrity of the RPV is related to the neutron irradiation embrittlement during long-term operation. A PTS event can occur under some accident scenarios in which cold water is introduced into the RPV while the RPV is pressurized. The rapid cooling leads to large thermal stresses, which could result in crack initiation or even failure of an embrittled RPV with high internal pressure. The PTS event is of great importance for safe operation of the PWR. The BWR is not susceptible to the PTS event since the steam in the BWR RPV will condense and reduce internal pressure if cold water is introduced into the RPV. Nonetheless, the BWR may be susceptible to the RPV overpressurization at low temperatures under some conditions.

The integrity methodologies used for assessing PTS are based on either deterministic analyses or probabilistic analyses. Most of methods rely on deterministic analyses and involve complicated fracture mechanics evaluations. In the US approach of 10CFR50.61, a probabilistic fracture mechanics (PFM) analysis is used to define generic screening

criteria that must be met. The generic screening criteria is related to the adjusted reference temperature that is determined at end of operating license life. Alternatively, 10CFR50.61a allows a plant specific probabilistic risk assessment (PRA) and raises effectively the allowable levels of the reference temperature [1-17].

Regarding the RPV integrity, the annual through-wall cracking frequency *TWCF* is employed for risk evaluation and the risk acceptance criterion is defined as (10CFR50.61a):

$$95\%TWCF \leq 10^{-6} \text{ /year} \tag{1.8}$$

where 95%*TWCF* is the 95 percentile of the *TWCF* distribution. For the PTS analysis, the sequences of events related to the RPV failure and their frequencies are determined through PRA analyses. Then, pressure, temperature, heat transfer coefficient histories at the inner surface of RPV are determined from thermal hydraulic analyses for the sequences of events and passed to a PFM model to estimate the driving force to fracture that can be compared to the RPV fracture toughness. This provides estimation of the conditional probability of RPV failure *CPF* and eventually the 95%*TWCF*. Specifically, the Eason-Odette-Nanstad-Yamamoto (EONY) model, a physically-based model for estimating irradiation induced transition temperature shifts ΔT_{41J} is incorporated in the regulation 10CFR50.61a for PTS analysis [1-18].

1.4 Radiation damage in reactor pressure vessel

The RPVs operate at temperatures around 290 °C with pressures ranging from about 7 MPa in the BWR to about 14 MPa in PWR, and are exposed to neutron irradiation with

neutron energies ranging from less than one to several MeV [1-19]. The neutron flux on RPV depends on its distance from reactor core and the reactor type and power. Fig. 1.7 illustrates the maximum neutron fluence, corresponding neutron dose and typical temperature for 40-year operation of RPVs of the BWR and PWR [1-20]. The neutron dose for the PWR RPV reaches around 0.1 dpa, while the dose for the BWR RPV is almost one or two orders lower since the BWR has larger distance between reactor core and RPV as well as lower core power density than the PWR. For long-term operation to 60 years, the dose for the PWR RPV can reach about 0.15 dpa, which corresponds to a fluence of about 10^{20} n/cm^2 (E > 1 MeV).

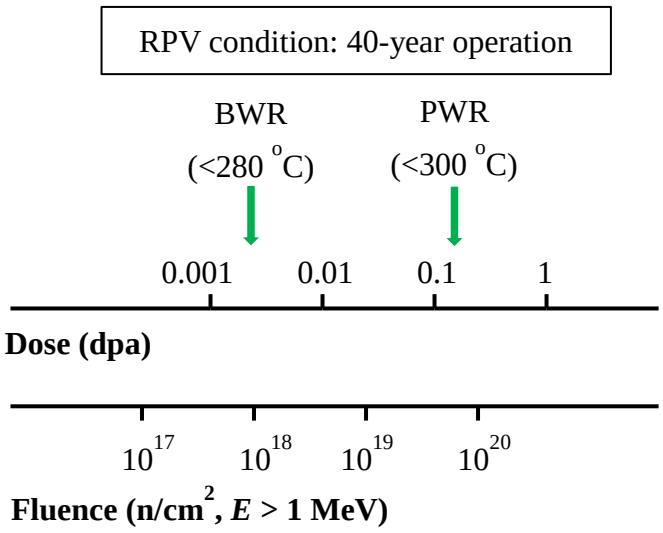

Fig. 1.7 Maximum neutron fluence, corresponding neutron dose and typical temperature for 40-year operation of RPVs of the BWR and PWR [1-20]

The irradiation embrittlement of RPV over a time scale of several decades originates from the lattice atom displacements due to energetic neutron bombardment which take place within a time scale of picosecond. Fig. 1.8 schematically shows the time evolution of

neutron irradiation damage processes [1-21]. Under irradiation, high-energy neutrons hit the lattice atoms, called primary knock-on atoms (PKAs). If the transferred energy during the collision is higher than the displacement threshold energy, the PKAs leave sites and start moving through the lattice. This interaction results in significant energy transfer to create energetic PKAs. Fig. 1.9 shows the PKA spectra for a typical PWR RPV [1-22]. The PKAs slow down in a branching series of collisions with secondary knock-on atoms (SKAs). The SKAs are then slowed down through the same mechanism. The collisional phase ends when no atom has enough energy to displace another atom. The collision process produces high concentrations of point defects including vacancies and self-interstitial atoms (SIAs). During the cooling phase, the defect rearrangement takes place, resulting in recombination of vacancies and SIAs or clustering of them [1-23]. A displacement cascade leads to direct formation of point defects and point defect clusters. Thermally activated diffusion process of the defects take place during the thermal and diffusion phases.

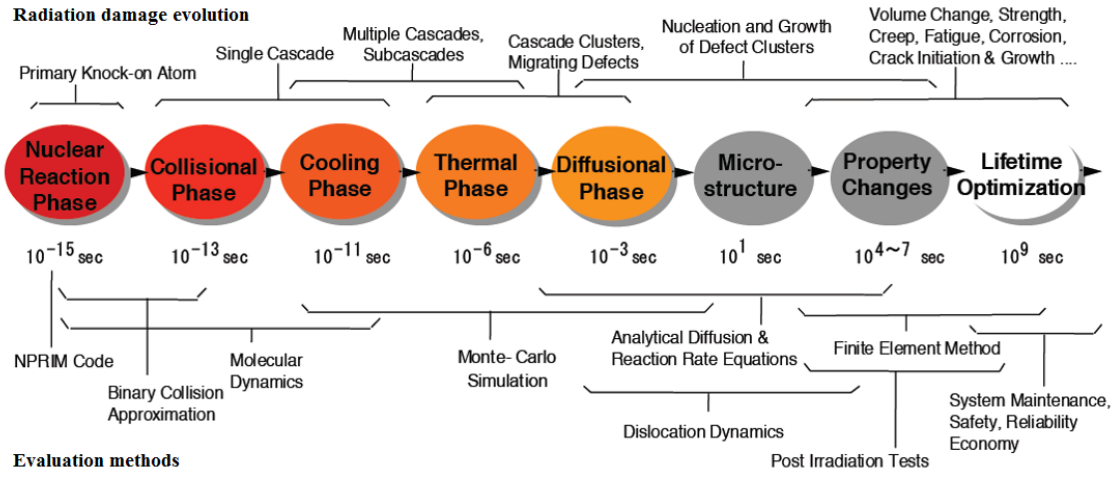

Fig. 1.8 Schematic diagram of time evolution of neutron irradiation damage [1-21]

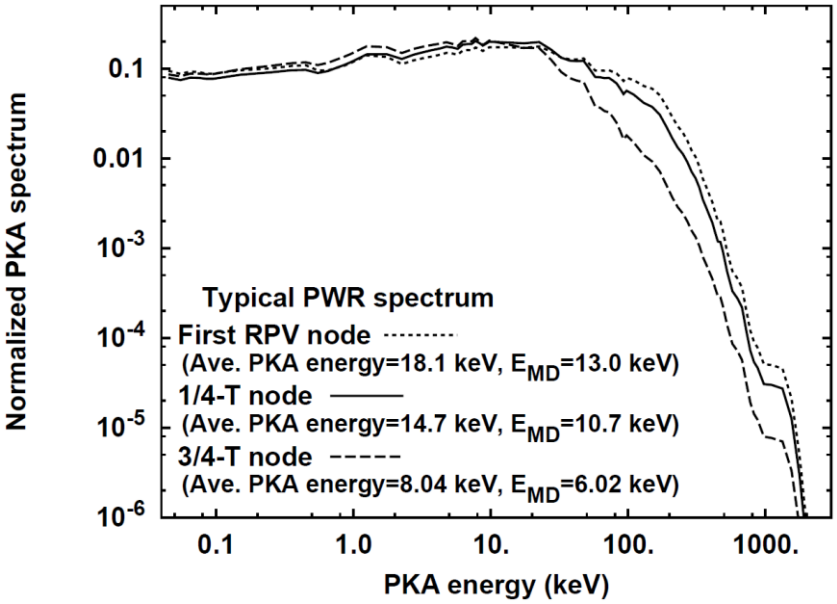

Fig. 1.9 Representative PKA spectra for three locations in a typical PWR RPV [1-22]

Diffusion of solute atoms, such as Cu, Ni, Mn, and Si atoms, can take place through a vacancy mechanism. The ab initio calculations of Vincent et al. [1-24] showed strong binding of Ni, Mn, and Si with vacancies in α-Fe. Besides, Olsson et al. [1-25] reported that Mn can also strongly bind with vacancies by magnetic coupling. Cu, Ni, Mn, and Si atoms can then diffuse in the opposite direction than that of vacancy, known as the inverse kirkendall effect, since their binding energies with vacancies are high and their migration energies that correspond to a first nearest neighbor jump are lower than the migration energy of Fe [1-26]. The study of Messina et al. [1-26] using ab initio calculations combined with a self-consistent mean field method showed that Cu, Ni, Mn, and Si atoms can also diffuse in the same direction with vacancy through vacancy drag in α-Fe because of their binding with vacancies. Solute diffusion can be driven by interstitials as well. Both ab initio calculations [1-27] and residual resistivity measurements [1-28,29,30] have reported the formation of Mn-SIA mixed dumbbells and the migration of mixed

dumbbells, indicating that Mn diffusion by an interstitial mechanism is very plausible.

Basically, three types of microstructures develop in the RPV as a consequence of defect and solute diffusion, including solute clusters enriched in Cu, Ni, Mn, and Si, matrix damage basically composed of point defect clusters, and grain boundary segregation of embrittling elements such as P. The solute clusters and matrix damage act as obstacles that impede dislocation movement, resulting in hardening of the material; while the grain boundary segregation causes a drop in the fracture strength. The effect of neutron irradiation in causing hardening or a drop in the fracture strength is to lead to embrittlement of the RPV.

1.5 Solute clusters

The progress in advanced microanalysis techniques such as atom probe tomography (APT) and small angle neutron scattering (SANS) has enabled researchers to perform detailed microstructural examinations of irradiated RPV steels and relevant model alloys. Such examinations have clearly shown the formation of solute clusters under irradiation and their complex chemical compositions [1-20]. The solute clusters are commonly formed in RPV steels regardless of the material chemical composition [1-15], and these clusters consist of Cu, Ni, Mn, Si, and occasionally P, as reported in so many papers, e.g. [1-15,31,32,33,34,35].

Cu has a dominant effect on solute clusters because of its very low solubility limit in Fe matrix (about 0.003% at typical irradiation temperature around 290 ^{o}C) [1-36]. The

formation of Cu-rich clusters was detected by positron annihilation at neutron fluences of an order of 10^{17} n/cm^2 [1-37]. It is recognized that the nucleation of Cu-rich clusters, measured as the number density of clusters, increases with increasing Cu content, and the fraction of Cu atoms in the clusters increases with increasing Cu content. Once the clusters nucleate, the Cu, Ni, Mn, and Si atoms in matrix consistently segregate to the clusters, resulting growth of clusters in size. The general trend is that the cluster radius in terms of the Guinier radius increases consistently with increasing neutron fluence [1-16]. The effect of Ni is commonly taken into consideration because of the synergetic effect of higher Ni on the Cu effect and of higher Cu on the Ni effect in terms of Cu-rich clusters, which affects the fluence dependence of hardening and embrittlement [1-15,18]. The general consensus of opinion from the literature is that Ni is energetically favored to be located at the cluster-matrix interface rather than at the cluster center or in the Fe matrix [1-38,39,40,41].

Several experimental studies have shown strong Ni-Mn interaction. A report of an International Atomic Energy Agency (IAEA) Cooperative Research Project notes that for a given high level of Ni in the material, high Mn content leads to much greater irradiation embrittlement than low Mn content for both VVER-1000 and PWR materials [1-42]. The Ni-Mn interaction was predicted long ago based on theoretical models [1-43,44], but the nature of Ni-Mn interaction remains unclear. Systematic analyses have been conducted on surveillance specimens from Japanese pressurized water reactors [1-15,31,32]. The mean atomic composition of the clusters was 6Cu-10Ni-6Mn-7Si, 2Cu-11Ni-5Mn-9Si, and 0Cu-12Ni-6Mn-12Si for 0.12wt.%Cu steels, 0.07wt.%Cu steels, and 0.04wt.%Cu steels, respectively. In the clusters, the Si concentration increased as the Cu concentration

decreased, while the concentrations of Ni and Mn remained unchanged, which may indicate a negative interaction between Si and Cu. Additionally, a recent study [1-45] have predicted that Si addition to binary Fe-Ni alloy can result in the formation of Ni-Si clusters at very low temperature. The clustering of Ni and Si at typical RPV temperature under the condition of no Cu requires further investigation.

1.6 Atom probe tomography

The characterization of the fine scale microstructural features responsible for the irradiation embrittlement of RPV steels and relevant model alloys has been the focus of many studies. APT has emerged as a very powerful experimental technique for the quantitative analysis of the local composition of the microstructural features in RPV materials. In this section, the basic principles of APT and its uncertainties are presented.

1.6.1 Principles of atom probe tomography

APT combines field evaporation, time-of-flight (TOF) spectroscopy and position-sensitive detection, as shown in Fig. 1.10. By applying a high electric field to the atom probe specimen it is possible to induce desorption and ionization of atoms even at cryogenic temperatures. This process, known as field evaporation [1-46], has an activation energy dependent on the applied electric field strength. Electrons can be stripped from surface atoms by a tunneling process at field strengths of 10 V/nm or greater, and the resultant positive ions are repelled from the specimen toward the counter electrode by applying a high voltage of ~3-10 kV to the specimen. In the local electrode atom probe (LEAP), the counter electrode is a small aperture which has a diameter of ~40 μm and is

located between the specimen and the detector. The atom probe specimen is prepared in the form of a needle tip with an apex radius of ~50 nm. The very small radius of the specimen and the high voltage induce a very high electric field (tens V/nm) which promotes field evaporation at cryogenic temperatures.

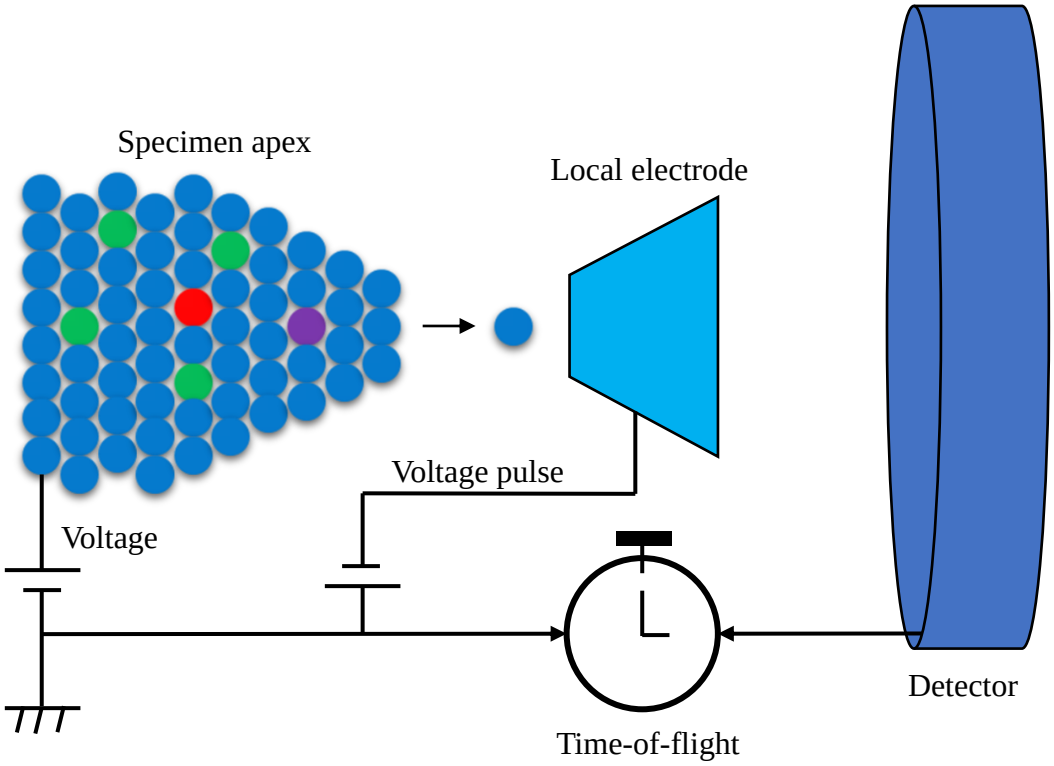

Fig. 1.10 Schematic principles of local electrode atom probe

APT uses a position-sensitive detector to record the impact position of individual ions and the sequence of evaporation events, which ultimately enables a mapping in 3D of the original position of the atoms on the specimen tip. During field evaporation of the specimen, the x-y position of the atom is determined from its impact position on the detector. The sequence of evaporation events is used to determine its z-position, the depth into the specimen along its long axis, since only surface atoms are removed.

During analysis, the field evaporation process is controlled, as illustrated in Fig. 1.11. First, a standing electric field (T_{base}, $V_{standing}$) which is below the evaporation threshold of the specimen ($V_{standing}$ is d.c. voltage), is established. Then the evaporation is triggered by additional pulses, such as negative electric pulses on the counter electrode or temperature pulses from laser irradiation on the specimen apex. This can be achieved since the evaporation rate increases with electric field and the temperature. The application of the pulse enables a measure of the departure time of an ion from the specimen. A second timing signal is obtained on arrival at the detector. This allows to measure the TOF it takes the ion to travel the distance from the specimen to the detector. The resultant TOF mass spectrometry is then used to chemically identify the ion.

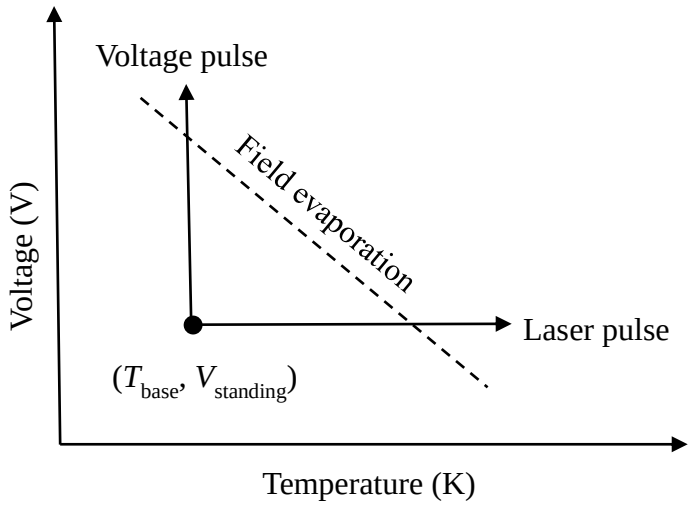

Fig. 1.11 Field evaporation process controlled by electric field and temperature

As the specimen is evaporated, if it is assumed that the potential energy of an ion is immediately converted to the kinetic energy, the speed of the ion v can be written as $v = L/t$, where L is the ion flight path length and t is the TOF of the ion. Then, by the energy

conservation law,

$$neV = \frac{1}{2}mv^2 = \frac{1}{2}m(\frac{L}{t})^2 \quad (1.9)$$

where *n* is the ion charge state, *e* is the elementary unit of charge, *V* is the potential difference, and *m* is the ion mass. Then the mass-to-charge-state ratio, *m*/*n* is given by

$$\frac{m}{n} = \frac{2eVt^2}{L^2} \quad (1.10)$$

1.6.2 Uncertainties of atom probe tomography

Anomalous behavior has been observed in some APT studies, where the apparent concentrations of certain elements differed from the expected values. For example, in ferritic Fe, APT tends to underestimate the true Cu content as the specimen temperature increases, where the apparent content of Si obtained by APT tends to higher than the actual content [1-47,48]. This is because of the difference in evaporation fields between different elements and has been interpreted by preferential evaporation and retention in field evaporation. The evaporation field for an element can be calculated at 0 K and the evaporation field data for some key elements in RPV steels are shown in Table 1.2 [1-49]. Fig. 1.12 illustrates the preferential evaporation of Cu in Fe [1-50]. In voltage pulse mode, the most dominant element, Fe, can be controlled to be field-evaporated by the superimposition of a standing voltage and a pulse voltage. The Cu atoms then preferentially filed-evaporate at higher temperatures during the application of the standing voltage alone. During the analysis, the ions evaporated by pulse voltage are counted as signals, whereas the ions evaporated by standing voltage are not counted as signals. Therefore, preferential evaporation would lead to an underestimation of the actual Cu concentration in Fe. For the preferential retention of Si in Fe, the Fe atoms

preferentially field-evaporate, while the preferentially retained Si atoms will be eventually evaporated by pulse voltage, which lead to an overestimation of the actual Si concentration in Fe.

Table 1.2 Evaporation filed for some key elements in RPV steels (V/nm) [1-49]

Element	F_1	F_2	F_3	F_4
Fe	42	33	54	100
Cu	30	43	77	120
Ni	35	36	65	110
Mn	30	30	60	100
Si	45	33	60	

*Note that F_n is the evaporation field for an element in the n-th charge state.

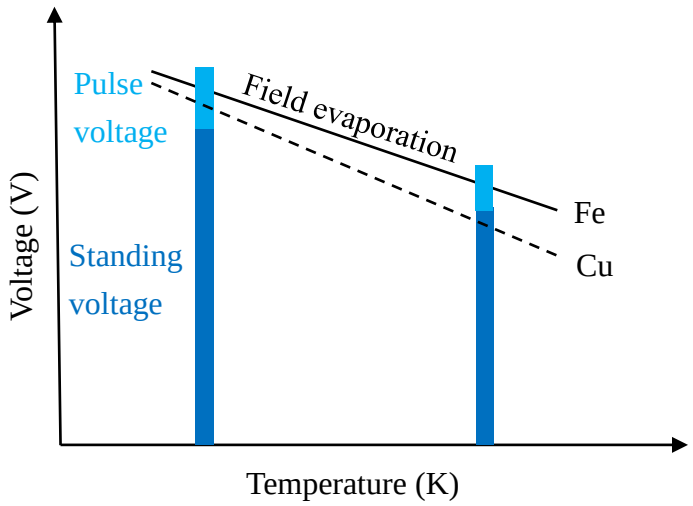

Fig. 1.12 Schematic for preferential evaporation of Cu in Fe [1-50]

The measurement conditions of APT must be carefully selected because of the issues of

preferential evaporation and retention in field evaporation. In voltage pulse mode, first, the d. c. standing voltage should be low enough to avoid field evaporation, while the standing voltage plus pulse voltage should provide all elements with similar probabilities of field evaporation. This requires a high pulse fraction which can simultaneously cover different evaporation fields that are required for the different elements. Second, a low specimen temperature is desirable since the difference in the evaporation field between two elements increases with temperature [1-51]. Furthermore, a high pulse repetition rate reduces the evaporation period by standing voltage. Therefore, it is generally accepted that low specimen temperature, high pulse fraction, and high pulse repetition rate are desirable for APT analysis [1-52]. But it should be noted that these preferable measurement conditions of APT increase the possibility of specimen rupture.

Besides the preferential evaporation and retention, there are still other uncertainties that should be considered. For example, the difference in evaporation fields between different elements can also lead to local magnification effects for RPV study. In addition, the specimen surface migration of some elements, such as C, Si, and P, prior to field evaporation may bias the atom position obtained by APT from the original location in the specimen [1-9].

1.7 Research objectives

The present study is focused on the solute clusters formed in RPV materials. Regarding long-term operation, the extensive study [1-16] on Japanese RPV steels at high neutron fluences (3×10^{19} n/cm^2 to $>10^{20}$ n/cm^2, E > 1 MeV) showed that the cluster radius

increased consistently with the fluence, indicating that the existing clusters grew in size; meanwhile, a slight increase in the cluster number density was still observed in most of the steels, indicating the formation of new clusters. The main objective of present study is to understand effects of solute elements, including Ni, Mn, and Si, on formation and growth of solute clusters in RPV.

In this study, novel experimental design, neutron irradiation following thermal ageing, will be used to simulate the microstructural evolution under the conditions of long-term operation. First, thermal ageing is performed to produce clusters which grow to large size. Then under the subsequent neutron irradiation, the pre-existing clusters produced by thermal ageing may continue to grow and new clusters may also be formed. Considering the open issues regarding Ni-Mn interaction, Si-Cu interaction, and Si-Ni interaction which are mentioned in chapter 1.5, the research objectives are then categorized as: to study effects of Ni and Mn on nucleation and growth of Cu-rich clusters during neutron irradiation following thermal ageing; to study effect of Si on nucleation and growth of Cu-rich clusters during neutron irradiation following thermal ageing; to study effect of Si on formation of Ni-rich clusters at high dose; to discuss the role of solutes and the embrittlement prediction for long-term operation of RPV.

In the thesis, chapter 2 describes the novel experimental design. For the neutron irradiation following thermal ageing experiments, RPV model alloys with systematic variations in chemical composition were selected. The alloys can be divided into four categories: Fe-Cu, Fe-Cu-Ni, Fe-Cu-Ni-Mn, and Fe-Cu-Si.

In chapter 3, evolution of clusters in Fe-Cu binary alloy under the neutron irradiation following thermal ageing is discussed. This is the basis to study effects of Ni, Mn and Si in more complex alloys Fe-Cu-Ni, Fe-Cu-Ni-Mn, and Fe-Cu-Si.

In chapter 4, effects of Ni and Mn in Cu-rich clusters are studied using the alloys Fe-Cu-Ni and Fe-Cu-Ni-Mn. Notably, the Ni content in the alloys Fe-Cu-Ni and Fe-Cu-Ni-Mn is varied in small range to probe the interaction between Ni and Mn.

In chapter 5, effect of Si in Cu-rich clusters is investigated using the ternary alloys Fe-Cu-Si. The Si content in the alloys Fe-Cu-Si is varied to identify its effect.

In chapter 6, effect of Si on Ni-rich clusters is focused on using the ternary model alloy Fe-Ni-Si. For this study, high-dose ion irradiation experiment is performed on the alloy at typical RPV temperature since the clusters in ferric alloys with no Cu have only been observed at high dose [1-53,54,55].

In chapter 7, contribution of solute effects to RPV embrittlement is discussed. This includes quantitative correlation between solute clusters and hardening, and discussion on solute effects and embrittlement prediction for long-term operation of RPV.

Chapter 8 concludes this thesis, and future studies are also discussed.

References in chapter 1

[1-1] The Power Reactor Information System, IAEA, 2017.

[1-2] S.R. Ortner, C.A. English, Applicability of Dose-Damage Relations to Operating Reactors, IAEA Technical Meeting Degradation Of Primary Components Of Pressurised Water-Cooled Nuclear Reactors: Current Issues And Future Challenges, Vienna, Austria, 2013.

[1-3] R.H. Sterne, L.E. Steele, Nucl. Eng. Des. 10 (1969) 259–307.

[1-4] Integrity of Reactor Pressure Vessels in Nuclear Power Plants: Assessment of Irradiation Embrittlement Effects in Reactor Pressure Vessel Steels, IAEA, 2009.

[1-5] N. Yamashita, M. Iwasaki, K. Dozaki, N. Soneda, J. Eng. Gas Turbines Power 132 (2010) 102919–102919.

[1-6] L.E. Steele, Neutron Irradiation Embrittlement of Reactor Pressure Vessel Steels, IAEA Technical Reports 163, 1975.

[1-7] R.K. Nanstad, M.A. Sokolov, D.E. McCabe, J. ASTM Int. 5 (2008) 1–14.

[1-8] Guidelines for Application of the Master Curve Approach to Reactor Pressure Vessel Integrity in Nuclear Power Plants, IAEA, 2005.

[1-9] N. Soneda, Irradiation Embrittlement of Reactor Pressure Vessels (RPVs) in Nuclear Power Plants, Woodhead Publishing, 2014.

[1-10] Rules for Arrangement and Safe Operation of Equipment and Piping of Nuclear Power Installations, PNAE, Energoatomizdat, Moscow, 1990.

[1-11] Design and Construction Rules for Mechanical Components of PWR Nuclear Islands, RCC-M, AFCEN, Paris, 1980.

[1-12] Codes for Nuclear Power Generation Facilities - Rules on Design and Construction for Nuclear Power Plants, JSME, 2001.

[1-13] Surveillance of the Irradiation Behaviour of Reactor Pressure Vessel Materials of LWR Facilities, KTA, 2001.

[1-14] N. Soneda, A. Nomoto, J. Eng. Gas Turbines Power 132 (2010) 102918-102918–9.

[1-15] N. Soneda, K. Dohi, A. Nomoto, K. Nishida, S. Ishino, J. ASTM Int. 7 (2010) 1–20.

[1-16] N. Soneda, K. Dohi, K. Nishida, A. Nomoto, M. Tomimatsu, H. Matsuzawa, J. ASTM Int. 6 (2009) 1–16.

[1-17] M. KIRK, Nucl. Eng. Technol. 45 (2013) 277–294.

[1-18] E.D. Eason, G.R. Odette, R.K. Nanstad, T. Yamamoto, J. Nucl. Mater. 433 (2013) 240–254.

[1-19] G.R. Odette, G.E. Lucas, JOM 53 (2001) 18–22.

[1-20] K. Fukuya, J. Nucl. Sci. Technol. 50 (2013) 213–254.

[1-21] N. Sekimura, Nuclear Energy and Advanced Technology-1, NSA/COMMENTARIES No.2, 1994.

[1-22] R.E. Stoller, L.R. Greenwood, in:, ASTM STP 1405, ASTM, 2001, pp. 204–217.

[1-23] K. Morishita, N. Sekimura, T. Diaz de la Rubia, J. Nucl. Mater. 248 (1997) 400–404.

[1-24] E. Vincent, C.S. Becquart, C. Domain, Nucl. Instrum. Methods Phys. Res. Sect. B Beam Interact. Mater. At. 228 (2005) 137–141.

[1-25] P. Olsson, T.P.C. Klaver, C. Domain, Phys. Rev. B 81 (2010) 054102.

[1-26] L. Messina, M. Nastar, T. Garnier, C. Domain, P. Olsson, Phys. Rev. B 90 (2014) 104203.

[1-27] E. Vincent, C.S. Becquart, C. Domain, J. Nucl. Mater. 359 (2006) 227–237.

[1-28] F. Maury, A. Lucasson, P. Lucasson, Y. Loreaux, P. Moser, J. Phys. F Met. Phys. 16 (1986) 523.

[1-29] F. Maury, A. Lucasson, P. Lucasson, P. Moser, F. Faudot, J. Phys. Condens. Matter 2 (1990) 9291.

[1-30] K. Murakami, T. Iwai, H. Abe, N. Sekimura, Y. Katano, T. Iwata, T. Onitsuka, Philos. Mag. 95 (2015) 1680–1695.

[1-31] N. Soneda, K. Dohi, A. Nomoto, K. Nishida, S. Ishino, Development of neutron irradiation embrittlement correlation of reactor pressure vessel materials of light water reactors, CRIEPI Report Q06019, 2007.

[1-32] K. Fukuya, K. Ohno, H. Nakata, S. Dumbill, J.M. Hyde, J. Nucl. Mater. 312 (2003) 163–173.

[1-33] M.K. Miller, K.F. Russell, M.A. Sokolov, R.K. Nanstad, J. Nucl. Mater. 361 (2007) 248–261.

[1-34] R.G. Carter, N. Soneda, K. Dohi, J.M. Hyde, C.A. English, W.L. Server, J. Nucl. Mater. 298 (2001) 211–224.

[1-35] J.T. Buswell, W.J. Phythian, R.J. McElroy, S. Dumbill, P.H.N. Ray, J. Mace, R.N. Sinclair, J. Nucl. Mater. 225 (1995) 196–214.

[1-36] G.R. Odette, G.E. Lucas, Radiat. Eff. Defects Solids 144 (1998) 189–231.

[1-37] K. Fujii, H. Nakata, K. Fukuya, T. Ohkubo, K. Hono, Y. Nagai, M. Hasegawa, T. Yoshiie, J. Nucl. Mater. 400 (2010) 46–55.

[1-38] A. Seko, S.R. Nishitani, I. Tanaka, H. Adachi, E.F. Fujita, Calphad 28 (2004) 173–176.

[1-39] R. Prakash Kolli, D.N. Seidman, Acta Mater. 56 (2008) 2073–2088.

[1-40] A.T. Al-Motasem, M. Posselt, F. Bergner, J. Nucl. Mater. 418 (2011) 215–222.

[1-41] P.D. Styman, J.M. Hyde, K. Wilford, D. Parfitt, N. Riddle, G.D.W. Smith, Ultramicroscopy 159, Part 2 (2015) 292–298.

[1-42] Effects of Nickel on Irradiation Embrittlement of Light Water Reactor Pressure Vessel Steels, IAEA, 2005.

[1-43] G.R. Odette, MRS Proc. 373 (1994) 137–148.

[1-44] G.R. Odette, B.D. Wirth, J. Nucl. Mater. 251 (1997) 157–171.

[1-45] K. Murakami, T. Iwai, H. Abe, N. Sekimura, J. Nucl. Mater. 482 (2016) 47–52.

[1-46] E.W. Müller, Phys. Rev. 102 (1956) 618–624.

[1-47] Y. Yamaguchi, J. Takahashi, K. Kawakami, Ultramicroscopy 109 (2009) 541–544.

[1-48] M.K. Miller, G.D.W. Smith, J. Vac. Sci. Technol. 19 (1981) 57–62.

[1-49] T.T. Tsong, Surf. Sci. 70 (1978) 211–233.

[1-50] J. Takahashi, K. Kawakami, Surf. Interface Anal. 46 (2014) 535–543.

[1-51] M. Wada, Surf. Sci. 145 (1984) 451–465.

[1-52] M.K. Miller, A. Cerezo, M.G. Hetherington, G.D.W.S. FRS, Atom Probe Field Ion Microscopy, Oxford University Press, Oxford, New York, 1996.

[1-53] E. Meslin, B. Radiguet, P. Pareige, A. Barbu, J. Nucl. Mater. 399 (2010) 137–145.

[1-54] K. Fujii, T. Ohkubo, K. Fukuya, J. Nucl. Mater. 417 (2011) 949–952.

[1-55] E. Meslin, B. Radiguet, M. Loyer-Prost, Acta Mater. 61 (2013) 6246–6254.

Chapter 2 Materials and methods

2.1 Materials

The model alloys, including Fe-Cu, Fe-Cu-Ni, Fe-Cu-Ni-Mn, and Fe-Cu-Si, were used in this study and their chemical compositions are given in Table 2.1. A high Cu content, 0.5% was used in all the alloys to form Cu-rich clusters during the thermal ageing. The Ni, Mn, and Si contents in these alloys were according to the chemical compositions of commonly used Japanese RPV steels [2-1]. The model alloys were made by JFE Steel Corporation and were solution annealed at 900 ^{o}C for 30 min. This was then followed by water quenching.

Table 2.1 Chemical composition of the alloys (wt.%)

Alloy	Cu	Ni	Mn	Si	C	P	Mo
Fe-0.5Cu	0.51	0.01	0.01	0.01	0.0007	0.002	0.01
Fe-0.5Cu-0.6Ni	0.52	0.58	0.01	0.02	0.0006	0.002	0.01
Fe-0.5Cu-0.8Ni	0.52	0.78	0.01	0.02	0.0006	0.002	0.01
Fe-0.5Cu-0.6Ni-1.4Mn	0.53	0.59	1.43	0.02	0.0005	0.002	0.01
Fe-0.5Cu-0.8Ni-1.4Mn	0.52	0.78	1.41	0.02	0.0005	0.002	0.01
Fe-0.5Cu-0.1Si	0.52	0.01	0.01	0.10	0.0009	0.002	0.01
Fe-0.5Cu-0.2Si	0.52	0.01	0.01	0.19	0.0010	0.002	0.01

*Note that the alloys also contain some Al, S, and other trace elements.

2.2. Neutron irradiation following thermal ageing

Prior to the neutron irradiation, thermal ageing was performed under vacuum (below 1×10^{-3} Pa) to produce clusters in the alloys. The ageing temperature was set at 450 ^{o}C, which was higher than the temperature of the subsequent neutron irradiation. This high temperature was used to increase the size of the clusters formed by ageing. Benefiting from the large cluster size, these clusters could be distinguished from the clusters formed during the subsequent irradiation, which were expected to be small in size. In this work, the Fe-Cu, Fe-Cu-Ni, and Fe-Cu-Si alloys were aged for 225 h, while the Fe-Cu-Ni-Mn alloys were aged for 90 h. This made all the alloys reach their maximum hardness at 450 ^{o}C [2-2]. When the alloys were aged to their maximum hardness, their solute clusters grew well and had a large size and high number density. Moreover, the high Cu content in the alloys was expected to dominate the microstructure. In addition, Miller et al. [2-3] showed that even though the thermal equilibrium state was not reached, the matrix Cu content was largely reduced when a Fe-Cu-Ni alloy was aged to its maximum hardness at 500 ^{o}C. These results are beneficial for studying the effects of Ni, Mn, and Si on the Cu-rich clusters during the neutron irradiation following thermal ageing.

The aged alloys were then neutron-irradiated at Czech's research reactor LVR-15. The neutron fluence received at an irradiation temperature of 290 ^{o}C and a flux of ~6×10^{12} n/cm^2/s was 5.8×10^{18} n/cm^2 (E > 1 MeV). This neutron fluence corresponds to about 0.01 dpa. Previous study [2-4,5] on a neutron-irradiated Fe-0.1 at.%Cu binary alloy showed that the number density of Cu clusters in such alloy saturated at around 0.02 dpa, which is higher than the neutron dose used in this work.

2.3. Atom probe analysis

2.3.1 Specimen preparation

Specimen preparation is one critical step to realize a successful APT analysis, and requires a combination of science and art. There are generally three fundamental criteria for a successful specimen preparation. First, the needle-shaped specimen must be sharp enough (with an apex radius of ~50 nm) to allow field evaporation. Second, its shape should be well controlled to avoid specimen rupture and allow for significant evaporation events so as to acquire enough data for analysis. Third, the near-apex region of the specimen should contain the user-defined features of interest.

Table 2.2 Advantages and limitations of electro-polishing method and FIB method

Specimen preparation method	Advantages	Limitations
Electro-polishing	Low cost of time; no Ga^+ ion implantation	Limited to conductive metals and alloys; issues of oxidation; difficult to prepare site-specific specimen
FIB	Site-specific specimen preparation permitted; suitable for conductive, semi-conductive, or insulator materials	High cost of time; Ga^+ ion implantation; demand of user skill

Electro-polishing and focused ion beam (FIB) milling are two prevalent methods for APT specimen preparation. Table 2.2 provides a brief description of the advantages and limitations of these two methods. In this research, the specimens in the neutron irradiation following thermal ageing experiments were prepared using the electro-polishing method and this will be discussed here. The FIB method was used to prepare the specimens in ion irradiation experiments and will be discussed in Chapter 6.

In electro-polishing method, a matchstick is taken from bulk material, and then this is followed by a two-step electro-polishing which shapes the specimen matchstick into sharp needle-shaped one. In this research, a block with a size of ~0.4×10×10 mm^3 was first cut from the bulk material which has a cross section of 10×10 mm^2 using Struers Accutom-5 with a cut-off wheel of thickness 0.52 mm. The block surfaces were then polished with metal polishing paper P1000 and the block thickness reached ~0.35 mm. The following step was to fabricate ~0.35×0.35×10 mm^3 matchsticks from the block using Accutom-5 with a cut-off wheel of 0.2mm thickness. The matchstick was then refined by paper polishing to remove the burr and finalized into ~0.3×0.3×10 mm^3 (see Fig. 2.1). The cross section of the matchstick was controlled to be a square, since the shape deviation can produce an undesirable wedge-shaped needle. The surface deformation introduced by the initial preparation process will normally be removed during the subsequent electro-polishing stage. Prior to electro-polishing, the prepared matchstick was mounted into a small Cu tube and fixed firmly.

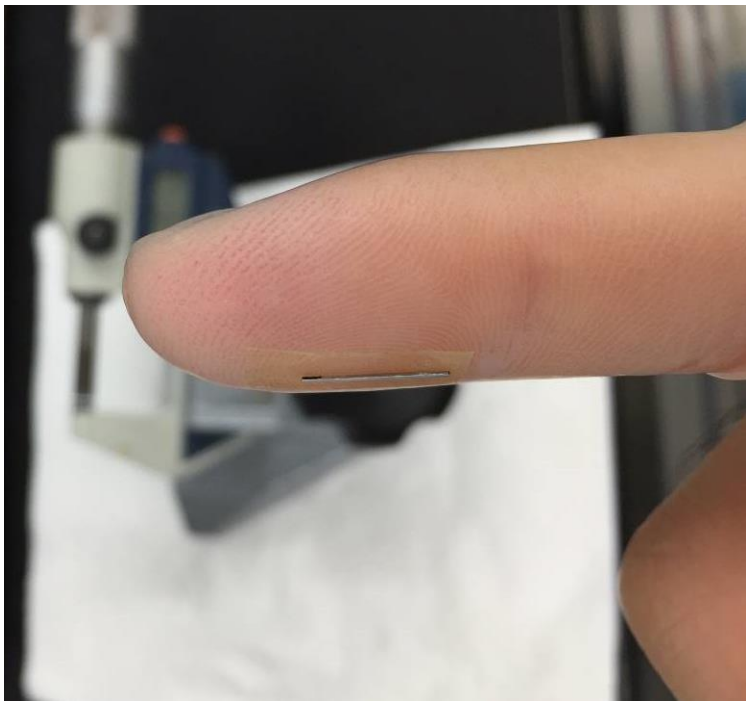

Fig. 2.1 The matchstick of an unirradiated sample to be refined by paper polishing

A two-step electro-polishing, including standard electro-polishing and micro electro-polishing, was used to produce desirable APT specimen from the matchstick, as illustrated in Fig. 2.2. The matchstick acts as an electrode and works with a counter electrode, an electrolyte, and a controllable voltage. During the first-step standard electro-polishing, the matchstick must frequently be lifted out from the electrolyte to examine its shape and to avoid over-polishing. This was followed by micro electro-polishing, when the specimen matchstick was thinned enough into a needle-shaped one. In the micro electro-polishing, the needle-shaped specimen was positioned and located in the center of a drop of electrolyte suspended in a wire loop. A voltage was applied between the specimen and the wire loop. The polishing process can be observed under an optical microscope. It should be noted that the specimen must always be thoroughly and carefully cleaned using ethanol and acetone to remove all traces of the electrolytes and other

contaminations following electro-polishing for a successful specimen preparation.

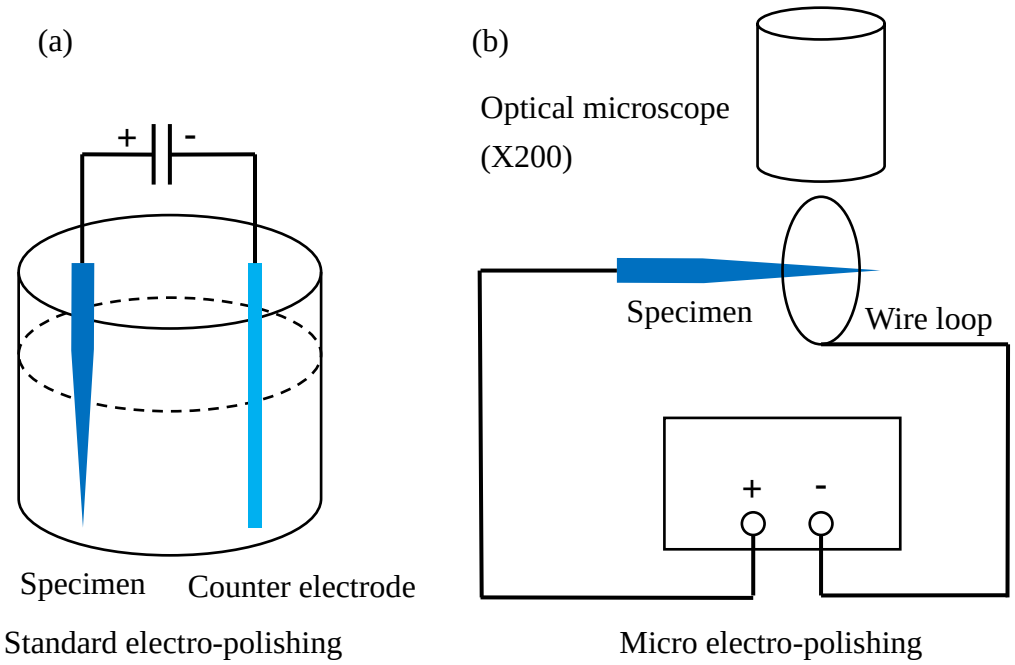

Fig. 2.2 Schematic diagrams of (a) standard electro-polishing, and (b) micro electro-polishing

In LEAP analysis, the typical analyzed volume is ~50×50×100-200 nm^3. A good specimen requires to be free from any protrusions, grooves or cracks, especially in the near-apex region, as shown in Fig. 2.3. In this research, in order to obtain large amounts of successful data (eventually to measure high number of solute clusters), the needle specimen was prepared in long sharp shape by well controlling the slope of the needle specimen. This enables a large analyzed volume which can even be up to ~50×50×1000 nm^3.

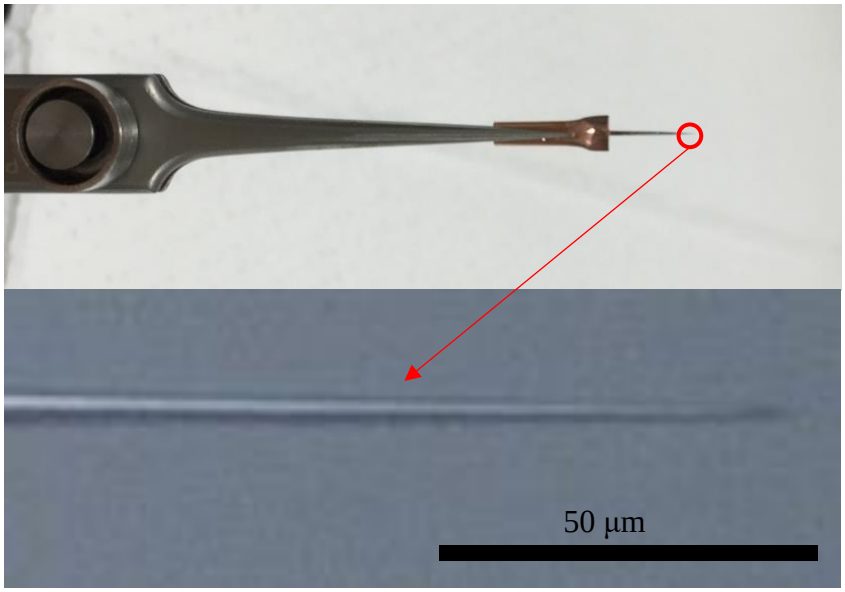

Fig. 2.3 The needle-shaped specimen for LEAP analysis

2.3.2 LEAP analysis

APT was employed for the microstructural characterization under two conditions:

- When the alloys were aged to their maximum hardness (aged to max Hv).
- When the alloys were first aged to their maximum hardness and then irradiated (aged+irradiated).

The APT specimens were analyzed using CAMECA's local electrode atom probe (LEAP 3000XSi) equipped at the Central Research Institute of Electric Power Industry which is shown in Fig. 2.4. The LEAP analysis was performed in the voltage pulse mode. A specimen temperature of 40 K, a pulse repetition rate of 200 kHz, and a pulse fraction of 15% were used to avoid the preferential evaporation of Cu [2-6]. All the experiments were carried out with a target evaporation rate in the range of 3-5% per pulse.

Fig. 2.4 LEAP 3000XSi used in the research

Multiple APT measurements were carried out for each material. The minimum number of measurements carried out for a material in this study was three. Typically more than 200 solute clusters were counted for each material. The large number of solute clusters taken from different regions of a specimen facilitated the detailed analyses of the clusters.

2.3.3 Data processing

In APT, the basic generated data are the mass-to-charge state ratio and the atomic coordinates of each atom in the analyzed volume. These data can be visualized in the form of atom maps. Fig. 2.5 shows the atom maps for Fe-0.5Cu-0.8Ni alloy after ageing plus irradiation. In the atom maps, a small dot indicates the position of one atom and the different colors of the dots indicate the different elements. Here, the atoms of Fe are not shown for clarity. The Cu-Ni clusters are clearly visible through the atom maps. In this

research, the cluster analysis was performed using a recursive search algorithm (RSA) method [2-7,8]. Here, the core solute atoms, i.e., Cu, Ni, Mn, and Si, which belong to the same cluster, are first searched within the separation of 0.4 nm. Then, any periphery atom such as an Fe atom within the separation of 0.4 nm from the core atoms is considered to belong to the cluster. Finally, the periphery atoms with less than three core atoms within a distance of 0.4 nm are removed. After all the clusters are found, any cluster that contains less than 20 core atoms is excluded from the analysis. These parameters for searching clusters work well for high Cu RPV model alloys and have been applied in previous studies, e.g. in [2-6].

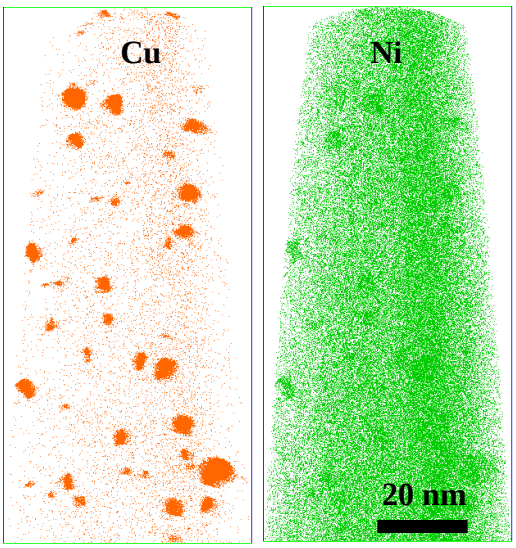

Fig. 2.5 Atom maps for Fe-0.5Cu-0.8Ni alloy after ageing plus irradiation

The cluster number density was determined by dividing the total number of clusters by the total reconstruction volume. The cluster radius in this work was defined using the Guinier radius, which is the radius of gyration multiplied by $(5/3)^{1/2}$. The volume fraction of the clusters was determined by dividing the sum of the volume of each cluster by the

total reconstruction volume. In this study, the clusters searched on dislocations and grain boundaries were excluded from the analysis, since it was found that the size and composition of such clusters could be altered.

2.4 Vickers hardness tests

Vickers hardness tests were conducted using Shimadzu HSV-20 for the mechanical property characterization of the alloys under three conditions: after solution annealing, after ageing to maximum hardness, and after ageing+irradiation. A load of 1 kgf was applied for the tests with 12 indents per sample. All procedures were consistent with the JIS Z2244 standard.

References in chapter 2

[2-1] N. Yamashita, M. Iwasaki, K. Dozaki, N. Soneda, J. Eng. Gas Turbines Power 132 (2010) 102919–102919.

[2-2] L. Liu, Effects of Solute Elements on Hardening and Microstructural Changes of Thermally Aged RPV Model Alloys Using Three-Dimensional Atom Probe, Master thesis, The University of Tokyo, 2011.

[2-3] M.K. Miller, K.F. Russell, P. Pareige, M.J. Starink, R.C. Thomson, Mater. Sci. Eng. A 250 (1998) 49–54.

[2-4] E. Meslin, Mécanismes de Fragilisation Sous Irradiation Aux Neutrons D'alliages Modèles Ferritique et D'un Acier de Cuve: Amas de Défauts, PhD thesis, Université de Rouen, 2007.

[2-5] R. Ngayam-Happy, C.S. Becquart, C. Domain, L. Malerba, J. Nucl. Mater. 426 (2012) 198–207.

[2-6] L. Liu, K. Nishida, K. Dohi, A. Nomoto, N. Soneda, K. Murakami, Z. Li, D. Chen, N. Sekimura, J. Nucl. Sci. Technol. 53 (2016) 1546–1553.

[2-7] N. Soneda, K. Dohi, K. Nishida, A. Nomoto, M. Tomimatsu, H. Matsuzawa, J. ASTM Int. 6 (2009) 1–16.

[2-8] J.M. Hyde, C.A. English, MRS Proc. 650 (2000).

Chapter 3 Evolution of clusters in Fe-Cu

Neutron irradiation following thermal ageing experiments were performed using Fe-Cu, Fe-Cu-Ni, Fe-Cu-Ni-Mn, and Fe-Cu-Si alloys in the research. Basically, the investigation of effects of Ni, Mn, and Si requires first understanding of the changes in microstructures during the neutron irradiation in the base alloy Fe-Cu. This chapter describes the characteristics and distribution of clusters in Fe-Cu alloy when aged to maximum hardness, and when aged plus irradiated to understand the microstructural evolution.

3.1 Characteristics of clusters in Fe-Cu

Table 3.1 summarizes the characteristics of the clusters in Fe-0.5Cu when aged to maximum hardness, and when aged plus irradiated. These characteristics include the number density, volume fraction, mean radius, and mean composition of the clusters. The number density and volume fraction values given here are the weighted means of various measurements, where the weight for each measurement is the total number of atoms in the reconstructed tip. The minimum and maximum of various measurements are given in parenthesis. The mean radius and mean composition given in the tables represent the mean of the radius and composition data collected from all the measurements for various clusters. The mean radius refers to a simple mean, while the mean composition refers to a weighted mean, where the weight for each cluster is the total number of atoms contained in the cluster. This weighted mean approach for the cluster composition limits the contribution of very small clusters as their compositions may be skewed because of the small number of atoms in them.

Table 3.1 Number density, volume fraction, mean radius, and mean composition of the clusters in Fe-0.5Cu when aged to maximum hardness, and when aged plus irradiated

Condition	Number density ($\times10^{23}$ m^{-3})	Volume fraction ($\times10^{-3}$)	Mean radius (nm)	Mean composition (at.%)	
				Cu	Fe
Aged to max Hv	0.74 (0.63/0.84)	1.50 (1.05/2.11)	1.56	45.2	37.6
Aged+irradiated	1.39 (1.34/1.55)	2.66 (2.46/2.79)	1.46	48.4	36.7

The increased cluster number density accompanied with increased cluster volume fraction under the neutron irradiation indicates that new clusters formed in Fe-0.5Cu. This is because the clustered Cu content of the alloy, defined as the ratio of the total number of Cu atoms in all clusters to the total number of atoms in the reconstructed tip, was only 0.16at.% when aged to maximum hardness based on the APT analysis, in other words, high content of Cu atoms (0.28at.%, assuming that Fe-0.5Cu alloy contains 0.50wt.%Cu equivalent to 0.44at.%Cu) remained in matrix. After the neutron irradiation, the clustered Cu content in Fe-0.5Cu increased to 0.32at.%.

3.2 Distribution of clusters in Fe-Cu

To get a clear picture of the evolution of clusters under the neutron irradiation, size distribution of the clusters was investigated. Fig. 3.1 shows the size distribution of the clusters in Fe-0.5Cu when aged to maximum hardness, and when aged plus irradiated. About 600 clusters were counted under each condition, implying that a density difference

of 10^{22} m^{-3} in this histogram corresponded to more than 40 counted clusters. Thermal ageing produced high number density of clusters, the sizes of which showed a unimodal distribution with a peak at ~1.6 nm. The subsequent neutron irradiation then increased the total cluster number density from 0.74×10^{23} to 1.39×10^{23} m^{-3} and altered the size distribution of the clusters, as illustrated in Fig. 3.1. The size distribution of the clusters became bimodal with peaks at ~1.0 and ~1.8 nm.

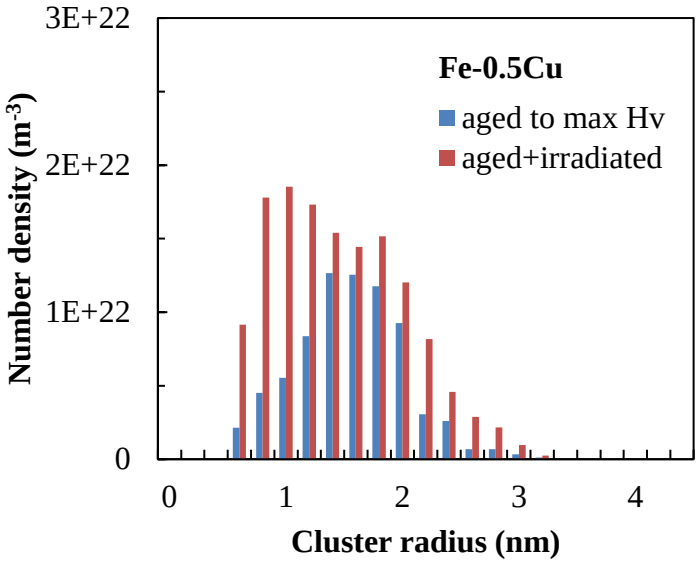

Fig. 3.1 Size distribution of the clusters in Fe-0.5Cu when aged to maximum hardness, and when aged plus irradiated

To evaluate the cluster changes during the neutron irradiation, one method is to subtract directly number density of the clusters in radius r when aged to maximum hardness $Nd_{r,\text{aged to max Hv}}$ from number density of the clusters in radius r when aged plus irradiated $Nd_{r,\text{aged+irradiated}}$.

$$\Delta Nd_r = Nd_{r,\text{aged+irradiated}} - Nd_{r,\text{aged to max Hv}} \quad (3.1)$$

This assumes that the pre-existing clusters produced by the thermal ageing do not change in size and number density, although this hypothesis is not based on theoretical model and should be fictitious. Fig. 3.2 shows the change of clusters in Fe-0.5Cu during the neutron irradiation. The cluster size distribution produced by subtraction exhibited broad spread towards large radius region, and one peak at 2.2 nm even appeared. These observations indicate that the pre-existing clusters formed by the thermal ageing should grow under the neutron irradiation.

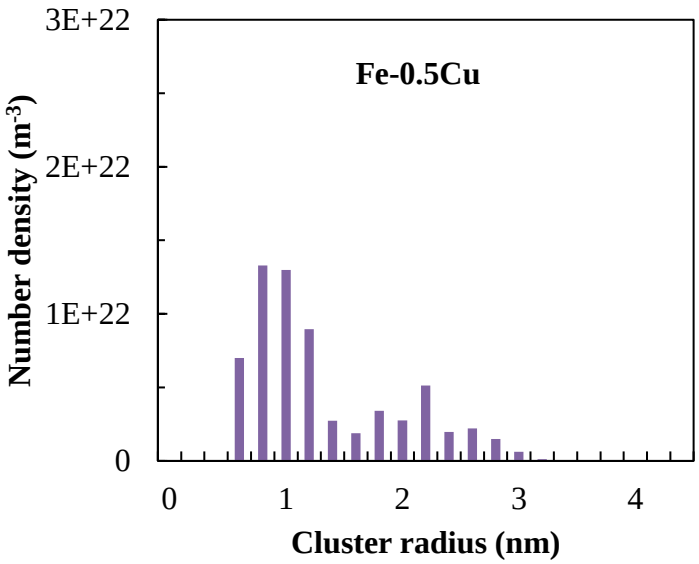

Fig. 3.2 Change of clusters in Fe-0.5Cu during the neutron irradiation

The picture that explains the evolution of clusters in Fe-0.5Cu can be as follows. High content of Cu atoms remained in matrix when the alloy was aged to maximum hardness. Under the neutron irradiation, the pre-existing clusters produced by the thermal ageing grew in size, shifting their distribution in size towards large radius region, which resulted in the observation of one peak at large radius region, as at ~1.8 nm in Fig. 3.1. Meanwhile,

a group of new clusters formed through Cu nucleation, resulting in the observation of one peak at small radius region, as at ~1.0 nm in Fig. 3.1. This microstructural evolution agreed well with our expectation from the experimental design.

Comments about the growth of clusters under thermal ageing and under neutron irradiation

The temporal behavior of size distribution of solute clusters, growing from supersaturated solution under thermally activated processes, was studied by a number of researchers before the 1970s. For diffusion controlled precipitation, Kahlweit [3-1] developed a model to describe the instantaneous rate of change of the cluster radius *r* as:

$$\frac{dr}{dt} = \frac{D \times V_m \times (C - C_s)}{r} \tag{3.2}$$

where D is the solute diffusion rate, V_m is the molar volume of the cluster, C is the concentration of solute at distances far from any cluster, C_s is the equilibrium saturation concentration of solute. From the Kahlweit model, the instantaneous rate of change of the cluster surface area S becomes independent of the cluster radius r [3-2,3], since

$$\frac{dS}{dt} = \frac{d[4\pi r^2]}{dt} = 8\pi \times D \times V_m \times (C - C_s) \tag{3.3}$$

This indicates that as solute clusters grow, the surface area distribution of the clusters undergoes pure translation to larger surface area.

Growth of solute clusters under neutron irradiation requires considerations, including radiation enhanced diffusion, collisional processes by energetic cascades, and solute segregation effects. Radiation enhanced diffusion is related to diffusional mechanisms that are strongly affected by the presence of radiation produced defects. For example, the

excess vacancies produced by neutron irradiation increase Cu diffusion rate in Fe by several orders of magnitude [3-4]. Cascade collision might cause atoms within the cluster to recoil into the matrix. The average primary knock-on atom (PKA) energy at the first RPV node (8 mm of the way through the RPV) is about 18 keV in a typical PWR RPV [3-5], as shown in the PKA energy spectra in Fig. 1.9 in chapter 1. In studied Fe-0.5Cu, the pre-existing clusters produced by the 450 ^{o}C thermal ageing appeared to be stable and not to be destroyed by the subsequent neutron irradiation. Since the cascade event do not begin from the constituent atoms of the cluster, the energy spectrum of the primary recoil atoms in the cluster can be in low energy region so that the cluster is hard to be destroyed. Fig. 3.3 gives an example of the recoil energy distribution of struck atoms in Fe by an incident Fe atom with an energy of 20 keV. This shows that for a sequences of secondary knock-on atoms (SKAs) created by 20 keV PKA, their mean energy has been reduced to several hundred eV.

In the literature, there has been little experimental evidence for dissolution under cascade collision, except for disordering of the ordered phase such as in [3-6]. Sekimura et al. [3-7] studied the stability of MC precipitates in austenitic stainless steels under heavy ion irradiation and suggested that the pre-existing MC precipitates have strong stability against recoil dissolution under cascade damage. The Monte-Carlo based calculations of Chou and Ghoniem [3-8] predicted that the maximum cluster size that may be completely destroyed by a high energy collision cascade is very limited. For example, for a cascade with an average PKA energy of about 500 keV in Fe, the maximum cluster size that may be completely destroyed is in the order of 1 nm diameter [3-8]. These results are consistent with the strong stability of clusters under neutron irradiation, as observed in

studied Fe-0.5Cu.

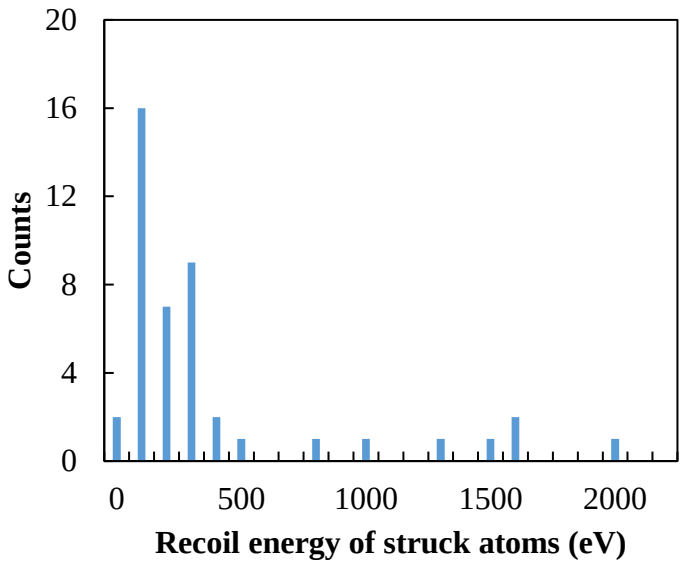

Fig. 3.3 Recoil energy distribution of struck atoms in Fe by an incident Fe atom with an energy of 20 keV calculated using SRIM-2008 [3-9] (only those struck atoms of which the recoil energy is greater than the displacement energy 40 eV are counted)

Regarding solute segregation effects, it is known that the fluxes of point defects generated by irradiation can segregate solute atoms to various defect sinks [3-10]. The Cu clusters in Fe are probably sinks for vacancy and interstitial defects, and may act as their recombination sites under irradiation conditions [3-11,12]. The irradiation induced solute segregation to Cu clusters might also have contributed to the growth of clusters in Fe-0.5Cu.

Comments about size distribution of the clusters

To well represent the solute clusters using APT analysis, multiple APT measurements

were carried out for each material. Fig. 3.4 shows the size distribution of the clusters with 0.4 nm bin width in three APT tips analyzed for Fe-0.5Cu when aged to maximum hardness with increasing cluster numbers of 37, 113, and 276. All three tips showed similar unimodal distributions. This research requires use of small bin width for cluster size distribution to get a clear picture of the evolution of clusters. For the cluster size distribution, when the bin width was reduced from 0.4 nm to 0.2 nm that was used in this research, tips No. 2 and 3 represented similar unimodal distributions, whereas tip No. 1 did not represent the unimodal distribution, as observed in Fig. 3.5. Therefore, a large cluster number, e.g., at least in the order of 100, can be desirable for the cluster size analysis with a bin width of 0.2 nm.

From Fig. 3.5, a detailed comparison between tips No. 2 and 3 showed the difference that the peak of the cluster size distribution for tip No. 2 appeared at ~1.4 nm while the peak for tip No. 3 appeared at ~1.6 nm. Also, the local chemical composition given by APT exhibited tip-to-tip variations. The difference between tips No. 2 and 3 appears to result from the heterogeneity in initial chemical composition of the alloy. The differences in the cluster size distribution (e.g., in terms of mean cluster radius and its standard deviation) and the local chemical composition between different tips were also observed in Fe-0.5Cu when aged plus irradiated. Therefore, for the APT analysis in the present study, several tips were taken from different positions of the alloy. The size distribution of the clusters that is used to represent each alloy under each condition, e.g., those in Fig. 3.1, was obtained through statistical analysis of the total clusters collected from all tips.

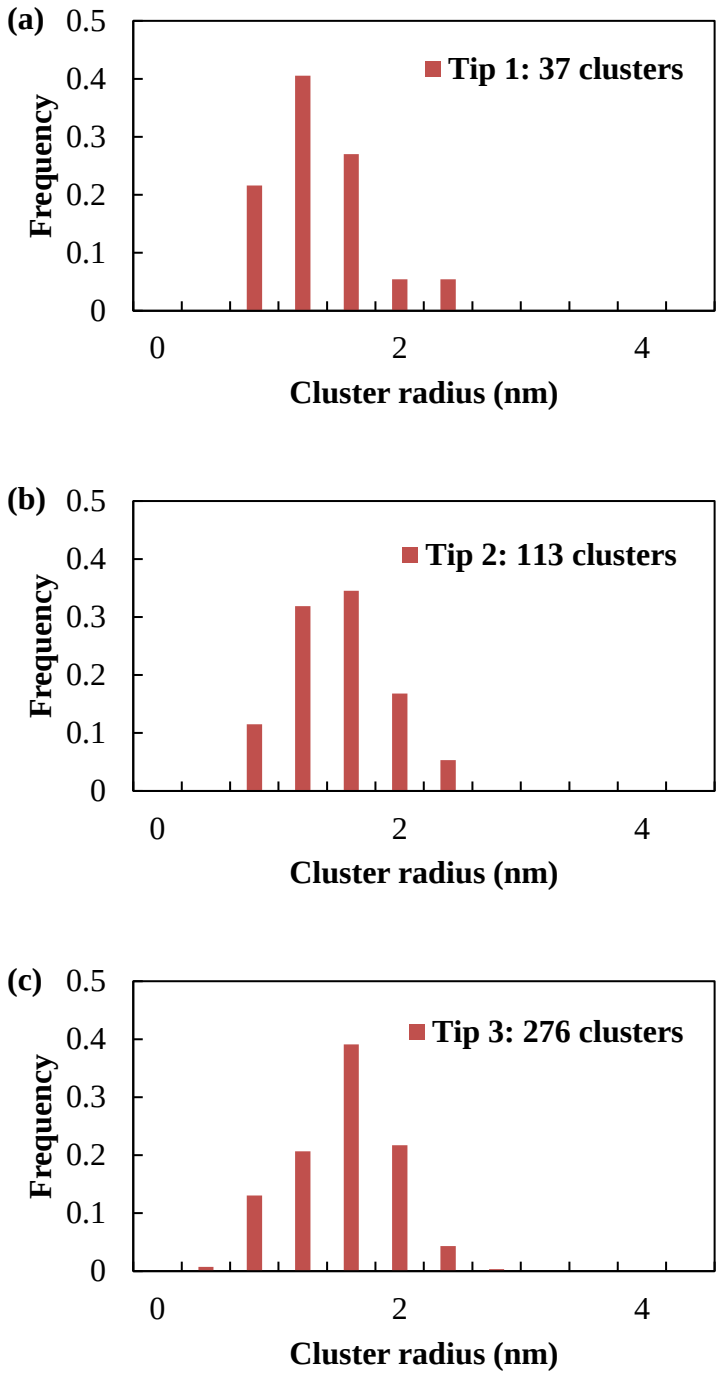

Fig. 3.4 Size distribution of the clusters with 0.4 nm bin width in three APT tips (a), (b), and (c) analyzed for Fe-0.5Cu when aged to maximum hardness

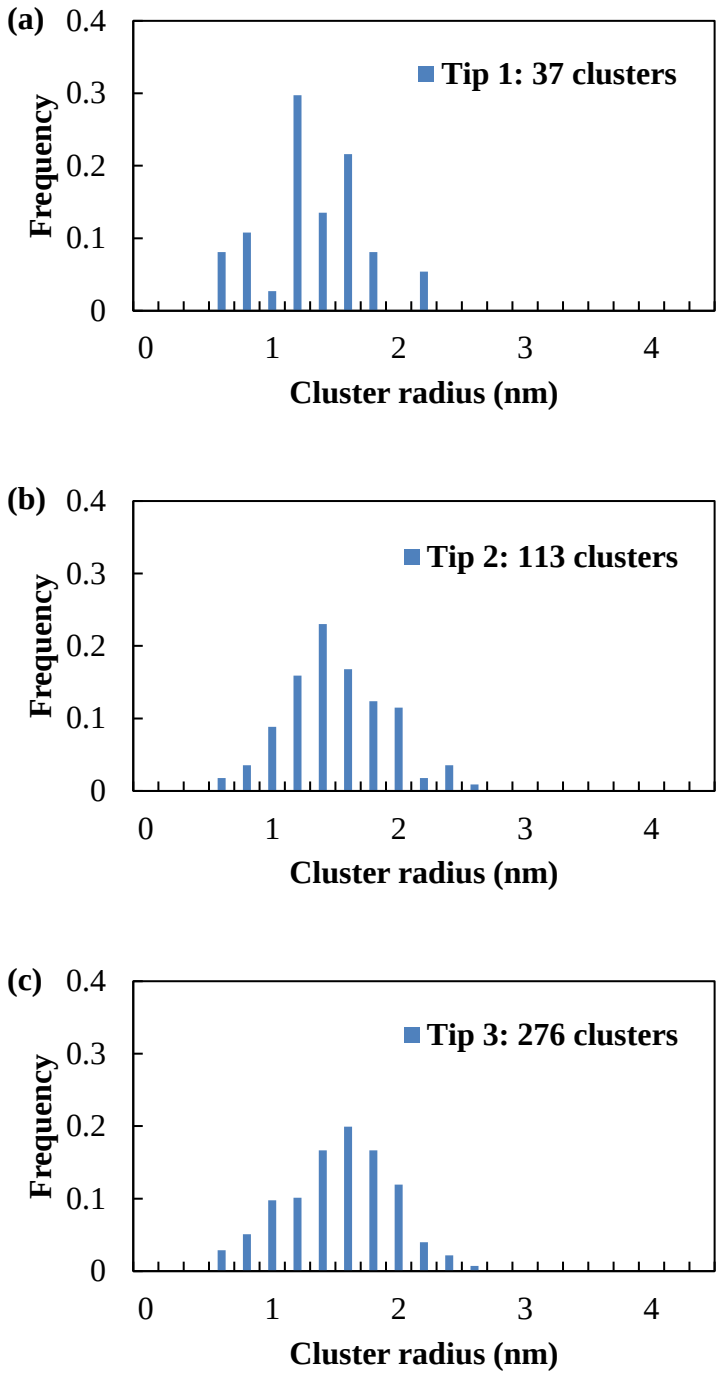

Fig. 3.5 Size distribution of the clusters with 0.2 nm bin width in three APT tips (a), (b), and (c) analyzed for Fe-0.5Cu when aged to maximum hardness

3.3 Summary

The size distribution of the clusters in Fe-0.5Cu when aged to maximum hardness was compared with and that in Fe-0.5Cu when aged plus irradiated. The comparison indicates that the subsequent neutron irradiation caused growth of the pre-existing clusters which were formed by thermal ageing and produced new clusters. This microstructural evolution agreed well with the expectation from experimental design and would be the basis for the investigation of effects of Ni, Mn, and Si.

References in chapter 3

[3-1] M. Kahlweit, Prog. Solid State Chem. 2 (1965) 134–174.

[3-2] F.S. Ham, J. Phys. Chem. Solids 6 (1958) 335–351.

[3-3] A.J. Markworth, J. Colloid Interface Sci. 38 (1972) 636–638.

[3-4] F. Christien, A. Barbu, J. Nucl. Mater. 324 (2004) 90–96.

[3-5] R.E. Stoller, L.R. Greenwood, in:, ASTM STP 1405, ASTM, 2001, pp. 204–217.

[3-6] R.S. Nelson, J.A. Hudson, D.J. Mazey, J. Nucl. Mater. 44 (1972) 318–330.

[3-7] N. Sekimura, T. Zama, H. Kawanishi, S. Ishino, J. Nucl. Mater. 141 (1986) 771–775.

[3-8] P. Chou, N.M. Ghoniem, J. Nucl. Mater. 117 (1983) 55–63.

[3-9] J.F. Ziegler, J.P. Biersack, in:, D.A. Bromley (Ed.), Treatise Heavy-Ion Sci., Springer US, 1985, pp. 93–129.

[3-10] R.A. Johnson, N.Q. Lam, Phys. Rev. B 15 (1977) 1794–1800.

[3-11] A.C. Arokiam, A.V. Barashev, D.J. Bacon, Y.N. Osetsky, Philos. Mag. Lett. 85 (2005) 491–501.

[3-12] A.C. Arokiam, A.V. Barashev, D.J. Bacon, Y.N. Osetsky, Philos. Mag. 87 (2007) 925–943.

Chapter 4 Effects of Ni and Mn in Cu-rich clusters

This chapter focuses on effects of Ni and Mn in Cu-rich clusters. First, effect of Ni in ternary alloys Fe-Cu-Ni is discussed. This is the basis for the study of effect of Mn and interaction between Ni and Mn in quaternary alloys Fe-Cu-Ni-Mn. Notably, the content of Ni in Fe-Cu-Ni and Fe-Cu-Ni-Mn is varied in small range to probe the interaction between Ni and Mn.

4.1 Effect of Ni in Cu-rich clusters

4.1.1 Solute clusters in Fe-Cu-Ni

The distribution of the clusters in size (cluster radius) in Fe-0.5Cu-0.6Ni and Fe-0.5Cu-0.8Ni are shown in Fig. 4.1 and 4.2, respectively. As in Fe-0.5Cu, thermal ageing produced high number density of clusters, and the sizes of the clusters showed a unimodal distribution with a peak at ~1.4 nm in both Fe-0.5Cu-0.6Ni and Fe-0.5Cu-0.8Ni. The subsequent neutron irradiation then increased the total cluster number density and altered the size distribution of the clusters into bimodal one. For both Fe-0.5Cu-0.6Ni and Fe-0.5Cu-0.8Ni, the peak at large radius region (as at ~1.6 nm in Fig. 4.1 and 4.2) clearly indicates that the subsequent neutron irradiation caused the growth of the pre-existing clusters formed during the thermal ageing. Meanwhile, the peak at small radius region (as at ~0.8 nm in Fig. 4.1 and 4.2) suggests that a group of new clusters were also produced by the neutron irradiation.

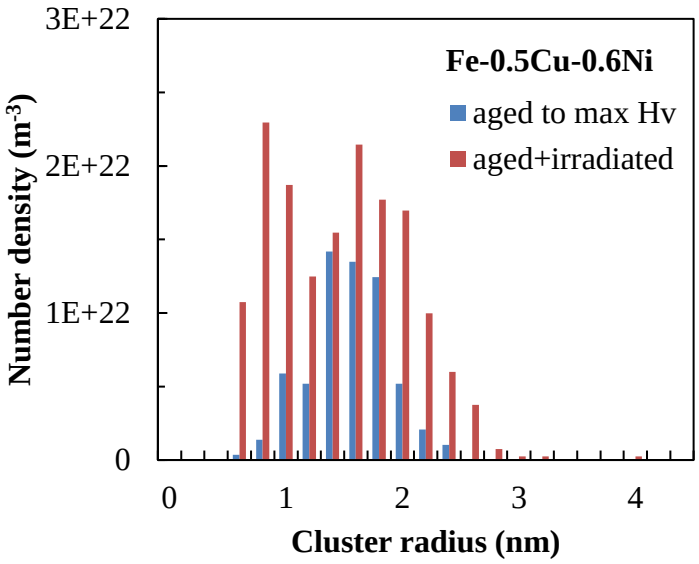

Fig. 4.1 Size distribution of the clusters in Fe-0.5Cu-0.6Ni when aged to maximum hardness, and when aged plus irradiated

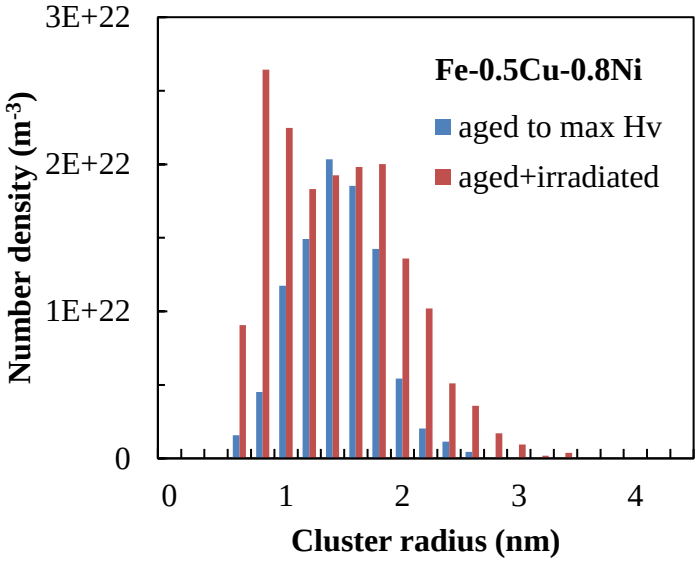

Fig. 4.2 Size distribution of the clusters in Fe-0.5Cu-0.8Ni when aged to maximum hardness, and when aged plus irradiated

The shapes and amplitudes of the size distribution curves for Fe-0.5Cu, Fe-0.5Cu-0.6Ni, and Fe-0.5Cu-0.8Ni were similar to each other when aged to maximum hardness, and when aged plus irradiated. To identify the difference of the clusters, the number density of total clusters in Fe-0.5Cu-0.6Ni and Fe-0.5Cu-0.8Ni was compared, as shown in Table 4.1. The data showed the trend of slightly larger number density of clusters in Fe-0.5Cu-0.8Ni than in Fe-0.5Cu-0.6Ni, which suggests a higher Ni alloying content increases the number density of clusters, to a slight extent.

Table 4.1 Number density of the clusters in Fe-0.5Cu-0.6Ni and Fe-0.5Cu-0.8Ni when aged to maximum hardness, and when aged plus irradiated ($\times 10^{23}$ m^{-3})

Alloy	Aged to max Hv	Aged+irradiated
Fe-0.5Cu-0.6Ni	0.61 (0.56/0.74)	1.58 (1.49/1.82)
Fe-0.5Cu-0.8Ni	0.95 (0.90/1.13)	1.71 (1.68/1.74)

*Note that the values are the weighted means of various measurements, where the weight for each measurement is the total number of atoms in the reconstructed tip. The minimum and maximum of various measurements are given in parenthesis.

Fig. 4.3 shows the Ni concentration distribution of the clusters in Fe-0.5Cu-0.6Ni and Fe-0.5Cu-0.8Ni, which is the cluster size dependence of the number of Ni atoms in the cluster. In the figure, each point indicates one cluster. When aged to maximum hardness, the Ni concentration in the clusters for both the alloys was well distributed along the line representing the mean content. This suggests that Ni atoms were included in the clusters at roughly the same concentration regardless of the cluster size. When aged plus irradiated, it was found that the neutron irradiation broadened the Ni concentration distribution curve

of the clusters. The clusters of Fe-0.5Cu-0.8Ni showed a slightly higher Ni concentration than those of Fe-0.5Cu-0.6Ni both when aged to maximum hardness and when aged plus irradiated. This implies that a higher Ni alloying content enhances the Ni concentration in the clusters. Nonetheless, this enhancing effect was weak in the studied alloys.

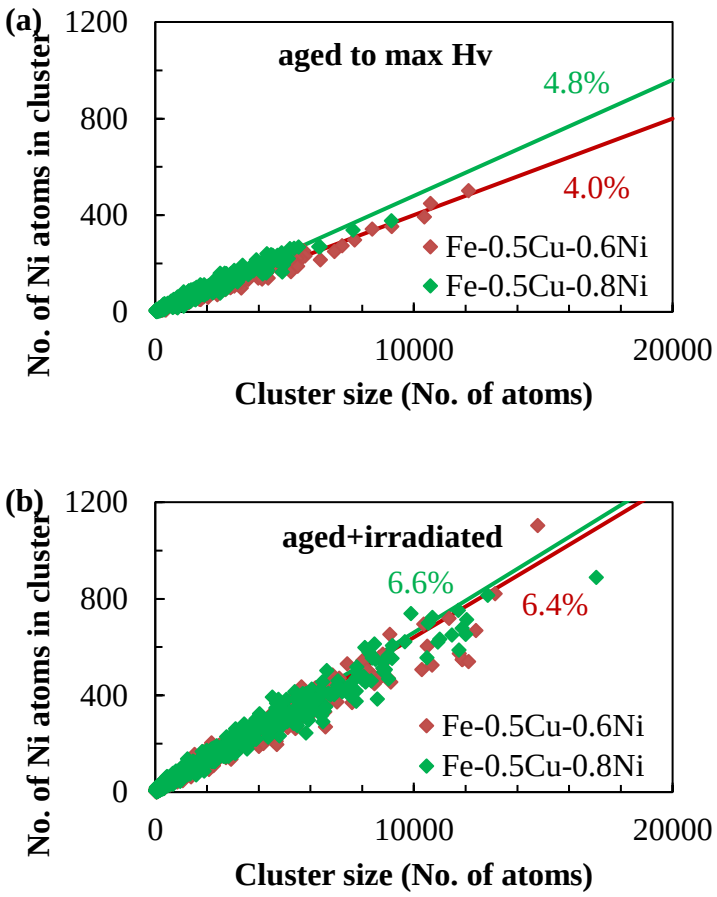

Fig. 4.3 Ni concentration distribution of the clusters in Fe-0.5Cu-0.6Ni and Fe-0.5Cu-0.8Ni: (a) when aged to maximum hardness, and (b) when aged plus irradiated

4.1.2 Effect of Ni

Ni entered the solute clusters, and exhibited the effect in increasing the number density

of the clusters. The size effect of the solute elements might have contributed to the increased number density of the clusters. The volume size factors of Cu, Ni, and Mn in α-Fe, which represent the fractional difference between the effective atomic volume of the solute and the atomic volume of Fe, are 17.53, 4.65, and 4.89%, respectively [4-1,2]. A Cu nucleus is supposed to have a larger lattice parameter than an Fe matrix since Cu is an oversized atom for an Fe matrix. This results in a misfit strain. In Fe matrix, the size of Ni is smaller than that of Cu. Therefore, when Ni is included in a Cu nucleus, the lattice parameter of the nucleus should decrease. This would decrease the strain energy barrier for the formation of clusters. This can reduce the formation energy of Cu nucleus, thus enhancing the Cu nucleation rate and increasing the number density of the clusters.

Another contribution to the increased cluster number density is revealed by a detailed cluster analysis for the studied alloys. By taking a composition profile across the clusters using the proxigram method, it was observed that Ni was enhanced at the cluster-matrix interface, as shown in Figure 4.4. The interfacial segregation of Ni in Cu-rich clusters has been observed in RPV model alloys and steels by many researchers, e.g. [4-3,4,5]. Seko et al. [4-6] investigated the sites preferred by Ni and found that Ni was energetically favored to be located at the cluster-matrix interface rather than at the cluster center or in the matrix. The ab initio calculations reported previously [4-7] suggest that a Cu-Ni binding is preferred in the Fe matrix. According to the Scientific Group Thermodata Europe (SGTE) solution database [4-8], the Ni–Fe interaction is weakly attractive, while the Cu-Fe interaction is strongly repulsive. Therefore, the presence of Ni at the Cu cluster interface would replace the strongly repulsive Cu-Fe bond with the attractive Cu-Ni bond in the nearest neighbor of Cu. This is energetically favored. Based on the above discussion,

it can be concluded that the formation energy of Cu nuclei in Fe matrix can decrease when Ni is present between Cu and Fe. This effect of Ni again enhances the Cu nucleation rate and increases the number density of the clusters. These mechanisms are in agreement with study of the non-classical nucleation theory by Zhang and Enomoto [4-9]. They showed that the formation energy of Cu nucleus reduces by the addition of Ni to binary Fe-Cu alloy.

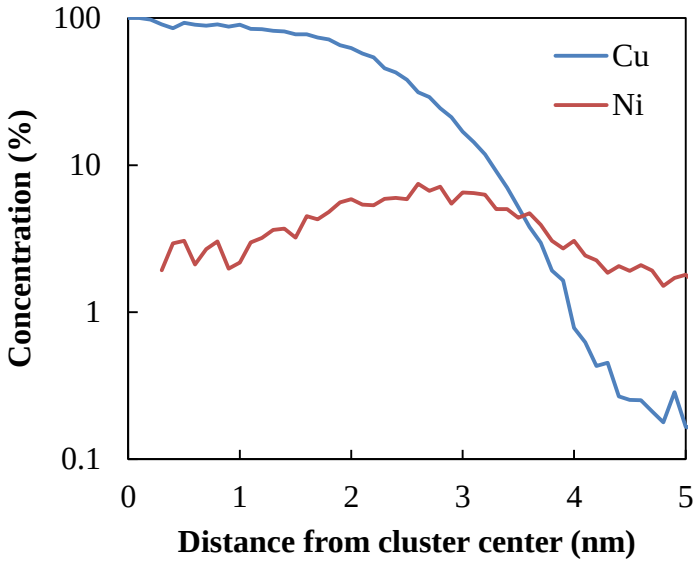

Fig. 4.4 Proxigram averaged over 10 Cu-rich clusters in Fe-0.5Cu-0.8Ni when aged plus irradiated

4.2 Effect of Mn in Cu-rich clusters

4.2.1 Solute clusters in Fe-Cu-Ni-Mn

The distribution of the clusters in size (cluster radius) in Fe-0.5Cu-0.6Ni-1.4Mn and Fe-

0.5Cu-0.8Ni-1.4Mn are shown in Fig. 4.5 and 4.6, respectively. Thermal ageing produced high number density of clusters, and the sizes of the clusters showed a unimodal distribution in both Fe-0.5Cu-0.6Ni-1.4Mn and Fe-0.5Cu-0.8Ni-1.4Mn, as in Fe-0.5Cu, Fe-0.5Cu-0.6Ni, and Fe-0.5Cu-0.8Ni. The subsequent neutron irradiation of both Fe-0.5Cu-0.6Ni-1.4Mn and Fe-0.5Cu-0.8Ni-1.4Mn then increased the number density of their clusters by about four times. This implies that the neutron irradiation of the alloys resulted in a substantial increase in the number density of the new clusters as the volume fraction of the clusters increased by about twice at the same time. It can also be seen from the figure that the irradiation broadened the size distribution curve of the clusters. The resulting size distribution curve had a long tail, which may indicate the growth of the pre-existing clusters formed by thermal ageing. However, there was a significant size overlapping between the new clusters formed by the subsequent irradiation and the pre-existing clusters formed by ageing. As a result, only one peak appeared explicitly at small radius region (as at ~1.2 nm in Fig. 4.5 and 4.6) in the statistical size distribution curve of the clusters when aged plus irradiated.

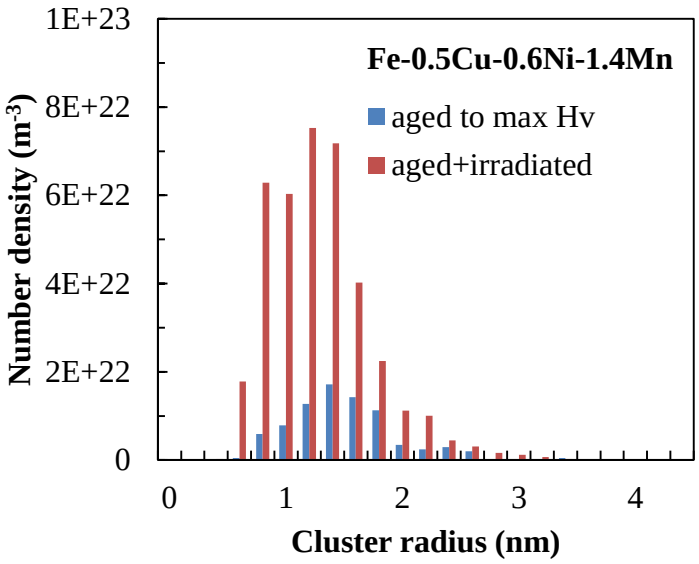

Fig. 4.5 Size distribution of the clusters in Fe-0.5Cu-0.6Ni-1.4Mn when aged to maximum hardness, and when aged plus irradiated

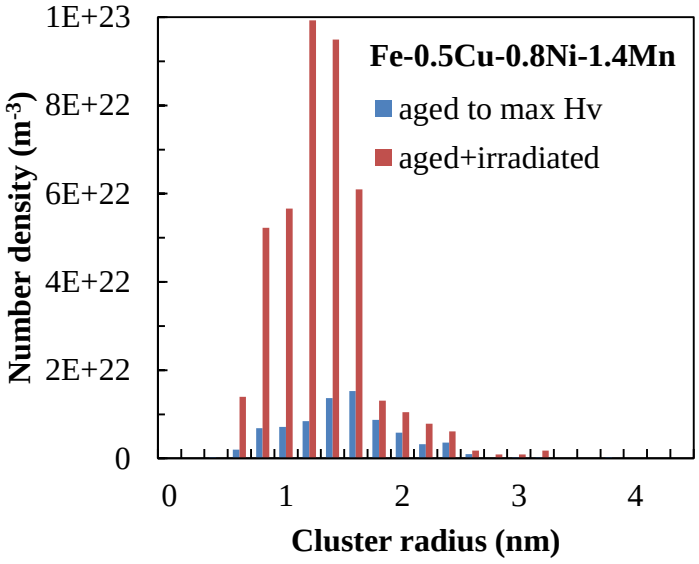

Fig. 4.6 Size distribution of the clusters in Fe-0.5Cu-0.8Ni-1.4Mn when aged to maximum hardness, and when aged plus irradiated

The composition distribution of the clusters in Fe-0.5Cu-0.6Ni-1.4Mn and Fe-0.5Cu-0.6Ni-1.4Mn when aged to maximum hardness is shown in Fig. 4.7. This composition distribution included both the Ni and Mn concentration distributions of the clusters. Again, both Ni and Mn concentrations were well distributed in the clusters along the mean composition line denoted by the solid lines. A similar trend was previously observed in the case of the Fe-Cu-Ni alloys when aged to maximum hardness. These observations indicate that Ni and Mn were included in the clusters at roughly the same concentration regardless of the cluster size.

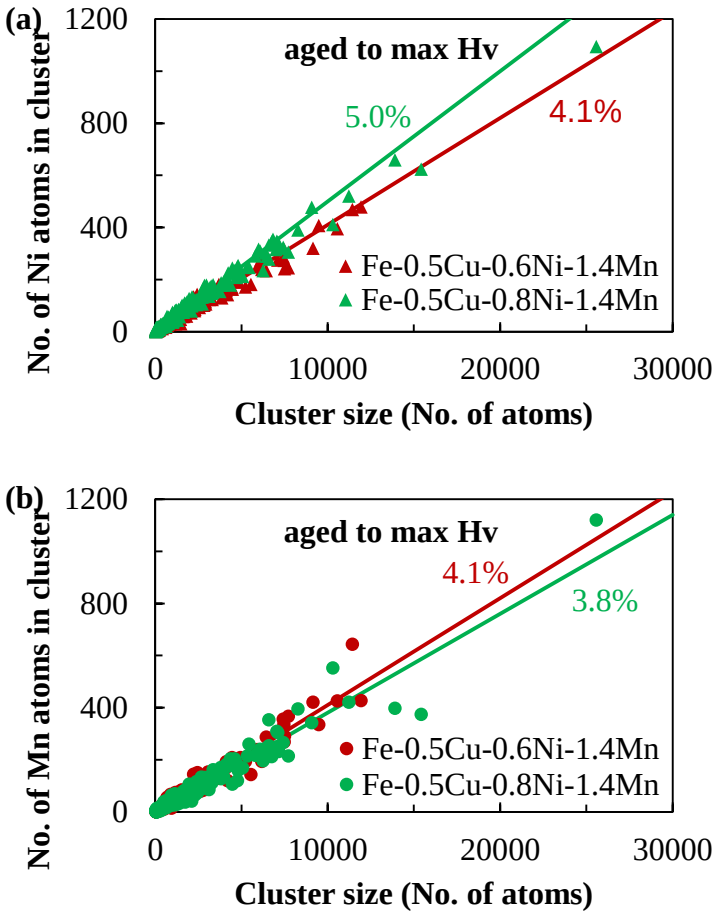

Fig. 4.7 Composition distribution of the clusters in Fe-0.5Cu-0.6Ni-1.4Mn and Fe-0.5Cu-0.8Ni-1.4Mn when aged to maximum hardness: (a) Ni concentration in the clusters, and (b) Mn concentration in the clusters

However, a clear difference in the cluster composition along with an increase in the cluster size was observed when aged plus irradiated, as illustrated in Fig. 4.8. In Figs. 4.8 (a)-(d), the solid line denotes the mean composition of all the clusters (more than 400 clusters measured for both the alloys when aged plus irradiated), and the two dotted lines represent the mean composition of 20 largest clusters and that of 20 medium-sized clusters. It was found that the Ni and Mn concentrations of the 20 largest clusters were lower than those of the 20 medium-sized clusters. The composition distribution of the clusters when aged plus irradiated shows the presence of two groups of clusters, which were distributed along the two dotted lines. Group 1 clusters were large in size and contained low concentrations of Ni and Mn, while group 2 clusters were small in size and contained high concentrations of Ni and Mn. Dohi et al. [4-10] studied Fe-Cu-Ni-Mn-Si alloys under neutron irradiation and reported that Ni, Mn, and Si atoms were included in the clusters at roughly the same concentration regardless of the cluster size. This trend was also observed in this study when aged to maximum hardness. Therefore, when aged plus irradiated, the group 1 clusters should correspond to the pre-existing clusters formed by ageing since such clusters contained low concentrations of Ni and Mn when aged to maximum hardness. On the other hand, the group 2 clusters were believed to be the new clusters formed by the subsequent irradiation. The Ni and Mn concentrations of the group 1 clusters when aged plus irradiated were higher than those of the clusters when aged to maximum hardness. This suggests that Ni and Mn atoms segregated more to the pre-existing clusters during the neutron irradiation. This can also imply the growth of the pre-existing clusters.

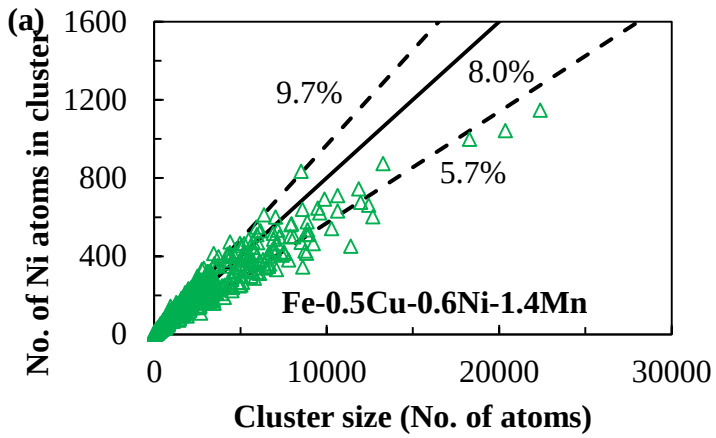
(a)
No. of Ni atoms in cluster
1600
1200
800
400
0
9.7%
8.0%
5.7%
Fe-0.5Cu-0.6Ni-1.4Mn
0
10000
20000
30000
Cluster size (No. of atoms)

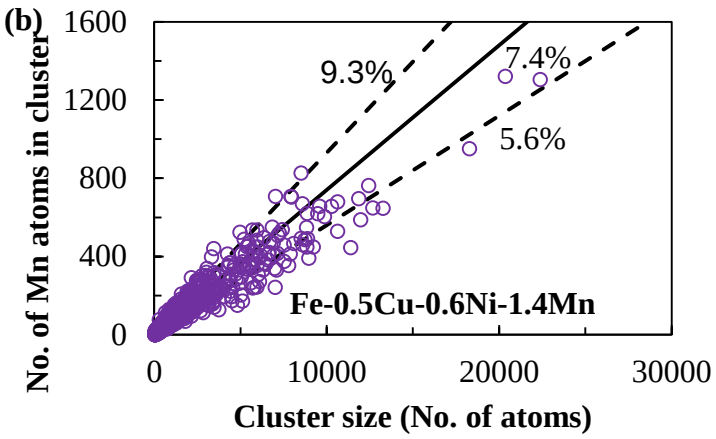
(b)
No. of Mn atoms in cluster
1600
1200
800
400
0
9.3%
7.4%
5.6%
Fe-0.5Cu-0.6Ni-1.4Mn
0
10000
20000
30000
Cluster size (No. of atoms)

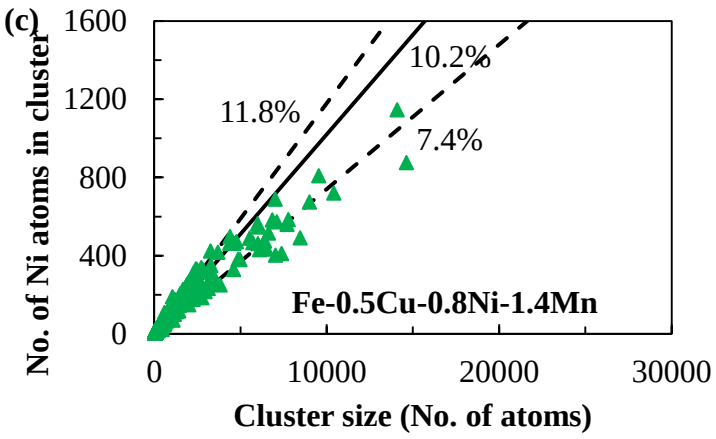
(c)
No. of Ni atoms in cluster
1600
1200
800
400
0
11.8%
10.2%
7.4%
Fe-0.5Cu-0.8Ni-1.4Mn
0
10000
20000
30000
Cluster size (No. of atoms)

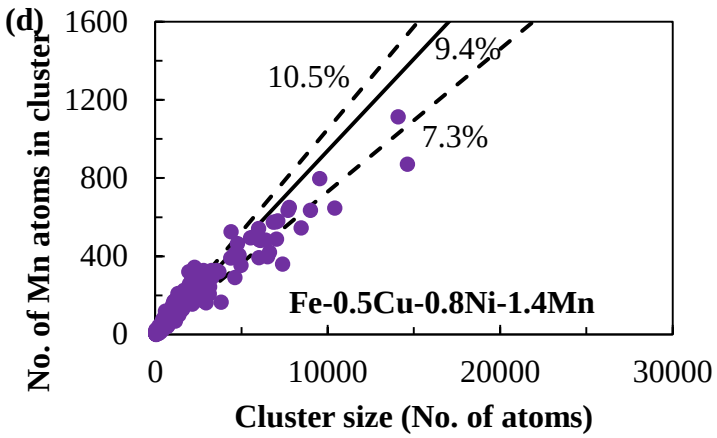

Fig.4.8 Composition distribution of the clusters when aged plus irradiated: (a) Ni concentration in the clusters in Fe-0.5Cu-0.6Ni-1.4Mn, (b) Mn concentration in the clusters in Fe-0.5Cu-0.6Ni-1.4Mn, (c) Ni concentration in the clusters in Fe-0.5Cu-0.8Ni-1.4Mn, and (d) Mn concentration in the clusters in Fe-0.5Cu-0.8Ni-1.4Mn

When aged plus irradiated, compared to Fe-0.5Cu-0.6Ni-1.4Mn, Fe-0.5Cu-0.8Ni-1.4Mn showed not only a higher Ni concentration but also a higher Mn concentration in the grown clusters (group 1) as well as in the new clusters (group 2). These results suggest that the higher Ni alloying content enhanced the Ni and Mn concentrations in the clusters. This enhancement effect was still manifested with the growth of the clusters. When aged to maximum hardness, the Mn concentration of the clusters in Fe-0.5Cu-0.8Ni-1.4Mn appeared to be slightly lower than that of the clusters in Fe-0.5Cu-0.6Ni-1.4Mn. This is unlikely to be a real effect. The absolute values of the Mn concentration in such clusters were small. The tip-to-tip variations in the APT measurements might have also confounded the solute effects. Liu et al. [4-11] carried out the thermal ageing of similar alloys at 450 ^{o}C. When aged to 24 h, the mean composition of the clusters was 34Cu-5.2Ni-4.2Mn, and 34Cu-6.7Ni-4.9Mn for Fe-0.5Cu-0.6Ni-1.4Mn, and Fe-0.5Cu-0.8Ni-

1.4Mn, respectively. These results agree with our observations that a higher Ni alloying content enhanced the Ni and Mn concentrations in the clusters.

To further discuss the cluster evolution in Fe-Cu-Ni-Mn during the neutron irradiation, a statistical analysis of cluster size distribution is conducted. The intention of this analysis is to check whether the cluster size distribution for the aged alloys can be fitted using a normal distribution and the cluster size distribution for the alloys aged plus irradiated can be fitted using a mixture of two normal distributions. Fig. 4.9 presents the cluster size distribution by APT analysis and the fitted normal distributions through a least-squares fit in Fe-0.5Cu-0.6Ni and Fe-0.5Cu-0.6Ni-1.4Mn. The practice in Fe-0.5Cu-0.6Ni indicates that the cluster size distribution can be represented by one normal distribution when aged to maximum hardness, and by a mixture of two normal distributions when aged plus irradiated, as shown in Fig. 4.9(a). When aged plus irradiated, the normal distribution in large radius region clearly demonstrates the growth of pre-existing clusters under the neutron irradiation. When it comes to Fe-0.5Cu-0.6Ni-1.4Mn, Fig. 4.9(b) shows that the cluster size distribution can be represented using one normal distribution when aged to maximum hardness, as expected. Besides, the statistical analysis can also detect two normal distributions when aged plus irradiated, even though the size overlapping between new clusters and pre-existing clusters is significant. The second normal distribution detected in large radius region demonstrates the growth of pre-existing clusters. This verifies our previous analysis that the pre-existing clusters can grow during the neutron irradiation.

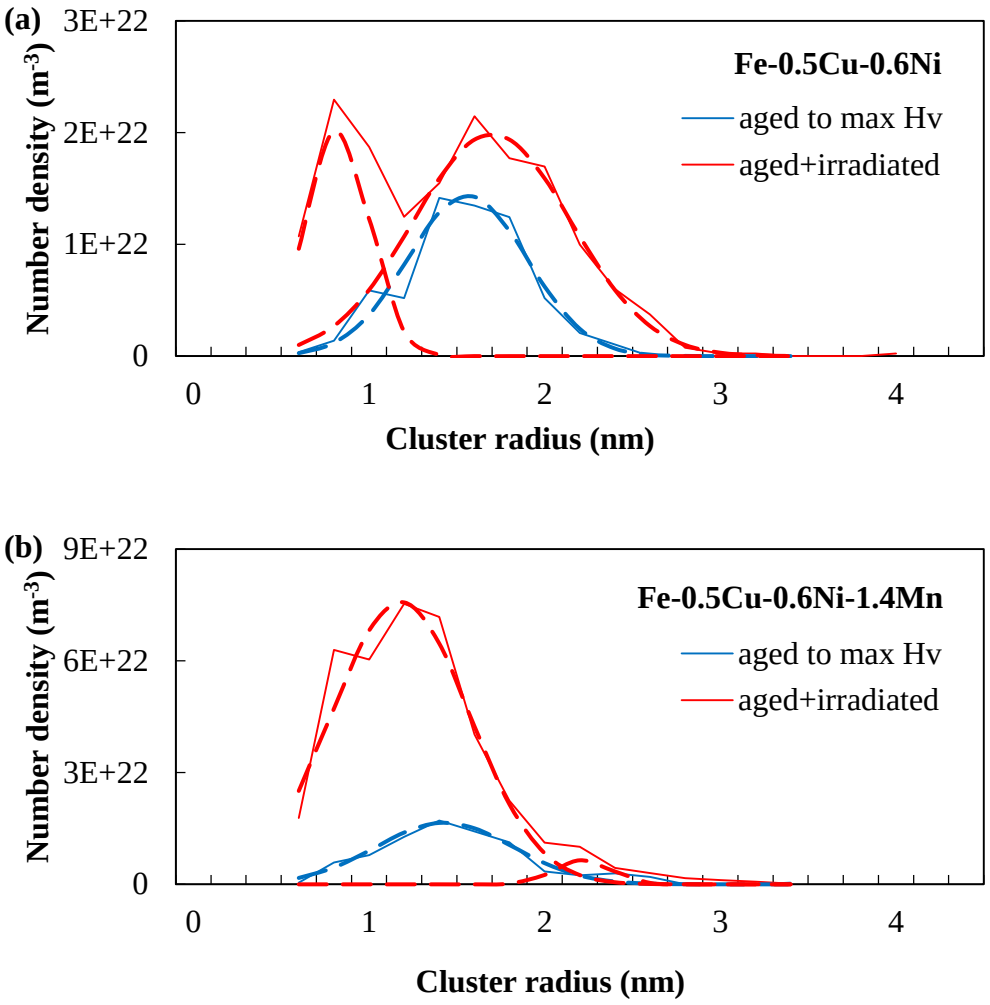

Fig. 4.9 Cluster size distribution and fitted normal distributions: (a) in Fe-0.5Cu-0.6Ni, and (b) in Fe-0.5Cu-0.6Ni-1.4Mn (Solid lines represent the cluster size distributions by APT analysis, and dotted lines represent the fitted normal distributions)

A detailed examination of the morphology of the clusters showed that some clusters appeared to exhibit preferential planes or directions. Fig. 4.10 shows the morphology of several large clusters in Fe-0.5Cu-0.6Ni-1.4Mn when aged plus irradiated. The top view in Fig. 4.10 (a) captures clusters No. 1, 2, 3, 4, and 5 with their longest axes and shortest axes in the 2D image, while the side view for individual cluster in Fig. 4.10 (b) displays

the cluster with its two long axes which appeared to be a preferential plane, especially for cluster No. 1, 3, and 4. The preferential plane of cluster No. 1 showed ~60 ^{o} angle with those of cluster No. 2, 3, and 5, and was parallel to that of cluster No. 4, as illustrated by the dotted lines in the figure. It is interesting to note that 60 ^{o} is one of the angles between {110} planes, and the atomistic simulations [4-12] showed that Cu clusters can exhibit faceting toward {110} planes of α-Fe matrix.

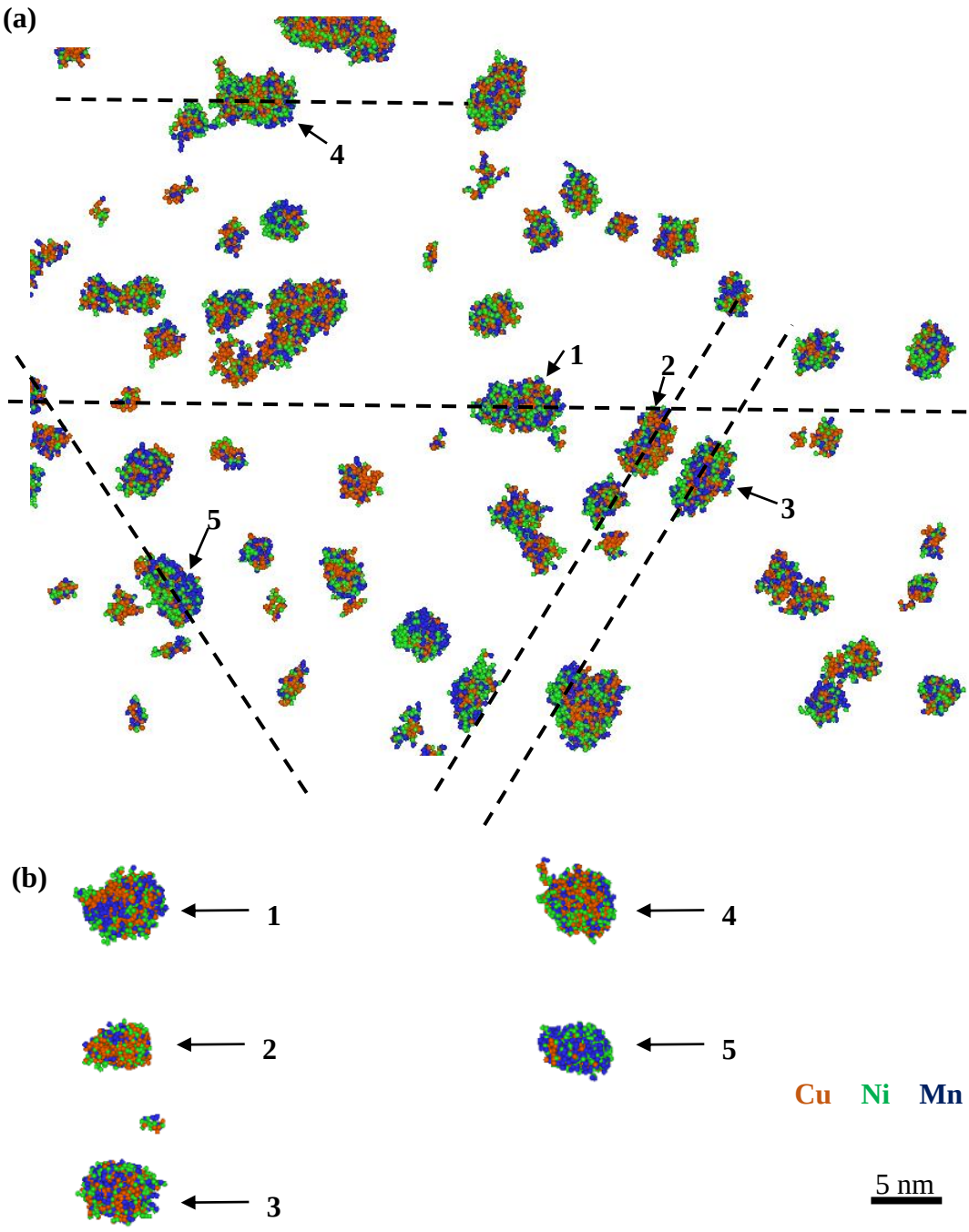

Fig. 4.10 Morphology of several large clusters in Fe-0.5Cu-0.6Ni-1.4Mn when aged plus irradiated: (a) top view, and (b) side view for individual cluster

4.2.2 Effect of Mn

When aged to maximum hardness, the Mn addition to Fe-Cu-Ni had little influence on the size distribution of the clusters. This is consistent with that the number density, volume fraction and mean radius of the clusters in Fe-Cu-Ni and Fe-Cu-Ni-Mn were similar, as shown in Appendix A.1. Fig. 4.11 shows the clustered Cu content of the alloys. The clustered Cu content remained unchanged when Mn was added to the alloy. However, the addition of Mn reduced the ageing time to reach the maximum hardness from 225 h (for Fe-Cu-Ni) to 90 h (for Fe-Cu-Ni-Mn). This implies that the process became 2.5 times as fast. These observations suggest that Mn accelerated the kinetic process of solute clustering during the thermal ageing.

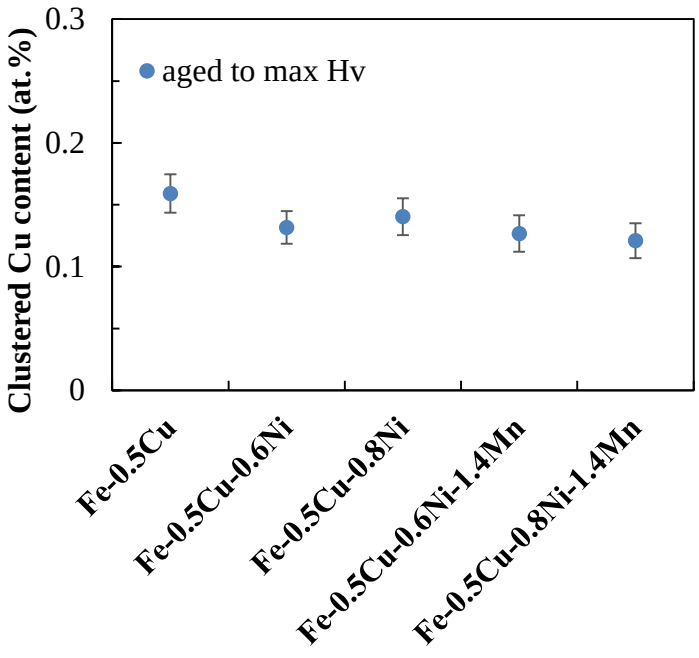

Fig. 4.11 Clustered Cu content in the alloys

(Error bar refers to the standard error of the mean)

The formation and evolution of solute clusters have been proposed to be described by a simplified cluster dynamics model based on kinetic equations [4-13]:

$$\frac{dC_n}{dt} = (\beta_{n-1}C_{n-1} - \alpha_n C_n) - (\beta_n C_n - \alpha_{n+1}C_{n+1}) \quad (4.1)$$

where C_n is the number density of a cluster of size n, α_n is the emission rate, and β_n is the capture rate. For the diffusion controlled clustering, both α_n and β_n can depend linearly on the solute diffusion rate [4-13]. Therefore, to reduce the ageing time from 225 to 90 h and to obtain a similar size distribution of the clusters, the solute diffusion rate should be increased from D_0 to $2.5D_0$. Under thermal ageing, the solute atoms diffuse via thermal vacancies and the solute diffusion rate, D, is given by [4-14]:

$$D = \alpha \times C_V \times D_V = \alpha \times \exp(-\frac{E_f^V}{kT}) \times \exp\left(-\frac{E_m^V}{kT}\right) \quad (4.2)$$

where C_V is the concentration of thermal vacancies and D_V is the vacancy migration rate. C_V and D_V depend on the formation energy and migration energy of thermal vacancies, respectively. The increment of D from D_0 to $2.5D_0$ needs a reduction in the vacancy formation energy or the vacancy migration energy of 0.06 eV. Murakami et al. [4-15] studied the effect of Mn addition to pure Fe using electrical resistivity measurements and concluded that Mn traps the vacancy-type defects and prevents the migration of vacancies at around 0 ^{o}C. Therefore, for Mn, the effect in reducing the vacancy formation energy is more plausible. In fact, Olsson et al. [4-16] found a strong binding between Mn and the vacancy up to the third nearest neighbor because of the magnetic coupling. This long-range Mn-vacancy interaction may contribute to the reduction in the vacancy formation energy, thus accelerating the solute diffusion during thermal ageing.

During the subsequent neutron irradiation, the addition of Mn to Fe-Cu-Ni largely

increased the number density of Cu-rich clusters even though the clustered Cu content was almost unchanged. The large increase of cluster number density is consistent with the results reported by Miller et al. [4-17]. Their APT data showed that upon neutron irradiation to ~1×10^{19} n/cm^2 (E > 1 MeV), Fe-0.78at.%Cu-1.05at.%Mn showed a number density of clusters that was approximately an order of magnitude higher than that for Fe-0.80at.%Cu. As mentioned previously, in α-Fe, the size of Mn is smaller than that of the oversized Cu atom. The addition of Mn to the Cu nucleus can reduce the formation energy of the Cu nucleus through the lowering of the misfit strain energy barrier. Interfacial segregation of Mn in Cu-rich clusters was observed in the Fe-Cu-Ni-Mn alloys, as shown in Fig. 4.12. Similar to the Ni effect, the interfacial segregation of Mn can be energetically favored since the Cu-Mn binding in the Fe matrix is also preferred [4-7]. Then the presence of Mn between Cu and Fe may also decrease the formation energy of the Cu nucleus in an Fe matrix by replacing the Cu-Fe bond with Cu-Mn bond. The effect of Mn in reducing the formation energy of the Cu nucleus agrees with the non-classical nucleation theory study of Zhang and Enomoto [4-9]. They reported that the addition of Mn to binary Fe-Cu alloy reduced the formation energy of the Cu nucleus. This Mn effect enhances the Cu nucleation rate, resulting in a higher number density of the clusters.

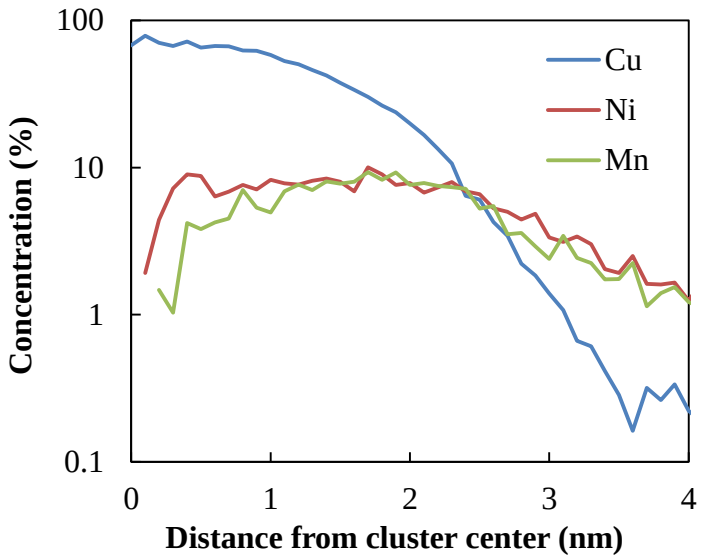

Fig. 4.12 Proxigram averaged over 10 Cu-rich clusters in Fe-0.5Cu-0.8Ni-1.4Mn when aged plus irradiated

However, this should not be the only effect of Mn that occurred in the Fe-Cu-Ni-Mn alloys since the effect of Mn in increasing the cluster number density was much more significant than the effect of Ni during the neutron irradiation. It is interesting that Mn had almost no impact on the microstructure and the consumption amount of matrix Cu when aged to maximum hardness. Whereas, under the condition of neutron irradiation, the Mn addition to Fe-Cu-Ni increased largely number density of Cu-rich clusters even though the consumption amount of matrix Cu was almost unchanged. This difference in Mn effect can arise from the change of the environment from thermal ageing to neutron irradiation. The contribution may be that the irradiation produced SIAs bind with Mn to form SIA-Mn clusters. These SIA-Mn clusters can server as nuclei of Cu-rich clusters, thus enhancing the formation of Cu-rich clusters.

The strong interaction between Mn and SIAs has been reported both theoretically and experimentally. The ab initio calculations of Vincent et al. [4-18] showed that the mixed Mn-SIA dumbbell configuration was very stable and that the mixed dumbbell was likely to migrate because of its low energy for the mixed-to-mixed migration. The transmission electron microscopy (TEM) study by Yabuuchi et al. [4-19] revealed that under neutron irradiation, the addition of Mn to pure Fe increases the number density of dislocation loops. They interpreted their results by that Mn serves as a nucleus of the loop by trapping SIAs and clusters. Therefore, it can be concluded that the formation of SIA-Mn clusters is very plausible. It is interesting that the atomistic Monte Carlo study by Ngayam-Happy et al. [4-20] predicted that small Mn-rich clusters associated with SIAs can form very quickly via a fast interstitial-driven mechanism, and the formation of such clusters is faster than even Cu nucleation which occurs via a slower vacancy-driven mechanism. This is also consistent with the assumption that SIA-Mn clusters form. Since SIA-Mn clusters can act as sinks of vacancies, the SIA-Mn clusters can be the nuclei of Cu-rich clusters with the mechanism where Cu atoms diffuse by the vacancy mechanism towards SIA-Mn clusters. This might have increased the rate of formation of Cu-rich clusters.

4.3 Interaction of Ni and Mn

In the Fe-Cu-Ni alloys, an increase of Ni alloying content from 0.6% to 0.8% enhanced only slightly Ni concentration in the clusters. While in the Fe-Cu-Ni-Mn alloys, the increase of Ni alloying content from 0.6% to 0.8% enhanced clearly concentrations of both Ni and Mn in the clusters. The APT data obtained under the condition of ageing plus irradiation also indicate that the addition of Mn to Fe-Cu-Ni enhanced the Ni

concentration in the clusters, even though the pre-ageing time for Fe-Cu-Ni and Fe-Cu-Ni-Mn was different. Previous APT data by Liu et al. [4-11] also showed that the addition of Mn to Fe-Cu-Ni alloys that are not pre-aged and are only neutron-irradiated enhances the Ni concentration in the clusters. These results appear to suggest an attractive interaction of Ni and Mn. This attractive interaction can serve as a driving force for enhanced concentrations of Ni and Mn in the clusters: Mn in the clusters attracts Ni, and the higher Ni attracts more Mn into the clusters, which is consistent with the prediction of Odette and Wirth [4-21].

This Ni-Mn interaction appears to rationalize the results of previous studies on RPV steels. Miller et al. [4-22] studied two neutron-irradiated RPV steel welds with different bulk Ni contents and the APT results showed that the 1.2wt.%Ni weld had not only a higher Ni concentration but also a higher Mn concentration in the clusters than the 0.6wt.%Ni weld. However, the weld with a higher bulk Ni content had a slightly lower bulk Mn content than the weld with a lower Ni content. A similar phenomenon was observed in the study of Carter et al. [4-23]. The clusters in the 1.00wt.%Ni weld had a higher Mn content than those in the 0.58wt.%Ni weld even though the bulk Mn content of the 1.00wt.%Ni weld was slightly lower than that of the 0.58wt.%Ni weld. Buswell et al. [4-24] investigated a series of RPV steels with a similar bulk Mn content under neutron irradiation. Unlike the ~0.8wt.%Ni steels JPG27 and JRQ41, the 1.17wt.%Ni steel JPH2 produced clusters with higher Mn content as well as higher Ni content. These observations of the higher Mn concentration in the clusters can be caused by the higher bulk Ni content.

To understand the interaction of Ni and Mn, the Ni and Mn concentrations in each cluster

of Fe-Cu-Ni-Mn were compared. Fig. 4.13 shows the cluster distribution when aged plus irradiated where each point represents one cluster. With the increase of cluster size, the Ni and Mn contents in the cluster showed a trend of 1:1 relation. More importantly, this 1:1 Ni-Mn relation in the clusters remained unchanged even when the Ni alloying content was varied from 0.6 to 0.8%. Similar Ni-Mn relation in the clusters was also observed when the alloys were aged to maximum hardness. This indicates that the 1:1 Ni-Mn relation can be thermodynamically favoured.

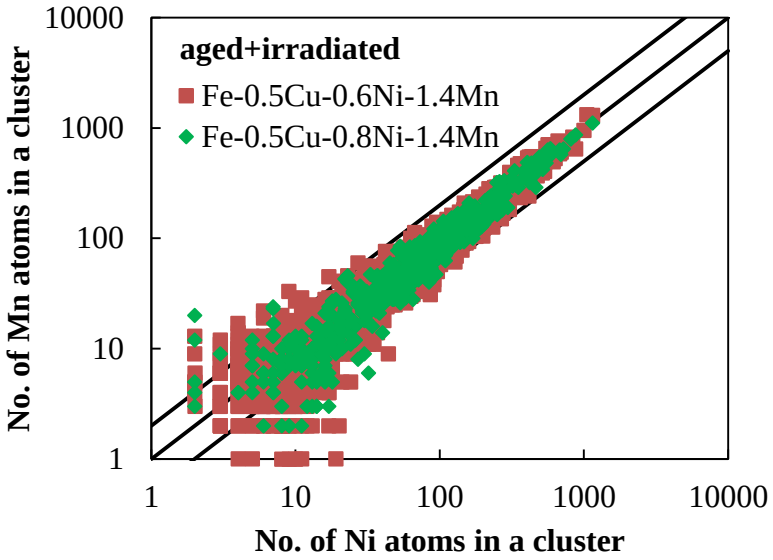

Fig. 4.13 Relationship between number of Ni atoms and number of Mn atoms in the clusters in Fe-0.5Cu-0.6Ni-1.4Mn and Fe-0.5Cu-0.8Ni-1.4Mn when aged plus irradiated (Solid lines represent 2:1, 1:1, and 1:2)

Furthermore, the distributions of Ni and Mn in the clusters were investigated. Fig. 4.14 illustrates the morphology of typical large clusters in the Fe-Cu-Ni-Mn alloy. The cluster took a shape of ellipsoid and in the cluster the distribution of Ni atoms was spatially

similar to the distribution of Mn atoms. To quantitatively describe the relationship between Ni distribution and Mn distribution in the cluster, cluster Ni radius r_{Ni} and cluster Mn radius r_{Mn} were defined. It is know that the radius (Guinier radius) of a cluster r is defined as:

$$r = \sqrt{\frac{5}{3}} \times \sqrt{\frac{1}{n}\sum_{i=1}^{n}\{(x_i - x_c)^2 + (y_i - y_c)^2 + (z_i - z_c)^2\}} \quad (4.3)$$

where (x_c, y_c, z_c) is the coordinates of mass center of the cluster, and (x_i, y_i, z_i) defines the position of an individual atom in the cluster. Similarly, the cluster Ni radius r_{Ni} is defined when (x_i, y_i, z_i) defines the position of an individual Ni atom in the cluster, and the cluster Mn radius r_{Mn} is defined when (x_i, y_i, z_i) defines the position of an individual Mn atom in the cluster. Fig. 4.15 shows the relationship between cluster Ni radius and cluster Mn radius in Fe-0.5Cu-0.6Ni-1.4Mn and Fe-0.5Cu-0.8Ni-1.4Mn. In the figure, each point represents one cluster. The cluster Ni radius was almost equal to the cluster Mn radius, indicating similar distributions of Ni and Mn in the clusters.

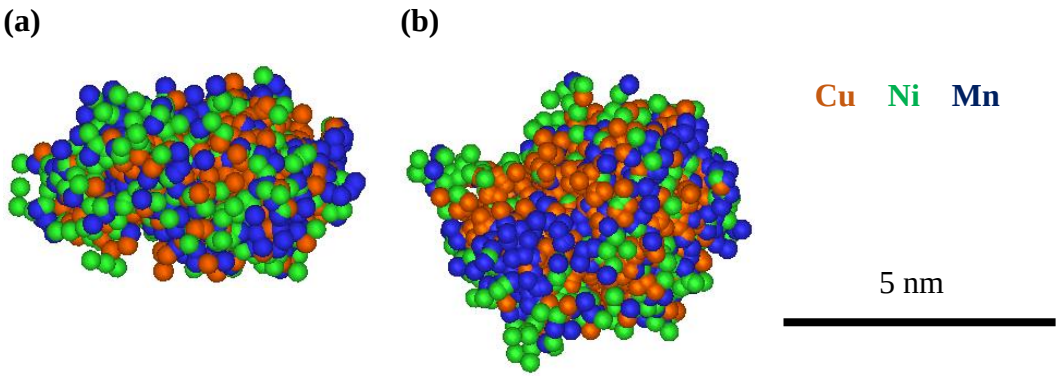

Fig. 4.14 Atom maps of a typical large cluster in Fe-0.5Cu-0.6Ni-1.4Mn when aged plus irradiated: (a) top view, and (b) side view

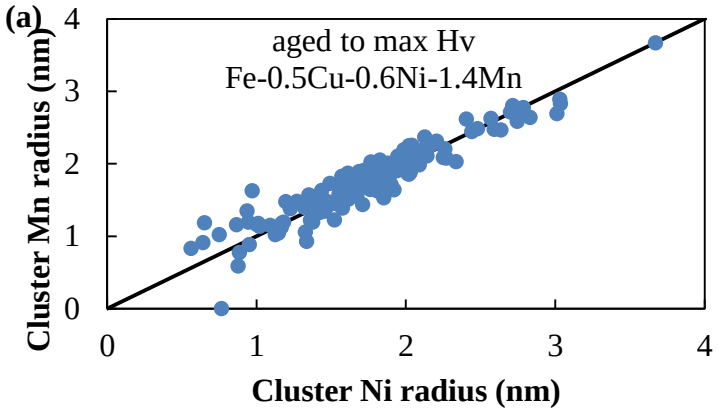
(a)
aged to max Hv
Fe-0.5Cu-0.6Ni-1.4Mn
Cluster Mn radius (nm)
Cluster Ni radius (nm)
0
1
2
3
4

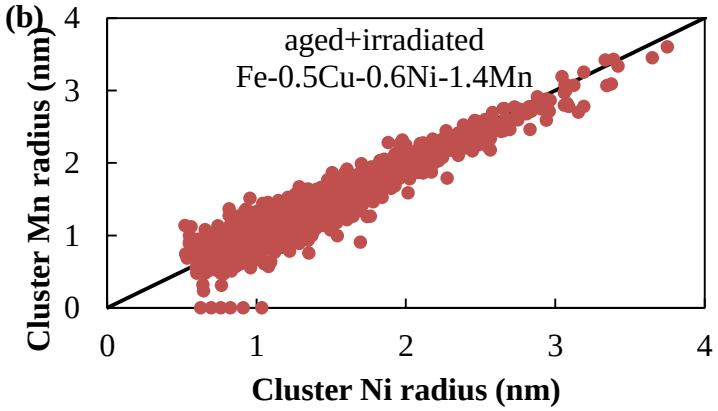
(b)
aged+irradiated
Fe-0.5Cu-0.6Ni-1.4Mn
Cluster Mn radius (nm)
Cluster Ni radius (nm)
0
1
2
3
4

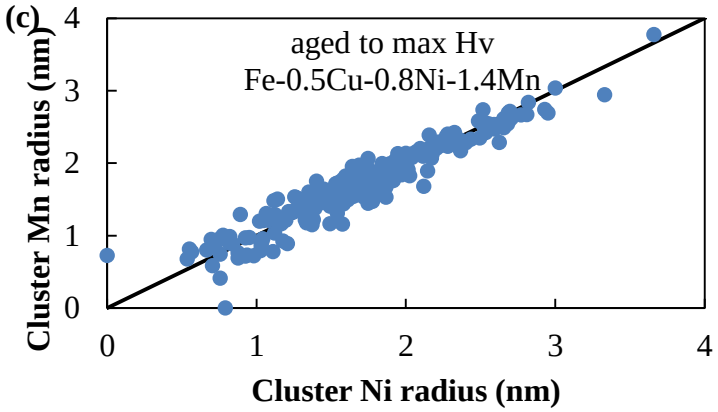
(c)
aged to max Hv
Fe-0.5Cu-0.8Ni-1.4Mn
Cluster Mn radius (nm)
Cluster Ni radius (nm)
0
1
2
3
4

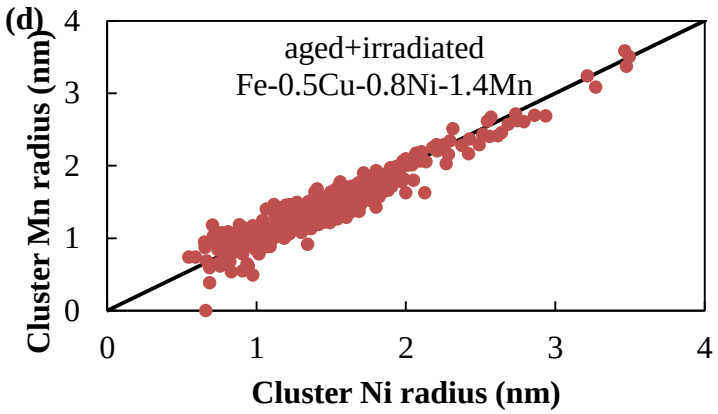

Fig. 4.15 Relationship between cluster Ni radius and cluster Mn radius in (a) Fe-0.5Cu-0.6Ni-1.4Mn when aged to maximum hardness, (b) Fe-0.5Cu-0.6Ni-1.4Mn when aged plus irradiated, (c) Fe-0.5Cu-0.8Ni-1.4Mn when aged to maximum hardness, and (d) Fe-0.5Cu-0.8Ni-1.4Mn when aged plus irradiated (Solid line represents 1:1)

The 1:1 Ni-Mn relation in terms of cluster composition and the almost equivalent cluster Ni radius and cluster Mn radius appear to suggest that Ni and Mn might form ordered phase in the clusters. It is interesting to note that in the Ni-Mn binary alloy phase diagram, an intermetallic at 50%Mn (Ni) occurs. In addition, in the Fe-Cu-Ni-Mn system, the interatomic potential developed by Bonny et al. [4-25] showed that Ni_2Mn_2 was energetically more stable than the other clusters ($NiMn_2$, Ni_2Mn, $NiMn_3$, and Ni_3Mn). These results are consistent with the present experimental observations.

4.4 Summary

This chapter investigated effects of Ni and Mn in Cu-rich clusters using the alloys Fe-0.5Cu-0.6Ni, Fe-0.5Cu-0.8Ni, Fe-0.5Cu-0.6Ni-1.4Mn, and Fe-0.5Cu-0.8Ni-1.4Mn. The

main results are summarized as follows:

(1) Regarding effect of Ni, the higher Ni alloying content increased the number density of Cu-rich clusters, to a slight extent. It is suggested that Ni can reduce the formation energy of Cu nuclei, thus enhancing the Cu nucleation rate.

(2) Regarding effect of Mn, the addition of Mn to Fe-Cu-Ni reduced the ageing time required to achieve a similar microstructure of the Cu-rich clusters (the condition of ageing to maximum hardness) from 225 to 90 h. This indicates that Mn can accelerate the solute diffusion via thermal vacancies, thereby accelerating the kinetic process of solute clustering. During the neutron irradiation, Mn significantly increased the number density of Cu-rich clusters. Mn can reduce the formation energy of Cu nuclei, thus enhancing the Cu nucleation rate. However, unlike the weak Ni effect, such significant Mn effect should also imply other important mechanisms. It is suggested that Mn may enhance the heterogeneous nucleation of Cu clusters through the formation of SIA-Mn clusters, since Mn had almost no impact on the number density of Cu-rich clusters when aged to maximum hardness. The SIA-Mn clusters can serve as nuclei of Cu-rich clusters.

(3) Regarding interaction of Ni and Mn, in Fe-Cu-Ni a high Ni alloying content enhanced only slightly Ni concentration in the clusters, whereas in Fe-Cu-Ni-Mn the high Ni alloying content enhanced clearly concentrations of Ni and Mn in the clusters. The addition of Mn to Fe-Cu-Ni also enhanced the Ni concentration in the clusters. These results can suggest an attractive interaction between Ni and Mn, which can serve as a driving force for enhanced concentrations of Ni and Mn in the clusters: Mn in the clusters attracts Ni, and the higher Ni attracts more Mn into the clusters. A 1:1 Ni-Mn concentration relation was found in the clusters of the alloys with different Ni

alloying contents, Fe-0.5Cu-0.6Ni-1.4Mn and Fe-0.5Cu-0.8Ni-1.4Mn. This indicates that the 1:1 Ni-Mn relation can be thermodynamically favoured. Moreover, the cluster Ni radius was almost equal to the cluster Mn radius, implying similar distributions of Ni and Mn in the clusters.

References in chapter 4

[4-1] H.W. King, J. Mater. Sci. 1 (1966) 79–90.

[4-2] E. Vincent, C.S. Becquart, C. Domain, Nucl. Instrum. Methods Phys. Res. Sect. B Beam Interact. Mater. At. 228 (2005) 137–141.

[4-3] A. Cerezo, S. Hirosawa, I. Rozdilsky, G.D.W. Smith, Philos. Trans. R. Soc. Lond. Math. Phys. Eng. Sci. 361 (2003) 463–477.

[4-4] R. Monzen, K. Takada, C. Watanabe, ISIJ Int. 44 (2004) 442–444.

[4-5] P.D. Styman, J.M. Hyde, K. Wilford, D. Parfitt, N. Riddle, G.D.W. Smith, Ultramicroscopy 159, Part 2 (2015) 292–298.

[4-6] A. Seko, S.R. Nishitani, I. Tanaka, H. Adachi, E.F. Fujita, Calphad 28 (2004) 173–176.

[4-7] L. Malerba, G.J. Ackland, C.S. Becquart, G. Bonny, C. Domain, S.L. Dudarev, C.-C. Fu, D. Hepburn, M.C. Marinica, P. Olsson, R.C. Pasianot, J.M. Raulot, F. Soisson, D. Terentyev, E. Vincent, F. Willaime, J. Nucl. Mater. 406 (2010) 7–18.

[4-8] B. Jansson, M. Schalin, M. Selleby, B. Sundman, in:, Mater Soc CIM, Quebec, 1993, p. 57.

[4-9] C. Zhang, M. Enomoto, Acta Mater. 54 (2006) 4183–4191.

[4-10] K. Dohi, K. Nishida, A. Nomoto, N. Soneda, H. Watanabe, 3D atom probe observation of heavy ion irradiated model alloys for reactor pressure vessel steels, CRIEPI Report Q08029, 2009.

[4-11] L. Liu, K. Nishida, K. Dohi, A. Nomoto, N. Soneda, K. Murakami, Z. Li, D. Chen, N. Sekimura, J. Nucl. Sci. Technol. 53 (2016) 1546–1553.

[4-12] P. Erhart, J. Marian, B. Sadigh, Phys. Rev. B 88 (2013) 024116.

[4-13] A. Barbu, E. Clouet, Solid State Phenom. 129 (2007) 51–58.

[4-14] G.S. Was, Fundamentals of Radiation Materials Science: Metals and Alloys, Springer, 2007.

[4-15] K. Murakami, T. Iwai, H. Abe, N. Sekimura, Y. Katano, T. Iwata, T. Onitsuka, Philos. Mag. 95 (2015) 1680–1695.

[4-16] P. Olsson, T.P.C. Klaver, C. Domain, Phys. Rev. B 81 (2010) 054102.

[4-17] M.K. Miller, B.D. Wirth, G.R. Odette, Mater. Sci. Eng. A 353 (2003) 133–139.

[4-18] E. Vincent, C.S. Becquart, C. Domain, J. Nucl. Mater. 359 (2006) 227–237.

[4-19] K. Yabuuchi, M. Saito, R. Kasada, A. Kimura, J. Nucl. Mater. 414 (2011) 498–502.

[4-20] R. Ngayam-Happy, C.S. Becquart, C. Domain, L. Malerba, J. Nucl. Mater. 426 (2012) 198–207.

[4-21] G.R. Odette, B.D. Wirth, J. Nucl. Mater. 251 (1997) 157–171.

[4-22] M.K. Miller, K.F. Russell, M.A. Sokolov, R.K. Nanstad, J. Nucl. Mater. 361 (2007) 248–261.

[4-23] R.G. Carter, N. Soneda, K. Dohi, J.M. Hyde, C.A. English, W.L. Server, J. Nucl. Mater. 298 (2001) 211–224.

[4-24] J.T. Buswell, W.J. Phythian, R.J. McElroy, S. Dumbill, P.H.N. Ray, J. Mace, R.N. Sinclair, J. Nucl. Mater. 225 (1995) 196–214.

[4-25] G. Bonny, D. Terentyev, A. Bakaev, E.E. Zhurkin, M. Hou, D. Van Neck, L. Malerba, J. Nucl. Mater. 442 (2013) 282–291.

Chapter 5 Effect of Si in Cu-rich clusters

This chapter focuses on effect of Si in Cu-rich clusters through the investigation of ternary alloys Fe-0.5Cu-0.1Si and Fe-0.5Cu-0.2Si under neutron irradiation following thermal ageing, compared to binary alloy Fe-0.5Cu.

5.1 Solute clusters in Fe-Cu-Si

The distribution of the clusters in size (cluster radius) in Fe-0.5Cu-0.1Si and Fe-0.5Cu-0.2Si are shown in Fig. 5.1 and 5.2, respectively. Thermal ageing produced high number density of clusters, and the sizes of the clusters showed a unimodal distribution with a peak at ~1.4 nm in both Fe-0.5Cu-0.1Si and Fe-0.5Cu-0.2Si. For Fe-0.5Cu-0.1Si, the shape and amplitude of the size distribution curve were similar to those for Fe-0.5Cu both when aged to maximum hardness and when aged plus irradiated. Moreover, the number density of total clusters in Fe-0.5Cu and Fe-0.5Cu-0.1Si was almost the same: 0.74×10^{23} and 0.78×10^{23} m^{-3} for Fe-0.5Cu and Fe-0.5Cu-0.1Si respectively when aged to maximum hardness, and 1.39×10^{23} and 1.43×10^{23} m^{-3} for Fe-0.5Cu and Fe-0.5Cu-0.1Si respectively when aged plus irradiated. Therefore, the growth of the pre-existing clusters formed by thermal ageing and the formation of new clusters during the subsequent neutron irradiation was demonstrated in Fe-0.5Cu-0.1Si. It is also indicated that the effect of 0.1%Si on the solute clusters was not significant. It is interesting to observe that the subsequent irradiation had almost no impact on the number density of total clusters in the case of Fe-0.5Cu-0.2Si. Moreover, when aged plus irradiated the size distribution of the clusters in Fe-0.5Cu-0.2Si was similar to that of the clusters in Fe-0.5Cu (as well as that of the clusters in Fe-0.5Cu-0.1Si) as shown in Fig. 5.3, albeit when aged to maximum hardness Fe-0.5Cu-0.2Si had a higher number density of total clusters than Fe-0.5Cu.

Compared to Fe-0.5Cu, in Fe-0.5Cu-0.2Si, the matrix Cu atoms seemed to prefer to segregate to the pre-existing clusters formed by ageing rather than form new clusters during the subsequent irradiation. This can be attributed to the high number density of the pre-existing clusters, which acted as effective sinks for Cu segregation.

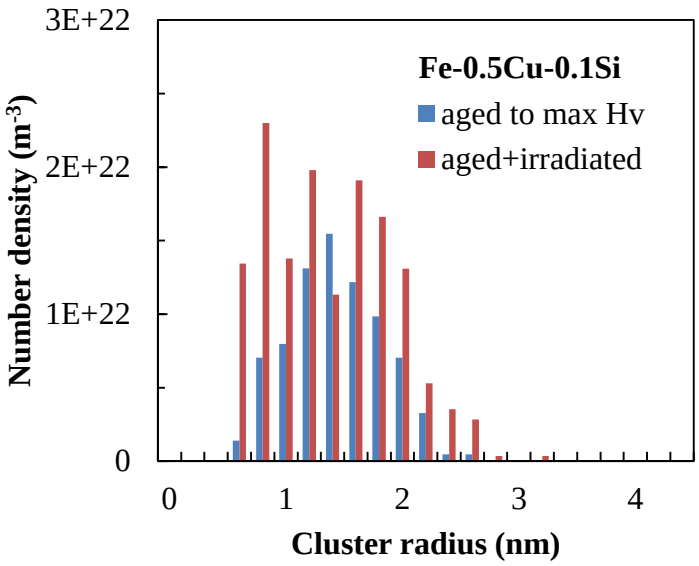

Fig. 5.1 Size distribution of the clusters in Fe-0.5Cu-0.1Si when aged to maximum hardness, and when aged plus irradiated

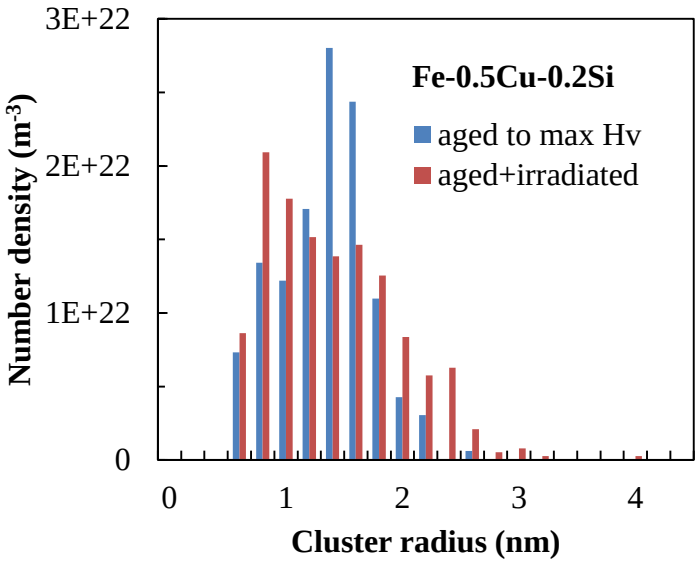

Fig. 5.2 Size distribution of the clusters in Fe-0.5Cu-0.2Si when aged to maximum hardness, and when aged plus irradiated

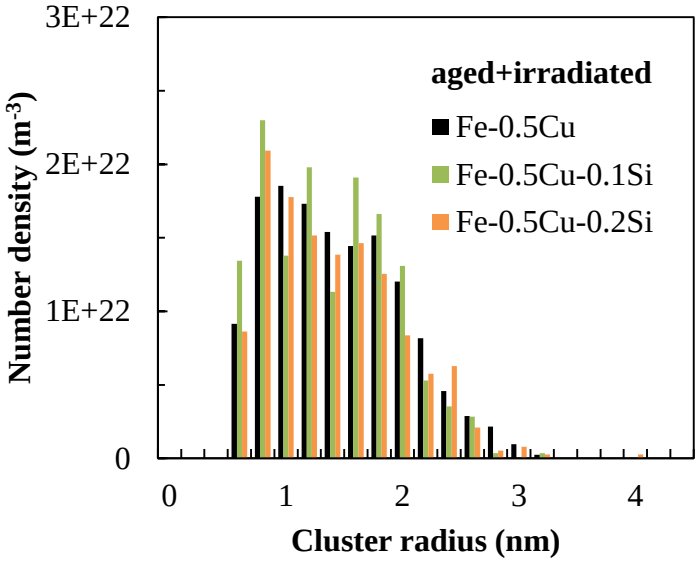

Fig. 5.3 Size distribution of the clusters in Fe-0.5Cu, Fe-0.5Cu-0.1Si, and Fe-0.5Cu-0.2Si when aged plus irradiated

The Si concentration distribution of the clusters in Fe-0.5Cu-0.1Si and Fe-0.5Cu-0.2Si, which is the cluster size dependence of the number of Si atoms in the cluster are detailed in Fig. 5.4. In the figure, each point indicates one cluster and the lines represent the mean Si concentrations in clusters. For all measured clusters, the maximum number of Si atoms in the cluster was less than 100. The small number of Si atoms measured by APT was accompanied with scattering around the mean Si concentrations in clusters. It is clear that the Si concentration in the clusters in the Fe-Cu-Si alloys was very low, especially when compared to the Ni and Mn concentrations in the clusters of the Fe-Cu-Ni and Fe-Cu-Ni-Mn alloys.

To evaluate quantitatively the level of Si concentration in the clusters, the enrichment factor of Si, defined as the ratio of Si concentration in clusters to the Si alloying content, was calculated, shown in Table 5.1. The enrichment factor of Si in the Fe-Cu-Si alloys was very low (< 2). Notably, when aged to maximum hardness, the Si concentration in the clusters was even almost equal to the Si alloying content, resulting in a Si enrichment factor of ~1.

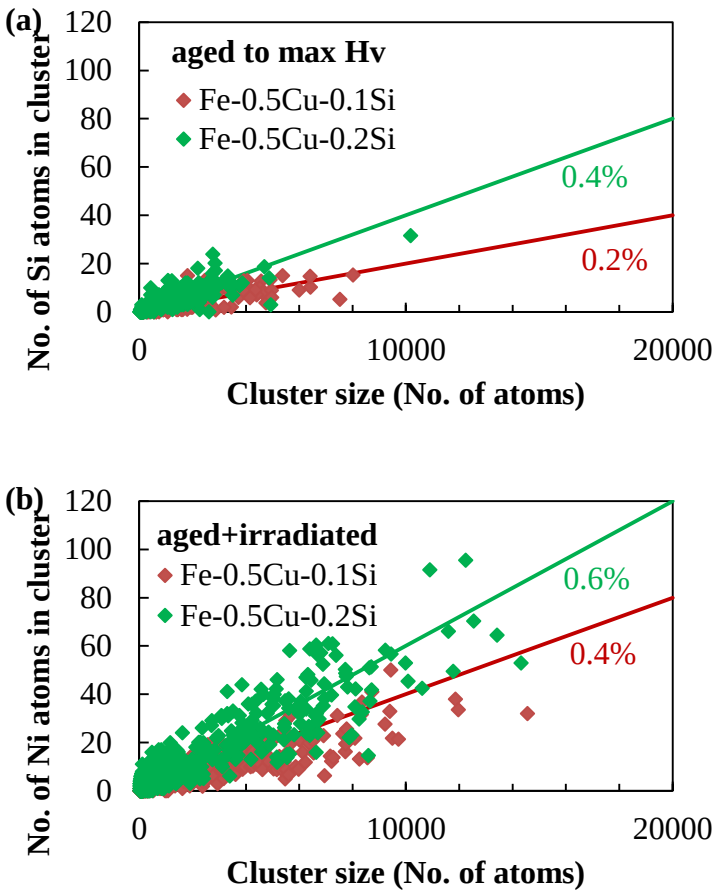

Fig. 5.4 Si concentration distribution of the clusters in Fe-0.5Cu-0.1Si and Fe-0.5Cu-0.2Si: (a) when aged to maximum hardness, and (b) when aged plus irradiated

Table 5.1 Enrichment factor of Si in Fe-0.5Cu-0.1Si and Fe-0.5Cu-0.2Si when aged to maximum hardness, and when aged plus irradiated

Alloy	Aged to max Hv	Aged+irradiated
Fe-0.5Cu-0.1Si	1.1	1.8
Fe-0.5Cu-0.2Si	1.1	1.6

5.2 Effect of Si

The addition of 0.1%Si to Fe-0.5Cu did not show any significant effect on the Cu clusters. On the other hand, when aged to maximum hardness, the addition of 0.2%Si increased the number density and decreased the radius of the clusters. The volume fraction of the clusters remained unchanged. According to a previous study, the clusters of an Fe-0.5Cu alloy aged to 200 h at 450 ^{o}C [5-1] exhibited a higher number density and a smaller radius than the clusters of Fe-0.5Cu when aged to maximum hardness (aged to 225 h at 450 ^{o}C). Both the alloys showed a similar volume fraction of the clusters. These results indicate that in Fe-0.5Cu, the coarsening of Cu clusters should occur during the ageing period of 200-225 h. The addition of 0.2%Si to Fe-0.5Cu was likely to suppress the coarsening of the Cu clusters. However, the addition of 0.2%Si to the alloys when aged plus irradiated had no significant effect on the Cu clusters, as previously shown by the size distribution curve of the clusters. The APT study by Liu et al. [5-1] also showed that the addition of 0.2%Si to Fe-0.5Cu had no clear effect on the Cu clusters under neutron irradiation.

The Si concentration in the clusters in the Fe-Cu-Si alloys was very low and was comparable to the Si alloying content. This suggests that the Si atoms hardly clustered with Cu. Previous equilibrium lattice Monte Carlo simulations which were parameterized purely on the basis of thermodynamic considerations, predicted that it is thermodynamically favorable for Si to segregate to the interface of a Cu cluster (Cu catalyzing mechanism) [5-2,3]. However, Si atoms hardly segregated to the Cu clusters in the ternary alloys Fe-Cu-Si under thermal ageing and even under the neutron irradiation which can largely accelerate the diffusion of Si atoms. In fact, the lattice Monte Carlo model in [5-2,3] reasonably predicted the contents of Cu, Ni, and Mn in the clusters

compared to experimental data, but it under-predicted about 50% of real Si content in the clusters. These observations appeared to imply that the segregation of Si to clusters may have other mechanisms, rather than the Cu catalyzing mechanism.

Previous analyses on surveillance specimens from Japanese pressurized water reactors [5-4,5,6] showed the mean atomic composition of the clusters was 6Cu-10Ni-6Mn-7Si, 2Cu-11Ni-5Mn-9Si, and 0Cu-12Ni-6Mn-12Si for 0.12wt.%Cu steels, 0.07wt.%Cu steels, and 0.04wt.%Cu steels, respectively, as mentioned in chapter 1. In the clusters, the Si concentration increased as the Cu concentration decreased, while the concentrations of Ni and Mn remained unchanged. The increase of Si concentration in the clusters may have been caused by complex mechanisms. To answer this question, at least the interactions of Si with other solute elements should be studied.

5.3 Summary

The comparison of the size distribution of the clusters in Fe-0.5Cu-0.1Si and Fe-0.5Cu-0.2Si with that in Fe-0.5Cu did not show evidence for Si to have effect on the Cu clusters, except that it might suppress the coarsening of the Cu clusters under thermal ageing. The Si concentration in the clusters in Fe-0.5Cu-0.1Si and Fe-0.5Cu-0.2Si was very low and was comparable to the Si alloying content, indicating that Si atoms hardly clustered with Cu.

References in chapter 5

[5-1] L. Liu, K. Nishida, K. Dohi, A. Nomoto, N. Soneda, K. Murakami, Z. Li, D. Chen, N. Sekimura, J. Nucl. Sci. Technol. 53 (2016) 1546–1553.

[5-2] G.R. Odette, B.D. Wirth, J. Nucl. Mater. 251 (1997) 157–171.

[5-3] C.L. Liu, G.R. Odette, B.D. Wirth, G.E. Lucas, Mater. Sci. Eng. A 238 (1997) 202–209.

[5-4] N. Soneda, K. Dohi, A. Nomoto, K. Nishida, S. Ishino, J. ASTM Int. 7 (2010) 1–20.

[5-5] N. Soneda, K. Dohi, A. Nomoto, K. Nishida, S. Ishino, Development of neutron irradiation embrittlement correlation of reactor pressure vessel materials of light water reactors, CRIEPI Report Q06019, 2007.

[5-6] K. Fukuya, K. Ohno, H. Nakata, S. Dumbill, J.M. Hyde, J. Nucl. Mater. 312 (2003) 163–173.

Chapter 6 Effect of Si on Ni-rich clusters under high-dose ion irradiation

This chapter describes the study of effect of Si on Ni-rich clusters using additional experiments of Cu-free model alloy and high-dose ion irradiation. Here, a high dose irradiation is desirable since the solute clusters in RPV steels and relevant model alloys which contain low Cu or no Cu have been experimentally observed typically at high dose levels, e.g. in [6-1,2,3,4]. The primary objective of this chapter is to understand whether Si can interact with Ni to form solute clusters at typical RPV temperature and the how is the enrichment of Si in these clusters.

6.1 Material and sample preparation

One model alloy that contains no Cu, Fe-1.0wt.%Ni-0.2wt.%Si was used in this study. The concentrations of Ni and Si in the model alloy were selected according to the chemical compositions of commonly used Japanese RPV steels [6-5]. This ternary alloy facilitates a proper study of the interaction between Ni and Si. The model alloy was solution annealed at 900 ^{o}C for 30 min and then water quenched.

For ion irradiation experiments, a sample block with a size of ~1×4×10 mm^3 was cut from the initial bulk material which has a cross section of 10×10 mm^2 through an intermediate cut into ~1×10×10 mm^3. The sample block should not be too thin to sustain the sample treatment and manipulation.

The sample surface (4×10 mm^2 surface which would receive ion irradiation) was first treated by mechanical polishing. In this stage, the sample surface was polished using polishing papers P320 and P1500 in sequence. The surface was then buff polished using

3μm diamond solution and 0.05 μm Al_2O_3 solution in sequence. Finally, a mirror-like surface can be obtained by this stage. It should be noted that the sample must always be thoroughly and carefully cleaned after each step to avoid the contaminations.

The mechanical polishing was followed by electrochemical polishing which can remove the surface deformation introduced by the mechanical preparation process. Fig. 6.1 illustrates the electrochemical polishing method used in this study. The electrolyte liquid was 95% CH_3COOH and 5% $HClO_4$. The electrochemical polishing was performed at ~12^oC where the temperature was monitored using a thermometer and controlled with the ice-water bath and an oscillator. During the electrochemical polishing, it is important to insert the sample into the electrolyte liquid with the long side (10 mm side) of the sample parallel to the surface of the electrolyte liquid rather than perpendicular to the liquid surface so as to uniformly remove the deformation surface. The surface condition after electrochemical polishing was confirmed under an optical microscope. About 20 μm thickness was removed by the electrochemical polishing in this study. Fig. 6.2 shows the surface of the sample after the electrochemical polishing observed by an optical microscope.

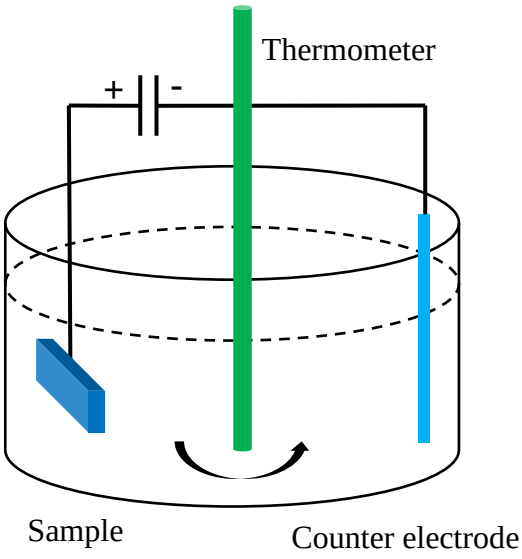

Fig. 6.1 Schematic diagram of electrochemical polishing

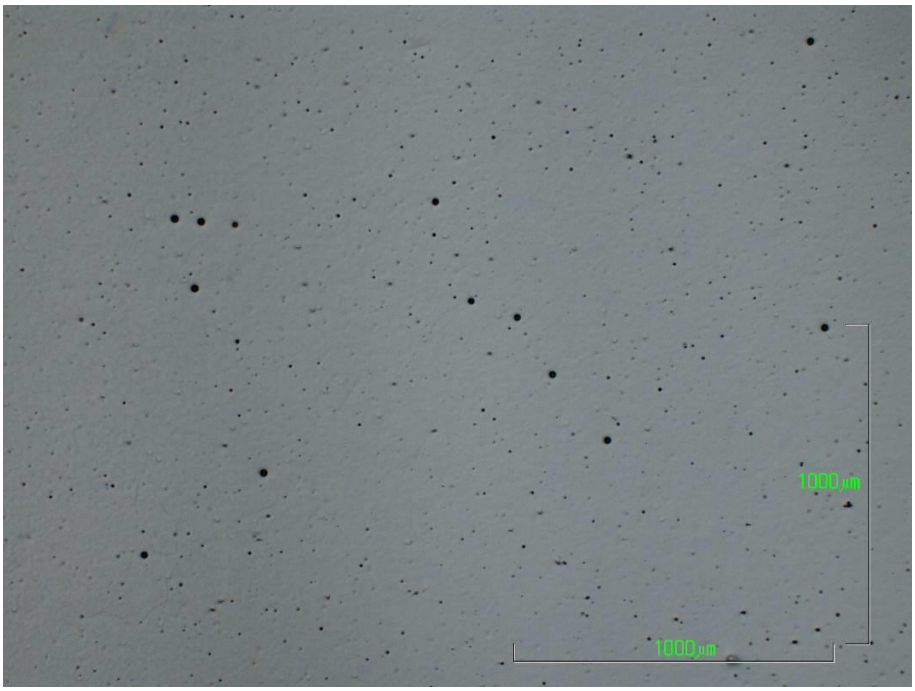

Fig. 6.2 The surface of the sample after electrochemical polishing under an optical microscope

6.2 Ion irradiation conditions

Ion irradiation with 2.8 MeV Fe^{2+} ions was carried out using a tandem-type accelerator installed at the High Fluence Irradiation Facility, The University of Tokyo (HIT) [6-6]. The irradiation temperature was 290 ^{o}C and the ion fluence was 2.32×10^{15} ions/cm^2. Fig. 6.3 illustrates the alloy sample fixed on the sample stage in HIT facility. During the irradiation, the temperature was monitored online using two thermal couples and controlled using the heater and the water cooling system. The ion beam profile was monitored every 30 min using a series of Faraday cups with an aperture diameter of 2 mm (coordinated 5×4). This is because that the monitoring of ion beam profile and the ion irradiation can't be performed simultaneously. The shape of the ion beam was controlled by magnetic lenses and steers and adjusted every 30 min accordingly. Then an approximately same ion flux during the irradiation and an approximately same ion fluence in a large irradiation area can be obtained.

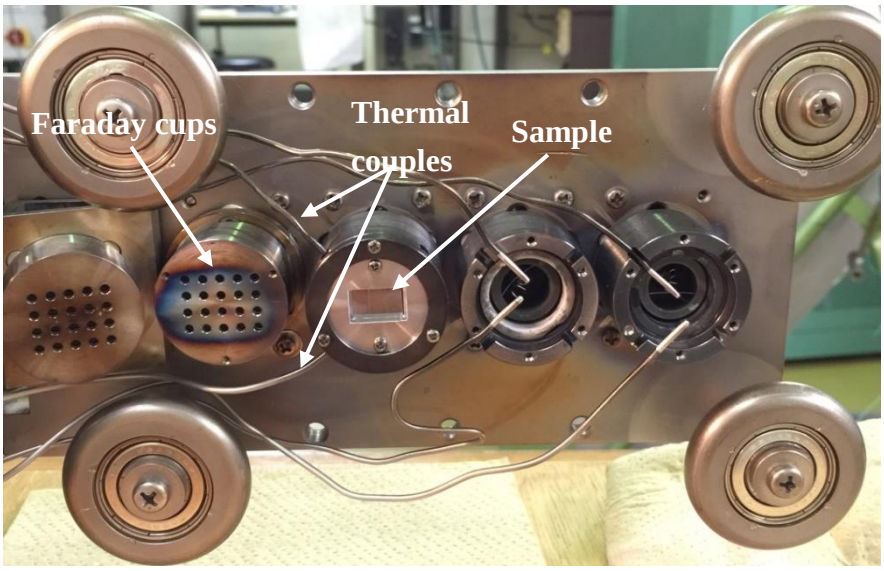

Fig. 6.3 The sample fixed on the stage for ion irradiation

The damage distribution associated with the ion irradiation was determined by using SRIM-2008 [6-7], as shown in Fig. 6.4. The calculation was conducted with a displacement energy of 40 eV and to be most consistent with the standard NRT dpa [6-8]. The peak of irradiation damage appeared at 800 nm and the calculated dose rate and dose (at the depth of damage peak) in this work was 2.65×10^{-4} dpa/s and 2.5 dpa, respectively.

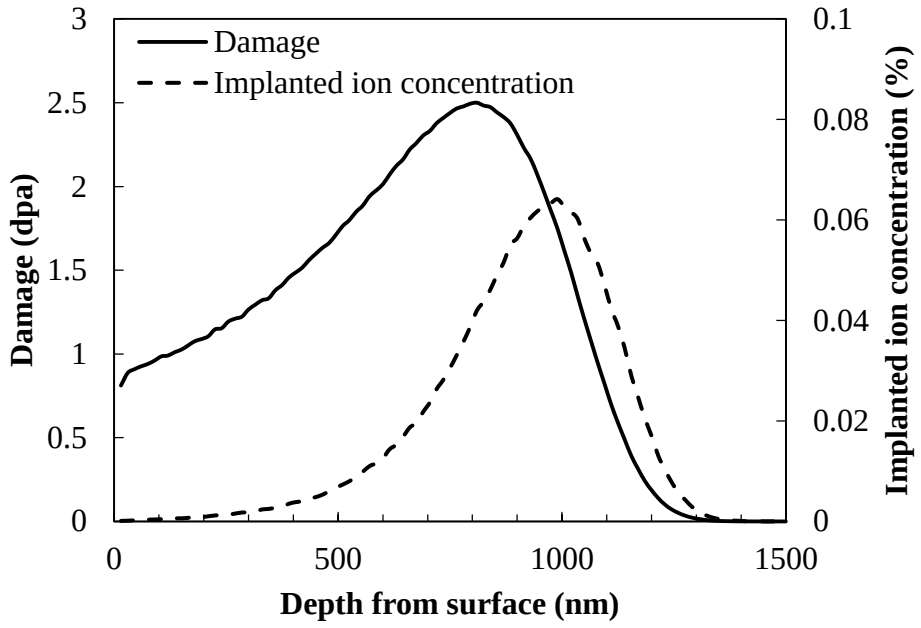

Fig. 6.4 Depth distribution of irradiation damage and implanted ion concentration by the SRIM code

6.3 Atom probe analysis

Considering the depth distribution of displacement damage introduced by ion irradiation in this study, the region of interest was the microstructure at a depth of 400 nm from the surface of the irradiated sample. This microstructure was characterized by APT.

6.3.1 Specimen preparation

The FIB use ions, usually Ga^+ ions, to interact with the sample surface and produce a secondary electron signal for imaging. The FIB can be used for milling when a high ion current is applied since the ion beam has the capability of sputtering away atoms. Deposition is one other fundamental capability of the FIB. Materials, such as tungsten, platinum and amorphous carbon, can be deposited on the sample surface as a protective layer when milling near sensitive areas.

In this study, the specimen preparation was performed using Zeiss NVision 40 FIB-SEM equipped at the Central Research Institute of Electric Power Industry which is shown in Fig. 6.5. The NVision 40 combines a high resolution scanning electron microscope (SEM) to the FIB. The e-beam images at an angle of 54^o to the Ga^+ ion beam. This dual-beam FIB instrument allows to image the sample in-situ (by the e-beam) when it is being milled (by the Ga^+ ion beam), which is important for preparing sit-specific specimens. The dual-beam FIB instrument is advantageous, also because that the imaging using the e-beam instead of the Ga^+ ion beam can reduce the Ga^+ ion implantation into the APT specimen and the induced damage in the preparation process.

Fig. 6.5 NVision 40 FIB-SEM used in the research

In order to prepare the site-specific APT specimens which can represent the microstructure at 400 nm depth, the FIB method was used to fabricate the specimens from 400 nm depth, of which the long axis from the apex was parallel to the surface of the irradiated sample. The manufacture procedure using FIB to prepare the specimens from certain depth from the sample surface, of which the long axis is perpendicular to the sample surface was presented in [6-9]. The manufacture procedure used in this study is a modified version of the procedure in [6-9].

Prior to the fabrication of the tips, tungsten was deposited on the region of interest up to a layer thickness of 600-1000 nm. This tungsten layer provided a protection for the region of interest from the Ga^+ ion implantation. It also acted as a counterpart of the sample when mounted on the atom probe post. To fabricate the tips, trenches were dug via milling

leaving a slice of the region of interest and then the sample was tilted to undercut the slice. The micro-manipulator was used to lift out the slice. Different from the procedure in [6-9], the slice was attached to a Nanomesh for a transit rather than directly attached to the atom probe post.

After the attachment of the lifted-out slice to the Nanomesh, the sample stage of the NVision 40 was taken out and then the Nanomesh was manually rotated 90 º. The stage was then reloaded into the NVision 40, and the rotated slice was transferred from the Nanomesh to the atom probe post via the micro-manipulator. The configuration of the slice tip on the atom probe post is illustrated in Fig. 6.6 (a), while Fig. 6.6 (b) illustrates the configuration without 90 º rotation of the Nanomesh.

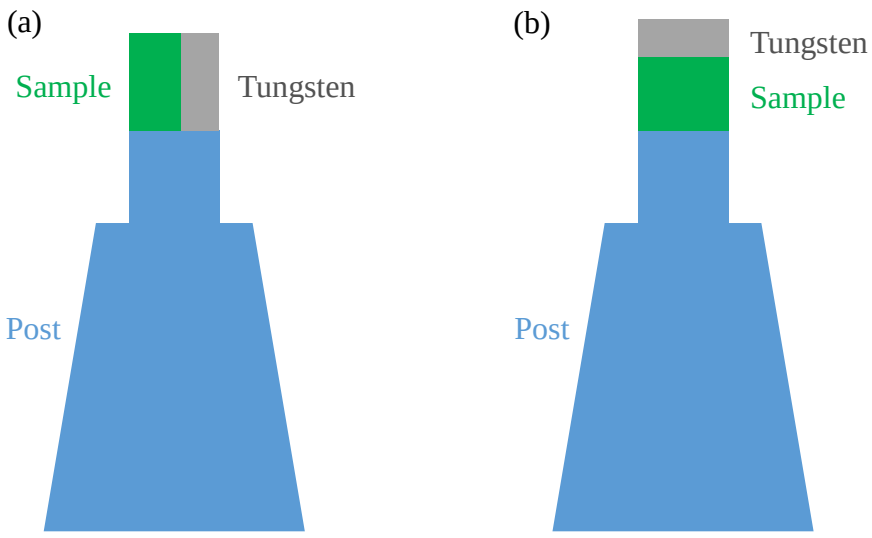

Fig. 6.6 Configurations of the slice tip on the atom probe post: (a) in this study, and (b) without 90 º rotation

The slice tip on the atom probe post was finally sharpened by annular milling. For the

annular milling, the radial pattern with an outer diameter slightly larger than that of the tip was used. The center of the radial pattern was located at 400 nm depth from the sample surface (the interface between the sample and the tungsten layer). Annular milling was performed under the 30 kV ion beam using several steps with progressively reduced outer and inner diameters until the required dimensions were reached. The affection of beam drift must be carefully eliminated during this stage for a successful specimen preparation. The specimen was finalized with the 10 kV ion beam to have an apex dimeter of ~100 nm. Fig. 6.7 shows a final atom probe specimen prepared by the FIB. The ion beam strategy for annular milling is critical for the FIB method, since it directly affects the shape and sharpness of the final specimen. The beam strategy interacts with the property of the material, and this determines the successful rate of the specimen preparation and the LEAP analysis.

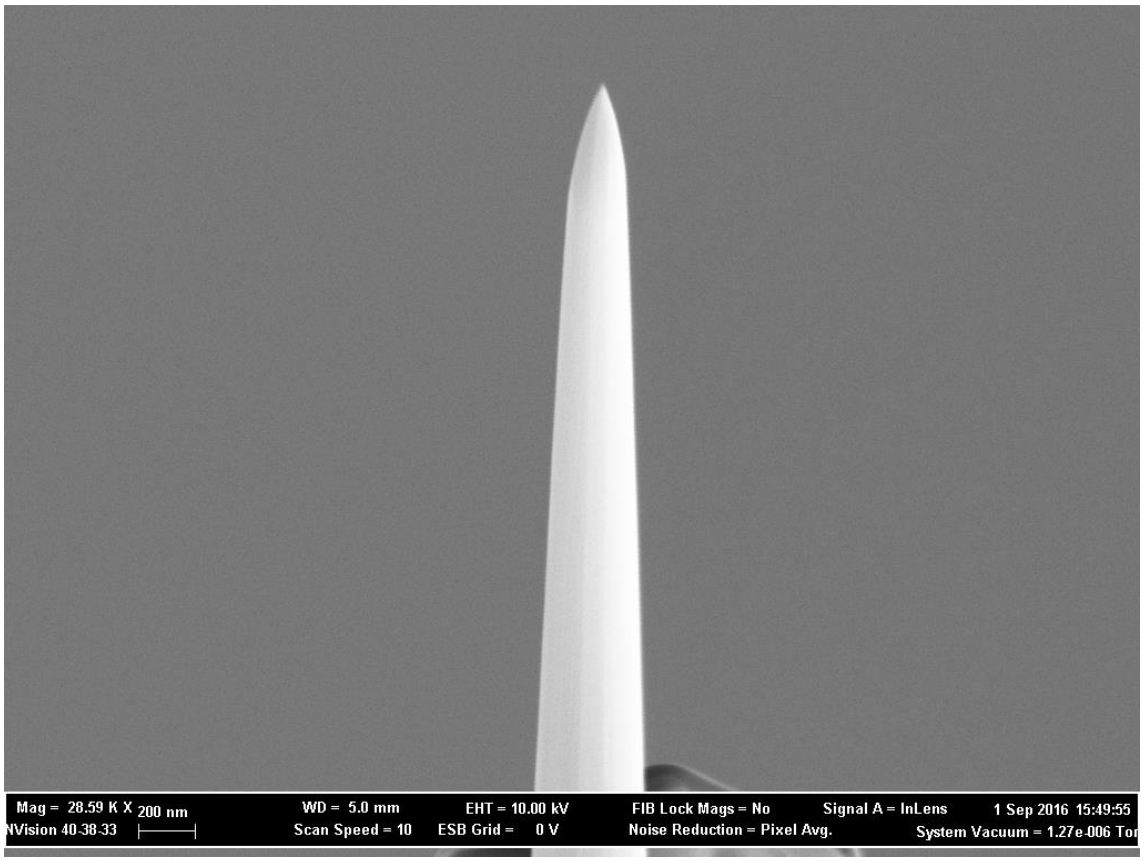

Fig. 6.7 Atom probe specimen prepared by FIB

6.3.2 LEAP analysis

The APT specimens prepared by the FIB method were analyzed using LEAP 3000XSi which is presented in Chapter 2 (Fig. 2.4). The LEAP analysis was performed in the voltage pulse mode. A specimen temperature of 40 K, a pulse repetition rate of 200 kHz, and a pulse fraction of 15% were used. All the experiments were carried out with a target evaporation rate in the range of 1-3% per pulse. This evaporation rate was lower than that used for the LEAP analysis in Chapter 2 to reduce the possibility of specimen rupture.

6.3.3 Data processing

In this study, the cluster analysis was performed using a recursive search algorithm (RSA) method [6-10,11], as in Chapter 2. Here, the core solute atoms, i.e., Ni and Si, which belong to the same cluster, are first searched within the separation of 0.4 nm. Then, any periphery atom such as an Fe atom within the separation of 0.4 nm from the core atoms is considered to belong to the cluster. Finally, the periphery atoms with less than three core atoms within a distance of 0.4 nm are removed. After all the clusters are found, any cluster that contains less than 20 core atoms is excluded from the analysis.

6.4 Results and discussion

Fig. 6.8 shows atom maps for irradiated Fe-1.0Ni-0.2Si. Numerous solute clusters (Ni-Si clusters) were observed in the analyzed volume of 85×85×131 nm^3. APT is an advanced microanalysis technique to characterize the solute clusters, but it can't give the evidence of the presence of point defects or point defect clusters. The association of solute clusters with the irradiation defect (such as dislocation line or loop) or the grain boundary can be identified when the distribution of the solute clusters take the shape of the defect or the grain boundary, for example in [6-12,13]. In atom maps shown by Fig. 6.8, these solute clusters did not take the shape of an extended dislocation or a grain boundary.

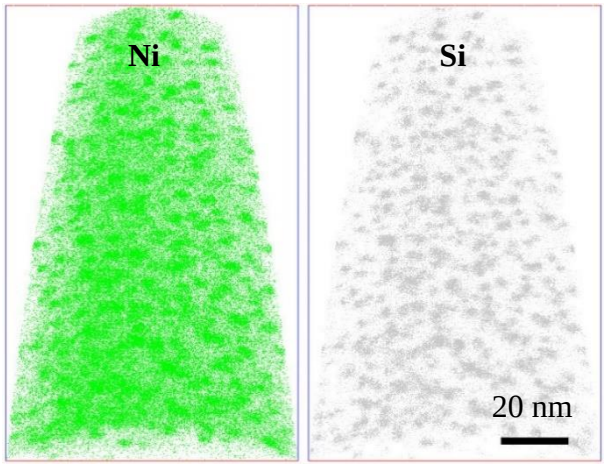

Fig. 6.8 Atom maps for irradiated Fe-1.0Ni-0.2Si

The cluster analysis based on the definition in the section 6.3.3 quantified the number density, volume fraction, mean radius and mean composition which are provided in Table 6.1. The ion irradiation produced high number density of clusters, the composition of which exhibits high enrichments of Si as well as Ni. Fig. 6.9 details the size dependence of the number of Ni atoms and the number of Si atoms in the clusters. In the figure, each point indicates one cluster (totally 593 clusters), and the lines represent the mean concentrations of Ni and Si in the clusters. Both Ni concentration in the clusters and Si concentration in the clusters were well distributed along their mean concentrations. This suggests that Ni atoms and Si atoms were both included in the clusters at roughly the same concentrations regardless of the cluster size.

Table 6.1 Number density, volume fraction, mean radius and mean composition of the clusters in irradiated Fe-1.0Ni-0.2Si

Number density	Volume fraction	Mean radius	Mean composition (at.%)		
(m^{-3})	(%)	(nm)	Ni	Si	Fe
1.42×10^{24}	1.56	1.28	24.5	15.8	41.9

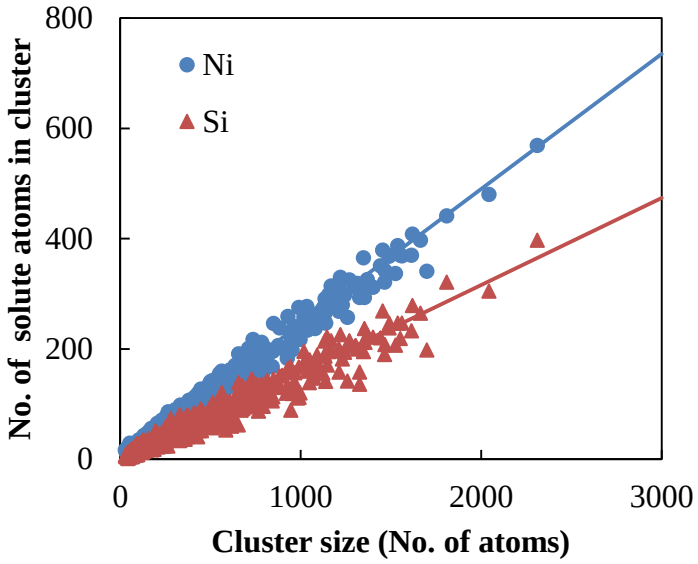

Fig. 6.9 Size dependence of the number of Ni atoms and the number of Si atoms in the clusters

Fig. 6.10 (a) describes the composition profile averaged over 5 solute clusters by the proxigram analysis, and Fig. 6.10 (b) is atom maps of one of these 5 clusters. The concentrations of Ni and Si in the clusters decreased simultaneously with the distance from cluster center. The morphology of the cluster in Fig. 6.10 (b) shows the combination between Ni atoms and Si atoms in the cluster. To quantitatively describe the relationship

between Ni distribution and Si distribution in the cluster, cluster Ni radius and cluster Si radius (the definition refers to the definition of cluster Ni radius or cluster Mn radius in Chapter 4) for each cluster was compared, as shown in Fig. 6.11. In the figure, each point represents one cluster. The cluster Ni radius was almost equal to the cluster Si radius, indicating correlated distributions of Ni and Si in the clusters. These observations indicate that Ni and Si should interact with each other during the formation of solute clusters. The ab initio calculations of solute-solute binding energies showed that Ni-Ni binding and Si-Si binding in α-Fe are both repulsive, whereas Ni-Si binding at first nearest neighbor is not repulsive, which was reported in [6-14]. This appears to agree with an interaction between Ni and Si.

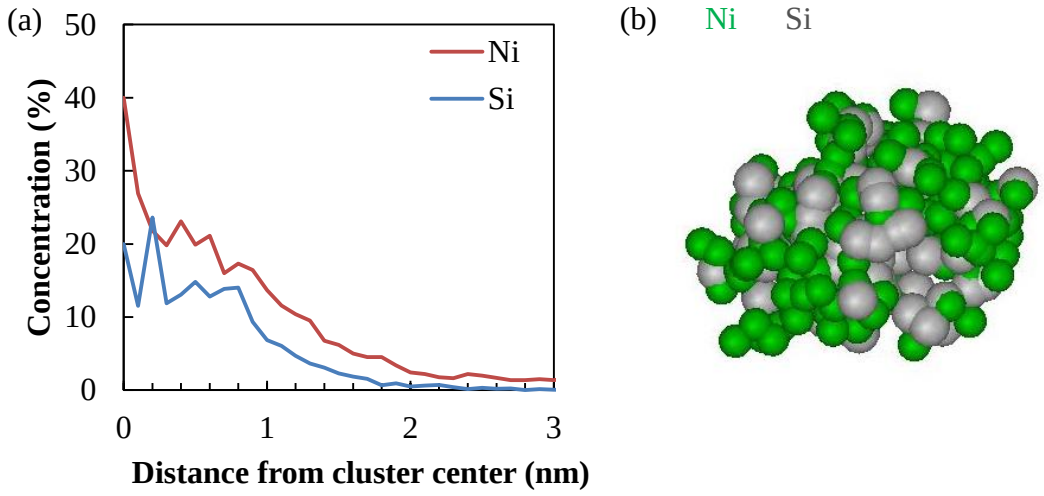

Fig. 6.10 (a) Proxigram averaged over 5 solute clusters in Fe-1.0Ni-0.2Si, and (b) atom maps of one of these 5 clusters

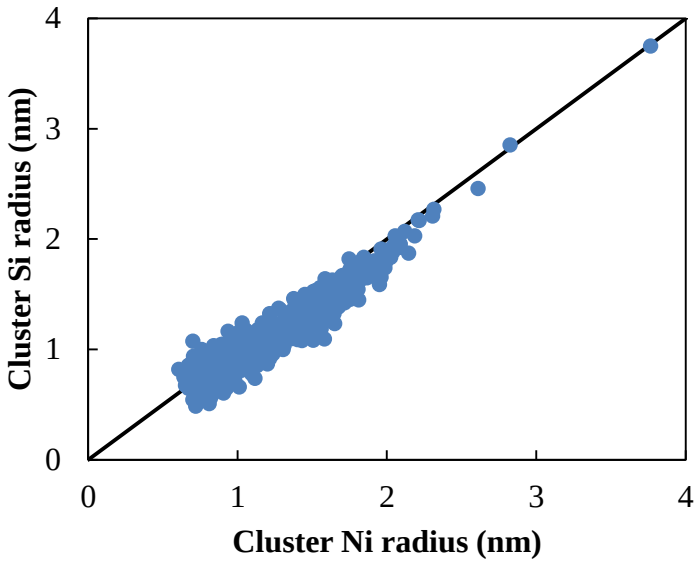

Fig. 6.11 Relationship between cluster Ni radius and cluster Si radius in Fe-1.0Ni-0.2Si (Solid line represents 1:1)

Solute clustering in a ferritic material in absence of Cu and Mn has never been reported before. Ni and Si both are soluble in α-Fe according to the phase diagram of binary alloys Fe-Ni and Fe-Si, respectively. Which can be the mechanisms for the formation of such high number density of Ni-Si clusters which were observed in the irradiated Fe-1.0Ni-0.2Si? The ab initio calculations have shown strong attractive binding of Ni atom or Si atom with the vacancy [6-15,16]. Besides, the positron annihilation experiments suggested the association of vacancy clusters with Ni atoms and the formation of vacancy-Si complexes under electron irradiation which produces damage in the form of single vacancies and self-interstitial atoms (SIAs) [6-17]. This also indicated the attractive interaction between Ni (and Si) and vacancy. When an attractive solute-vacancy interaction is present, the vacancy can drag the solute to diffuse in the same direction of the vacancy. The study using ab initio calculations combined with a self-consistent mean

field method showed that vacancy can drag Ni and Si in α-Fe [6-18]. The solute diffusion by vacancy drag can be strong under irradiation, thus increasing the collision frequency between Ni atoms and Si atoms. It is likely that the Ni-Si interaction then contributes to the formation of solute clusters.

Comments on the dose rate effects

Heavy ion irradiation enjoys the benefit of high dose rate which leads to the accumulation of high dose in short times. It can also be very efficient at producing dense cascades which are similar to those produced by neutrons [6-19]. The dose rate in this study was 2.65×10^{-4} dpa/s, several orders higher than that in the RPV of pressurized water reactors and boiling water reactors [6-20]. Whether the materials exhibit the same magnitude of damage under fast versus slow accumulation of the same dose level and if not, how their damages are different should be understood. The dose rate effect on the microstructure evolution is an important issue for the work using high dose rate experiments to simulate the behavior of the materials in the operating reactors.

The dose rate effect in RPV materials depends on the chemical composition of the material, the range of neutron dose, and the irradiation temperature [6-20,21,22]. For example, the Kinetic Monte Carlo simulations on the defect accumulation in α-Fe under neutron irradiation showed that the magnitude of the dose rate effect depended on the irradiation temperature and the dose rate effect was very strong at higher irradiation temperature, especially for the vacancy cluster formation [6-23]. The dose rate effect can mainly be attributed to two aspects. The first one is the competition between formation

and dissolution of defects which are thermally unstable at the irradiation temperature. The second one is its influence on solute diffusion and clustering.

It has been reported that large volume fraction of Ni-Mn-Si clusters were enhanced by lower dose rate [6-3,24]. The dose rate effect on these solute clusters may result from the intercascade interaction at high dose rates [6-23]. Therefore, it should be reasonable to conclude that Ni-Si clusters can also form in Fe-1.0Ni-0.2Si under the irradiation environment of RPV in the operating reactors.

6.5 Summary

To investigate the interaction between Ni and Si in ferritic alloy, ion irradiation experiment was carried out on one model alloy Fe-1.0Ni-0.2Si at 290 ^{o}C to 2.5 dpa by Fe-ions with the energy of 2.8 MeV. The microstructure of the irradiated sample was characterized using APT. A new manufacture procedure was established for using the FIB method to fabricate the APT specimens at 400 nm depth from the surface of the irradiated sample, of which the long axis from the apex was parallel to the sample surface. The APT results revealed the formation of high number density of Ni-Si clusters and the distribution of these clusters did not take the shape of an extended dislocation or a grain boundary. In the clusters, the Ni distribution was similar to the Si distribution, and the concentrations of Ni and Si decreased simultaneously with the distance from cluster center, which suggests the interaction between Ni and Si. Solute clustering in a ferritic material in absence of Cu and Mn has never been reported before. The Ni-Si interaction may contribute to the formation of these solute clusters.

References in chapter 6

[6-1] N. Soneda, K. Dohi, A. Nomoto, K. Nishida, S. Ishino, Development of neutron irradiation embrittlement correlation of reactor pressure vessel materials of light water reactors, CRIEPI Report Q06019, 2007.

[6-2] E. Meslin, B. Radiguet, P. Pareige, A. Barbu, J. Nucl. Mater. 399 (2010) 137–145.

[6-3] P.B. Wells, T. Yamamoto, B. Miller, T. Milot, J. Cole, Y. Wu, G.R. Odette, Acta Mater. 80 (2014) 205–219.

[6-4] P.D. Styman, J.M. Hyde, D. Parfitt, K. Wilford, M.G. Burke, C.A. English, P. Efsing, J. Nucl. Mater. 459 (2015) 127–134.

[6-5] N. Yamashita, M. Iwasaki, K. Dozaki, N. Soneda, J. Eng. Gas Turbines Power 132 (2010) 102919–102919.

[6-6] K. Murakami, T. Iwai, H. Abe, N. Sekimura, Nucl. Instrum. Methods Phys. Res. Sect. B Beam Interact. Mater. At. 381 (2016) 67–71.

[6-7] J.F. Ziegler, J.P. Biersack, in:, D.A. Bromley (Ed.), Treatise Heavy-Ion Sci., Springer US, 1985, pp. 93–129.

[6-8] R.E. Stoller, M.B. Toloczko, G.S. Was, A.G. Certain, S. Dwaraknath, F.A. Garner, Nucl. Instrum. Methods Phys. Res. Sect. B Beam Interact. Mater. At. 310 (2013) 75–80.

[6-9] K. Dohi, K. Nishida, A. Nomoto, N. Soneda, H. Watanabe, 3D atom probe observation of heavy ion irradiated model alloys for reactor pressure vessel steels, CRIEPI Report Q08029, 2009.

[6-10] N. Soneda, K. Dohi, K. Nishida, A. Nomoto, M. Tomimatsu, H. Matsuzawa, J. ASTM Int. 6 (2009) 1–16.

[6-11] J.M. Hyde, C.A. English, MRS Proc. 650 (2000).

[6-12] M.K. Miller, K.F. Russell, J. Nucl. Mater. 371 (2007) 145–160.

[6-13] P.D. Styman, J.M. Hyde, K. Wilford, A. Morley, G.D.W. Smith, Prog. Nucl. Energy 57 (2012) 86–92.

[6-14] L. Malerba, G.J. Ackland, C.S. Becquart, G. Bonny, C. Domain, S.L. Dudarev, C.-C. Fu, D. Hepburn, M.C. Marinica, P. Olsson, R.C. Pasianot, J.M. Raulot, F. Soisson, D. Terentyev, E. Vincent, F. Willaime, J. Nucl. Mater. 406 (2010) 7–18.

[6-15] E. Vincent, C.S. Becquart, C. Domain, Nucl. Instrum. Methods Phys. Res. Sect. B Beam Interact. Mater. At. 228 (2005) 137–141.

[6-16] O.I. Gorbatov, P.A. Korzhavyi, A.V. Ruban, B. Johansson, Y.N. Gornostyrev, J. Nucl. Mater. 419 (2011) 248–255.

[6-17] Y. Nagai, K. Takadate, Z. Tang, H. Ohkubo, H. Sunaga, H. Takizawa, M. Hasegawa, Phys. Rev. B 67 (2003) 224202.

[6-18] L. Messina, M. Nastar, T. Garnier, C. Domain, P. Olsson, Phys. Rev. B 90 (2014) 104203.

[6-19] G.S. Was, Fundamentals of Radiation Materials Science: Metals and Alloys, Springer, 2007.

[6-20] K. Fukuya, J. Nucl. Sci. Technol. 50 (2013) 213–254.

[6-21] G.R. Odette, T. Yamamoto, D. Klingensmith, Philos. Mag. 85 (2005) 779–797.

[6-22] A. Ballesteros, R. Ahlstrand, C. Bruynooghe, A. Chernobaeva, Y. Kevorkyan, D. Erak, D. Zurko, Prog. Nucl. Energy 53 (2011) 756–759.

[6-23] N. Soneda, S. Ishino, A. Takahashi, K. Dohi, J. Nucl. Mater. 323 (2003) 169–180.

[6-24] G.R. Odette, T. Yamamoto, B.D. Wirth, in:, MMM-2 Proc, Los Angeles, California, 2004.

Chapter 7 Contribution of solute effects to reactor pressure vessel embrittlement

7.1 Quantitative correlation between solute clusters and hardening

To forecast long-term integrity of RPV steels based on physical mechanisms, it requires an understanding of the nature of the microstructure under irradiation. Besides, it is also important to understand the relationship between microstructure and mechanical property. Here, the relationship between microstructure and hardening in the alloys Fe-Cu, Fe-Cu-Ni, Fe-Cu-Ni-Mn, and Fe-Cu-Si is focused on.

7.1.1 Alloy hardening

The hardness of the alloys, *H*v in neutron irradiation following thermal ageing experiments was evaluated using Vickers hardness tests and was represented using the mean (obtained through 12 indents), as listed in Table 7.1. Standard deviation of the hardness, which reflects the indent-to-indent variation, in the alloys was enlarged after the thermal ageing or after the neutron irradiation in most cases. Murakami et al. [7-1] observed the broadening of the hardness distribution in A533B RPV model alloys (some positions hardened more than others) after irradiation and concluded that this might result from the heterogeneity in initial alloy chemical composition, especially Cu.

Table 7.1 Hardness of the alloys in neutron irradiation following thermal ageing experiments

Alloy	Solution annealed	Aged to max Hv	Aged+irradiated
Fe-0.5Cu	76.4±2.1	119.8±2.9	157.9±3.7
Fe-0.5Cu-0.6Ni	88.4±3.1	123.2±2.2	163.8±4.2
Fe-0.5Cu-0.8Ni	89.6±3.1	125.3±3.7	162.3±6.0
Fe-0.5Cu-0.6Ni-1.4Mn	113.9±3.4	143.6±6.3	195.1±2.2
Fe-0.5Cu-0.8Ni-1.4Mn	115.6±3.6	145.7±4.9	208.0±3.6
Fe-0.5Cu-0.1Si	75.3±2.5	124.2±3.7	158.2±5.8
Fe-0.5Cu-0.2Si	81.5±2.1	122.7±2.5	160.6±3.8

The uncertainty is the standard deviation of the mean.

The hardening of the alloys, Δ*H*v was determined as

$$\Delta Hv^{aged\ to\ \max Hv} = Hv^{aged\ to\ \max Hv} - Hv^{solution\ annealed}$$
$$\Delta Hv^{aged+irradiated} = Hv^{aged+irradiated} - Hv^{solution\ annealed} \quad (7.1)$$

The relation between the hardening Δ*H*v and the alloy with varied chemical composition is shown in Fig. 7.1. The hardening after the thermal ageing or after the neutron irradiation depended primarily on the Cu content in the alloys. This can be because that the Cu content in these alloys are high.

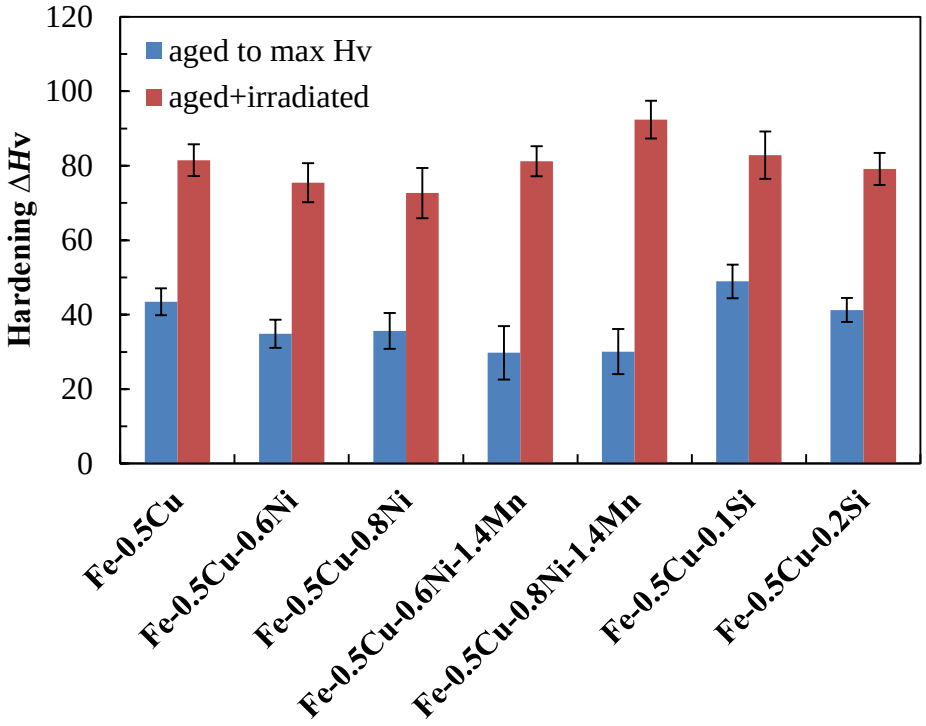

Fig. 7.1 Hardening of the alloys in neutron irradiation following thermal ageing experiments (Error bars refer to the standard deviation)

7.1.2 Hardening correlation with microstructure

The hardening of RPV materials is recognized to result mainly from two mechanisms, precipitation hardening and matrix hardening. The precipitation hardening is related to the formation of solute clusters, such as Cu-rich clusters and Ni-Mn-Si-rich clusters. In the studied alloys with 0.5%Cu, the precipitation hardening was caused by the Cu-rich clusters. The second mechanism, matrix hardening, is relevant to the matrix damage, such as dislocation loops. These defects can act as obstacles which impede dislocation movement and result in hardening.

7.1.2.1 Hardening by solute clusters

The hardening in RPV materials from Cu-rich clusters has generally been attributed to the difference in shear moduli between the solute clusters and the Fe matrix. For this case, the model that is most commonly used [7-2] is that of Russell and Brown [7-3]. Two alternate modulus hardening models can be found in the paper of Kelly [7-4]. In this thesis, the Russell-Brown model is employed. This model aims at the interaction between matrix slip dislocations and solute clusters which have lower elastic modulus than the matrix. The shear stress σ_{sy} is given by:

$$\sigma_{sy} = 0.8\frac{Gb}{L}\cos\frac{\phi_c}{2} \quad \phi_c \leq 100^{\circ}$$
$$\sigma_{sy} = \frac{Gb}{L}(\cos\frac{\phi_c}{2})^{3/2} \quad \phi_c \geq 100^{\circ} \tag{7.2}$$

where G is the shear modulus of the material, b is the Burgers vector for the dislocation, L is the obstacle spacing in the slip plane, and ϕ_c is the critical angle at which a dislocation can cut an obstacle. In the Fe matrix, G = 83 GPa, and b = 0.248 nm [7-5].

For a dislocation intersecting a spherical cluster, when the energy of the dislocation is lower in the cluster than it is in the matrix, the angle ϕ_c can be determined by the value when the dislocation is about to break away from the cluster [7-3]:

$$\phi_c = 2\sin^{-1}\frac{E_1}{E_2} \tag{7.3}$$

where E_1 is the energy per unit length of a dislocation in the cluster, and E_2 is the energy per unit length of a dislocation in the matrix. Russell and Brown [7-3] proposed the ratio E_1/E_2 as:

$$\frac{E_1}{E_2} = \frac{{E_1}^{\infty} \log\frac{r}{r_0}}{{E_2}^{\infty} \log\frac{R}{r_0}} + \frac{\log\frac{R}{r}}{\log\frac{R}{r_0}} \tag{7.4}$$

where E_1^{∞} and E_2^{∞} are the energy per unit length of a dislocation in infinite media, R is the outer cut-off radius used to calculate the energy of the dislocation, and r_0 is the inner cut-off radius. The ratio $E_1^{\infty}/E_2^{\infty}$ can be estimated to be equal to the ratio G_{SC}/G, where G_{SC} is the shear modulus of the cluster. R and r_0 are set to 2500b and 2.5b, respectively [7-3]. The particle spacing, L can be determined in terms of the volume fraction of cluster Vf and the mean radius of cluster r [7-3]:

$$L = \frac{1.77r}{\sqrt{Vf}} \tag{7.5}$$

In a polycrystal, the shear stress, σ_{sy} can be converted to the yield stress σ_y via the Taylor factor M:

$$\sigma_y = M\sigma_{sy} \tag{7.6}$$

where M has a value of 3.06 for bcc lattice [7-6]. In RPV materials, a linear relationship between the hardness Hv and the yield stress σ_y is generally admitted [7-2,7,8], and Hv can be converted to σ_y by [7-7]:

$$Hv = 0.41\sigma_y \tag{7.7}$$

Therefore, the hardening contribution of the solute clusters in studied alloys, $\Delta H\text{v}^{SC}$ can be given by

$$\Delta Hv^{SC} \approx 0.23\frac{MGb\sqrt{Vf}}{r}\left(1 - \frac{{E_1}^2}{{E_2}^2}\right)^{\frac{3}{4}} \tag{7.8}$$

where

$$\frac{E_1}{E_2} = \frac{G_{SC} \log\frac{r}{r_0}}{G \log\frac{R}{r_0}} + \frac{\log\frac{R}{r}}{\log\frac{R}{r_0}} \tag{7.9}$$

7.1.2.2 Hardening by matrix damage

Under the thermal ageing, the hardening contribution of the matrix damage in studied alloys can be simplified as zero. The matrix damage hardening under the neutron irradiation was approximated using the data of a RPV model alloy which contains no Cu, Fe-1.0Ni-0.2Si. The alloy Fe-1.0Ni-0.2Si received similar neutron irradiation with the studied alloys (a neutron fluence of 5.8×10^{18} n/cm^2 (E > 1 MeV) at an irradiation temperature of 290 ^{o}C and a flux of ~6×10^{12} n/cm^2/s), and its irradiation hardening obtained by Vickers hardness tests was 15.2. Buswell et al. [7-7] developed a fluence-hardening formula based on the data of low Cu RPV steels to define the hardening contribution of the matrix damage:

$$\Delta Hv^{MD} = 5.2\sqrt{\frac{\phi t}{10^{18}}} \tag{7.10}$$

where ϕt is the neutron fluence in units of n/cm^2 (E > 1 MeV). This gives a hardening of 12.5 at a neutron fluence of 5.8×10^{18} n/cm^2, which is at similar level with the irradiation hardening measured in Fe-1.0Ni-0.2Si.

Therefore, the hardening contribution of the matrix damage in studied alloys, ΔHv^{MD} was given by

$$\Delta Hv^{MD} \approx \begin{cases} 0 & \text{aged to max Hv} \\ 15.2 & \text{aged} + \text{irradiated} \end{cases} \tag{7.11}$$

7.1.2.3 Superposition of hardening mechanisms

In order to assess the total observed hardening of the material, the superposition law of the obstacles of different types is an important issue. In practice, this superposition law is

often taken as linear sum, or root-sum-square (RSS), or a combination of the linear sum and the RSS, although the actual superposition law depends on the obstacle strengths [7-2,9]. The linear sum superposition law assumes implicitly the independence of the different hardening mechanisms. In this analysis, the linear sum model was used for the approximation, which gives

$$\Delta Hv \approx \Delta Hv^{SC} + \Delta Hv^{MD} \tag{7.12}$$

Chaouadi and Gérard [7-10] studied the irradiation hardening of RPV materials and suggested the linear sum superposition law for the hardening of solute clusters and matrix damage.

7.1.2.4 Microstructure to hardening correlation

Fig. 7.2 shows the comparison of the measured hardening with that estimated from the microstructure (solute clusters and matrix damage). In the estimation of solute cluster hardening through Russell and Brown model, the shear modulus of the clusters, G_{SC} was estimated by fitting between the measured hardening and estimated hardening with the slope of 1:1, and calibrated on the basis of the type of the alloy. Table 7.2 provides the values of G_{SC} estimated in different alloys. The estimated G_{SC} values for Fe-Cu-Ni and Fe-Cu-Ni-Mn alloys were larger than that estimated for Fe-Cu alloys. This is consistent with the higher shear modulus of Ni and Mn elements than that of Cu as shown in Table 7.3 which were given by Friedel [7-5]. The addition of Ni to Fe-Cu binary alloy and the addition of Mn to Fe-Cu-Ni ternary alloys resulted in distinct change in the composition of solute clusters. The estimated G_{SC} value for Fe-Cu-Si alloys was similar with that estimated for Fe-Cu alloys, since the clusters formed in Fe-Cu-Si had very low concentration of Si and their composition was similar with that in Fe-Cu.

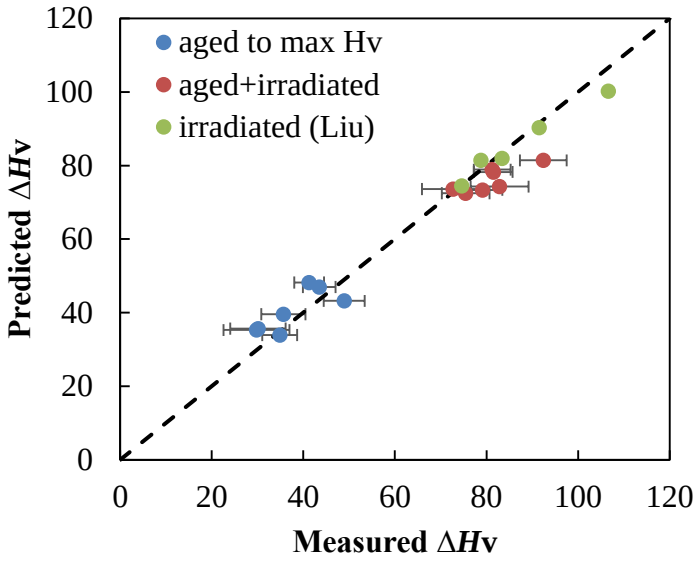

Fig. 7.2 Comparison of the measured hardening with that estimated from the microstructure (Error bars refer to the standard deviation)

Table 7.2 Shear modulus of solute clusters estimated in different alloys (GPa)

Fe-Cu alloys	Fe-Cu-Ni alloys	Fe-Cu-Ni-Mn alloys	Fe-Cu-Si alloys
62	66	69	62

Table 7.3 Shear modulus of the elements

Fe	Cu	Ni	Mn
83	49	75	81

A good agreement between the measured hardening and the estimated hardening was

observed. Liu et al. [7-11] studied similar alloys under neutron irradiation and their alloys were not pre-aged before the neutron irradiation. The hardening model in this work was then used to estimate the irradiation hardening of these alloys from their published microstructure data and this was also plotted in Fig. 7.2, which again shows good agreement between the measured and estimated hardening. These results demonstrate the quantitative correlation between the microstructure and mechanical property. It should be pointed out here that although the size distribution and composition of the clusters were not discussed here, the shape of the cluster size distribution and the cluster composition changed under the subsequent neutron irradiation, but the hardening was simply correlated with the microstructure through the above model and a good agreement was obtained. This needs further verification.

7.2 Role of solutes in long-term operation of reactor pressure vessel

Solute clusters are one dominant microstructure for RPV embrittlement. Even in the RPV steels irradiated to high fluences, pertinent to long-term operation, the increase of the transition temperature ΔT with fluence was still observed [7-12]. The microstructural analyses showed the increase of cluster radius and cluster number density with fluence, as mentioned in chapter 1 [7-12]. Therefore, for long-term operation of RPV, growth of existing clusters and formation of new clusters should be both considered. The present study focuses on effects of solute elements, including Ni, Mn, and Si, on formation and growth of solute clusters in RPV using neutron irradiation following thermal ageing

experiments and high dose ion irradiation experiment. Fig. 7.3 shows the brief summary of contribution to the knowledge of solute clustering by the present study.

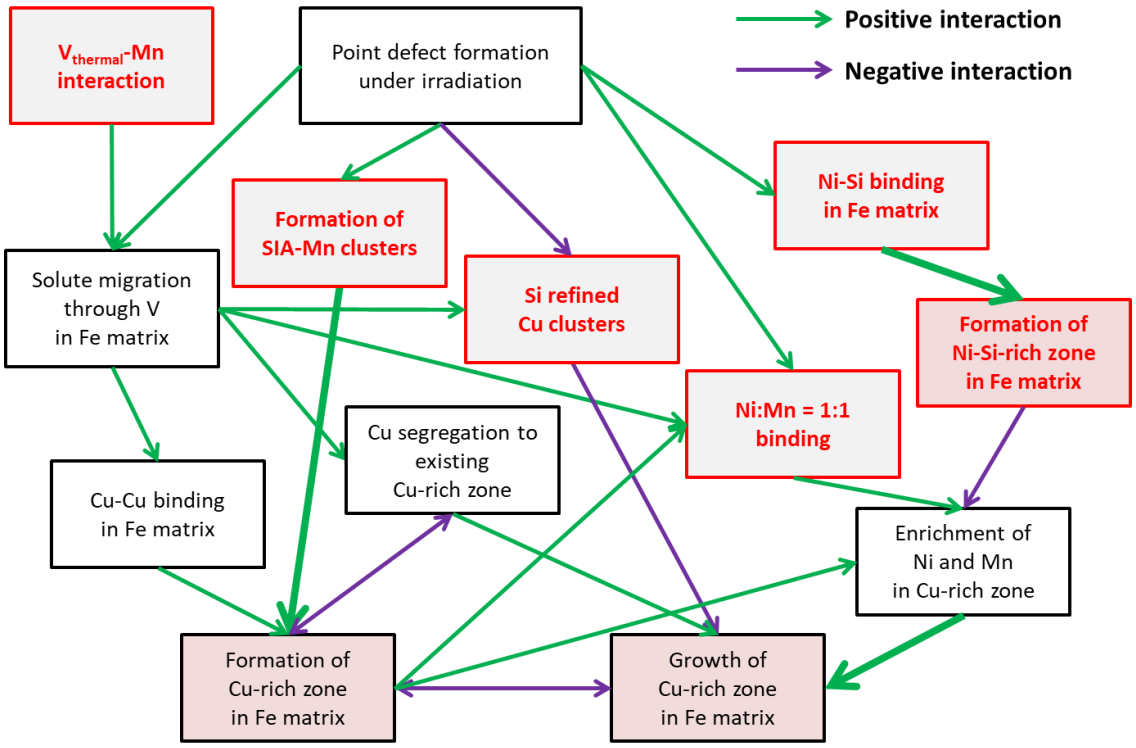

Fig. 7.3 Brief summary of contribution to the knowledge of solute clustering by the present study

In the present study, formation and growth of Cu-rich zone in Fe matrix (usually called Cu-rich clusters) are identified using the neutron irradiation following thermal ageing experiments. In addition, formation of Ni-Si-rich zone in Fe matrix (called Ni-Si clusters) is observed through high dose ion irradiation experiment. These three processes are shown in Fig. 7.3 using coloured boxes. They are the major sources of embrittlement. Formation of Cu-rich clusters and growth of Cu-rich clusters compete with each other, since formation of new Cu-rich clusters would reduce the amount of Cu segregation to

existing clusters. Besides, growth of Cu-rich clusters and formation of Ni-Si clusters may also compete with each other.

The new insights given by the present study are shown in Fig. 7.3 using the boxes with red outlines. As far as Mn is concerned, three interesting characteristics are found. First, the interaction between Mn and thermal vacancies can enhance solute migration through thermal vacancies in Fe matrix. Therefore, Cu-Cu binding in Fe matrix and formation of Cu-rich clusters would become rapid. The additional contribution of thermal vacancies to solute migration is a typical feature for very low flux irradiation, such as the irradiation on the inner wall of the BWR RPV. Second, Mn largely increased the number density of Cu-rich clusters during the neutron irradiation. This phenomenon is observed under irradiation and when Cu atoms exist in Fe matrix. Thermal vacancies do not contribute to this characteristic, as Mn did not change the number density of Cu-rich clusters under the thermal ageing. It has been considered to be caused by the formation of SIA-Mn clusters which can serve as nuclei of Cu-rich clusters. Third, the concentrations of Mn and Ni tend to exhibit 1:1 relationship in Cu-rich clusters. The 1:1 Ni-Mn relationship can be thermodynamically favoured. This thermodynamic relationship, probably 1:1 Ni-Mn binding, can enhance the enrichment of Ni and Mn in Cu-rich clusters which contributes to growth of Cu-rich clusters. The 1:1 Ni-Mn relationship and the enrichment of Ni and Mn in Cu-rich clusters can be driven by both thermal vacancies and irradiation produced point defects.

When it comes to Ni, two major characteristics are found. One is the 1:1 Ni-Mn binding. A higher Ni alloying content can lead to both higher Ni enrichment and higher Mn

enrichment in Cu-rich clusters. The other is the formation of Ni-Si clusters. The formation of Ni-Si clusters may result from the Ni-Si binding in Fe matrix and it is only observed in the highly irradiated material. Even though the fluence effect is not clarified in this study, the Ni-Si binding and the 1:1 Ni-Mn binding can interact and have combined effect on the solute enrichment and cluster composition.

As for Si, in addition to the formation of Ni-Si clusters, Si is likely to refine Cu clusters into small radius if the formation of Cu clusters is driven by thermal vacancies. But this Si effect was not recognized during neutron irradiation as the size distribution of clusters in Fe-Cu-Si and Fe-Cu became similar after the neutron irradiation.

Prior to representing the new findings in the present study into models, the status of current embrittlement correlation method in Japan, JEAC4201-2013 [7-13,14], is briefly reviewed: where solute effect, flux effect, and fluence effect have been considered, and how the method is different from the findings of this thesis. Current embrittlement correlation method consists of a set of mechanism-guided formulas, and the description of the formulas is detailed in chapter 1. The principal equations are reshown as below:

$$\frac{\partial C_{SC}}{\partial t} = \xi_9 \cdot \left(C_{Cu}^{avail} \cdot D_{Cu} \cdot \left(1 + \xi_8 \cdot C_{Ni}^{0}\right)\right)^2 + \xi_4 \cdot \left((C_{Cu}^{mat} + \xi_1) \cdot D_{Cu} + \xi_2 \right) \cdot C_{MD} \tag{7.13}$$

$$V_f = \left[\xi_{16} \cdot f(C_{Cu}^{mat}, C_{SC}) \cdot g\left(C_{Ni}^{0}\right) + h(\phi t)\right] \cdot C_{SC} \tag{7.14}$$

$$\Delta T_{SC} = \xi_{17} \cdot \sqrt{V_f} \tag{7.15}$$

$$D_{Cu} = D_{Cu}^{thermal} + D_{Cu}^{irrad} = D_{Cu}^{thermal} + \mu \cdot \phi^{\,\alpha} \tag{7.16}$$

In the method, flux effect is described as a difference of the diffusivity D_{Cu}, which depends on thermal vacancies and irradiation produced vacancies, as shown in equation

7.16. If the flux is very low, the contribution of thermal vacancies to formation and growth of solute clusters would become effective. The formulas can be separated into three parts: cluster formation, cluster growth, and microstructure to embrittlement correlation. In the part of cluster formation, Cu-Cu binding and Cu segregation to dislocation loops are both considered, as shown in equation 7.13. The first term is quite similar to the Cu-Cu binding model in present study, and the second term is also similar to the present study considering the SIA-Mn clusters. In both terms, flux effect and Ni effect are considered. Mn effect is not included in the method, whereas in this thesis Mn effect is found to be significant for the formation of solute clusters. The part of cluster growth is also considered using two terms, as shown in equation 7.14. One is the mean Cu amount in the cluster which reflects the competition between formation and growth of clusters. The other is cluster growth with fluence where flux effect is considered but no solute effect is included. Nonetheless, in this thesis, the 1:1 Ni-Mn thermodynamic relationship is found and it can enhance segregation of Ni and Mn to the clusters. In addition, the formation of Ni-Si clusters is not considered in current correlation method. In the part of microstructure to embrittlement correlation (see equation 7.15), current method uses a linear correlation between the square root of the cluster volume fraction and the transition temperature shift ΔT_{SC}, as a first order approximation.

Referring to the concept of current correlation method, the representation of the new findings is also separated into three parts: cluster formation, cluster growth, and cluster to embrittlement correlation. For the representation, flux effect is first discussed. It has been thought that flux takes effect through changing the amount of diffusion of Cu atoms [7-15,16], and flux effect depends on the flux range [7-17]. When the flux is as low as

like BWR irradiation conditions, the number of thermal vacancy jumps can reach the same magnitude as the number of irradiation-produced vacancy jumps [7-18].This type of flux effect, which means effective contribution of thermal vacancies to Cu diffusion, has been observed in surveillance materials of Japanese BWR RPVs [7-19]. To be specific, the RPV material with 0.24wt.%Cu from a capsule placed on the inner wall of the BWR RPV where the flux is as low as ~10^9 n/cm^2/s, showed higher number density and higher volume fraction of Cu-rich clusters than the archive RPV material irradiated in a material testing reactor (MTR) at a flux of 7×10^{11} n/cm^2/s. This is reflected as a linear sum of thermal vacancy contribution and irradiation-produced vacancy contribution in equation 7.16. In this thesis, it is found that the interaction between Mn and thermal vacancies can further enhance the contribution of thermal vacancies to Cu diffusion, leading to rapid formation of similar number density of clusters. These results indicate that the flux effect can be modelled using $D_{Cu}(\phi,C_{Mn})$, where ϕ is the flux which is used to describe the contribution of irradiation-produced vacancies, and C_{Mn} is the Mn content which is used to describe the interaction between thermal vacancies and Mn.

For the part of cluster formation, three features, Cu-Cu binding, Cu segregation to SIA-Mn clusters, and formation of Ni-Si clusters, are found to contribute to formation of solute clusters in present study. The Cu-Cu binding can be driven by both thermal vacancies and irradiation produced vacancies, which manifests flux effect. For Cu segregation to SIA-Mn clusters, the formation of SIA-Mn clusters would not be affected by thermal vacancies. Also, their formation should not increase linearly with time as it may compete with Mn segregation to existing solute clusters. The formation of Ni-Si clusters can be independent of Cu, but must depend on Ni, Si, and fluence. However, the present study is not sufficient

to clarify these effects and their priorities, which requires future study. Based on the above interpretation, the formation of solute clusters can be represented as:

$$\frac{\partial C_{SC}}{\partial t} = f_1(C_{Cu}, D_{Cu}) + f_2\left(C_{Cu}, C_{Mn}, {C_{SC}}^{-1}\right) + f_3(C_{Ni}, C_{Si}, \phi t) \tag{7.17}$$

where C_{SC} is the number density of solute clusters, C_{Cu} is the Cu content, C_{Ni} is the Ni content, C_{Si} is the Si content. The three functions f_1, f_2, and f_3, describe Cu-Cu binding, Cu segregation to SIA-Mn clusters, and formation of Ni-Si clusters, respectively. For the first term f_1, D_{Cu} is used to reflect the flux effect. For the second term f_2, C_{Mn} and C_{SC} are used to describe the formation of SIA-Mn clusters. The third term f_3 can depend on C_{Ni}, C_{Si}, and ϕt. The use of such many parameters also highlights the importance of the mathematical form of the formulas. For the Cu-Cu binding term f_1, a possible form can be proposed based on the kinetic theory which describes the precipitation in solid solution as a first order approximation [7-20]:

$$\begin{aligned}
&\frac{dC_n}{dt} = (\beta_{n-1}C_{n-1} - \alpha_n C_n) - (\beta_n C_n - \alpha_{n+1}C_{n+1}), \quad n \geq n^* \\
&\alpha_n = \frac{4\pi}{\Omega}(R_{n-1} + R_1)D_{\mathrm{Cu}} \exp\left(-\frac{F_{n-1} + \mathrm{F}_1 - \mathrm{F}_n}{\mathrm{k}T}\right) \\
&\beta_n = \frac{4\pi}{\Omega}(R_n + R_1)D_{\mathrm{Cu}}C_{\mathrm{Cu}}
\end{aligned} \tag{7.18}$$

where C_n is the number density of the cluster which contains n atoms, α_n is the emission rate of the cluster, β_n is the capture rate of the cluster, n*-1 designs the critical size for Cu nucleation, Ω is atomic volume, and F_n is Gibbs free energy of the cluster. Then, f_1 can be given by:

$$
\begin{aligned}
f_1 &= \frac{d}{dt}\sum_{n\geq n^*} C_n \\
&= \sum_{n\geq n^*} (\beta_{n-1}C_{n-1} - \alpha_n C_n - \beta_n C_n + \alpha_{n+1}C_{n+1}) \\
&= \left(\beta_{n^*-1}C_{n^*-1} + \sum_{n\geq n^*}\beta_n C_n\right) - \sum_{n\geq n^*}\alpha_n C_n - \sum_{n\geq n^*}\beta_n C_n + \left(\sum_{n\geq n^*}\alpha_n C_n - \alpha_{n^*}C_{n^*}\right) \\
&= \beta_{n^*-1}C_{n^*-1} - \alpha_{n^*}C_{n^*} \\
&\approx \beta_{n^*-1}C_{n^*-1} \\
&= \frac{4\pi}{\Omega}(R_{n^*-1} + R_1)D_{\mathrm{Cu}}C_{\mathrm{Cu}}C_{n^*-1}
\end{aligned}
\tag{7.19}
$$

If it is assumed that $C_{n^*\text{-}1}$ is proportional to C_{Cu}, then the form of f_1 can be proposed as:

$$f_1 = C \times D_{Cu}(\phi, C_{Mn}) \times {C_{Cu}}^2 \tag{7.20}$$

where C is the constant. For the term f_2 which describes Cu segregation to SIA-Mn clusters, since the formation of SIA-Mn clusters should be independent of Cu, its form can be proposed as:

$$f_2 = f_4(C_{\mathrm{Cu}}) \times f_5(C_{Mn}, {C_{SC}}^{-1}) \tag{7.21}$$

As for the part of cluster growth, the cluster growth has been believed to be due to solute segregation. The segregation of Cu atoms to existing solute clusters competes with the formation of new solute clusters. The segregation of Ni and Mn can be driven by both thermal vacancies and irradiation produced vacancies, which manifests the flux effect. The 1:1 Ni-Mn binding can further enhance the segregation of Ni and Mn. Therefore, the growth of solute clusters can be represented as:

$$V_f = \left[f_6(C_{Cu}, {C_{SC}}^{-1}) + f_7(\phi t, D_{Cu}, C_{Ni})\right] \times C_{SC} \tag{7.22}$$

where V_f is the volume fraction of solute clusters. The two functions f_6 and f_7, describe

the mean Cu amount in the cluster and the cluster growth with fluence, respectively. For the first term f_6, C_{SC} is used to describe the competition with cluster formation. For the second term f_7, D_{Cu} can reflect the flux effect, and C_{Ni} is used to consider the 1:1 Ni-Mn binding.

For the part of cluster to embrittlement correlation, the quantitative correlation between solute clusters and hardening based on the Russell-Brown model showed good agreement between predicted and measured hardening. This indicates that the transition temperature shift ΔT_{SC} can depend on the square root of the cluster volume fraction and the mean cluster radius. Therefore, the cluster to embrittlement correlation can be represented as:

$$\Delta T_{SC} = f_8\left(\frac{V_f}{C_{SC}}\right) \times \sqrt{V_f} \tag{7.23}$$

where V_f/C_{SC} is used to consider the mean cluster radius.

Based on the above discussion, the representation of the findings in the present study using models, is summarized as follows:

$$\begin{aligned} \frac{\partial C_{SC}}{\partial t} &= C \times D_{Cu}(\phi, C_{Mn}) \times {C_{Cu}}^2 + f_4(C_{\mathrm{Cu}}) \times f_5\left(C_{Mn}, {C_{SC}}^{-1}\right) + f_3(C_{Ni}, C_{Si}, \phi t) \\ V_f &= \left[f_6(C_{Cu}, {C_{SC}}^{-1}) + f_7(\phi t, D_{Cu}(\phi, C_{Mn}), C_{Ni})\right] \times C_{SC} \\ \Delta T_{SC} &= f_8\left(\frac{V_f}{C_{SC}}\right) \times \sqrt{V_f} \end{aligned} \tag{7.24}$$

To sophisticate the prediction models with such many parameters, it is necessary to develop microstructural database using APT. The consistency between the measured microstructural data and the predicted data can avoid the overfitting of the parameters.

Also, APT data are important for evaluating the available Mn content in RPV materials since this element is partially captured in the carbides. Some internal APT database have existed, such as CRIEPI database and UCSB microstructural database. The challenge is how to integrate the APT data obtained from different researchers. Here, a three-layer structure is proposed for the APT database, as shown in Fig. 7.4. Conventional database typically contain the information of material layer and cluster layer. The use of a tip layer provides the information of LEAP version, tip preparation method, cluster search algorithm, and tip composition. These factors can affect the APT data obtained in the cluster layer, thus being important for the integration of different database. To be specific, both straight-flight-path and energy-compensated versions of LEAP are in commercial use and their differences in detection efficiency and spectral resolution can be significant. For example, the detection efficiency of the straight-flight-path LEAP 3000XSi is about 58%, while the energy-compensated LEAP 3000XHR is about 37% [7-21]. As for the tip preparation method, electro-polishing and FIB milling are two prevalent methods. The electro-polished tip can be analyzed even up to a length of ~1000 nm, where the analyzed length of FIB tip is typically limited to 100-300 nm. Therefore, the cluster counts in electro-polished tip and FIB tip can be very different. Due to the small size of solute clusters in RPV materials, the cluster search algorithms also requires careful consideration. For example, the RSA method [7-12,22] and the maximum separation method [7-22] would search the same number density of clusters, but the cluster composition estimated by the RSA method can be different from that estimated by the envelope method [7-23].

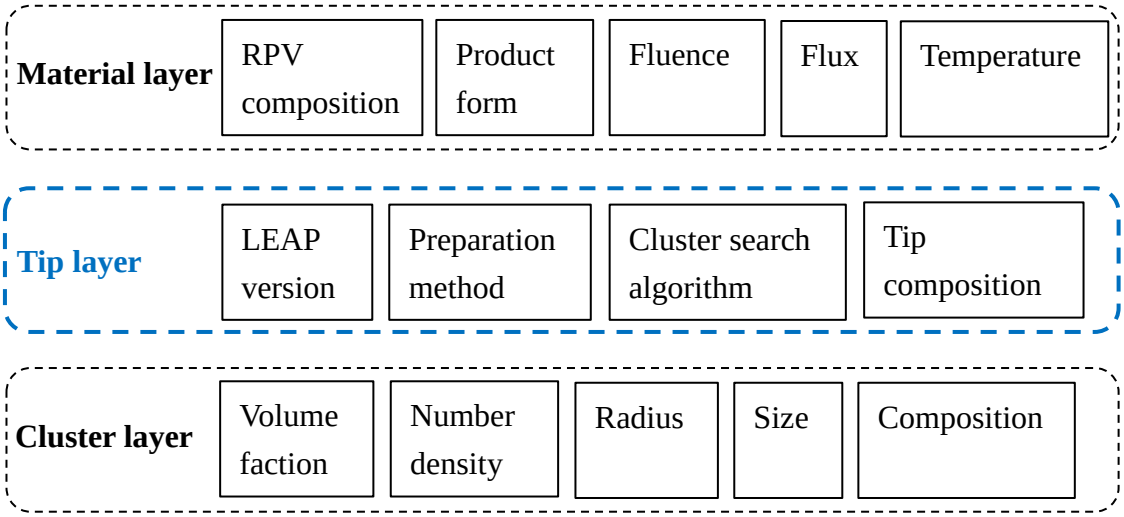

Fig. 7.4 Proposed structure for the APT database

In summary, the solute effects and the embrittlement prediction for long-term operation of RPV are discussed. The mechanisms found in the present thesis are represented using prediction formulas. To sophisticate the prediction formulas including fitting parameters, the APT database is proposed.

References in chapter 7

[7-1] K. Murakami, N. Sekimura, T. Iwai, H. Abe, J. Nucl. Sci. Technol. 53 (2016) 1061–1066.

[7-2] G.S. Was, Fundamentals of Radiation Materials Science: Metals and Alloys, Springer, 2007.

[7-3] K.C. Russell, L.M. Brown, Acta Metall. 20 (1972) 969–974.

[7-4] P.M. Kelly, Int. Metall. Rev. 18 (1973) 31–36.

[7-5] J. Friedel, Dislocations, Pergamon Press, 1964.

[7-6] R.E. Stoller, S.J. Zinkle, J. Nucl. Mater. 283 (2000) 349–352.

[7-7] J.T. Buswell, W.J. Phythian, R.J. McElroy, S. Dumbill, P.H.N. Ray, J. Mace, R.N. Sinclair, J. Nucl. Mater. 225 (1995) 196–214.

[7-8] J.T. Busby, M.C. Hash, G.S. Was, J. Nucl. Mater. 336 (2005) 267–278.

[7-9] G.R. Odette, G.E. Lucas, Radiat. Eff. Defects Solids 144 (1998) 189–231.

[7-10] R. Chaouadi, R. Gérard, J. Nucl. Mater. 345 (2005) 65–74.

[7-11] L. Liu, K. Nishida, K. Dohi, A. Nomoto, N. Soneda, K. Murakami, Z. Li, D. Chen, N. Sekimura, J. Nucl. Sci. Technol. 53 (2016) 1546–1553.

[7-12] N. Soneda, K. Dohi, K. Nishida, A. Nomoto, M. Tomimatsu, H. Matsuzawa, J. ASTM Int. 6 (2009) 1–16.

[7-13] N. Soneda, A. Nomoto, J. Eng. Gas Turbines Power 132 (2010) 102918-102918–9.

[7-14] N. Soneda, K. Nakashima, K. Nishida, K. Dohi, ASME Proc. (2013) V01BT01A047.

[7-15] S.B. Fisher, J.E. Harbottle, N. Aldridge, Phil Trans R Soc Lond A 315 (1985) 301–332.

[7-16] S.B. Fisher, J.T. Buswell, Int. J. Press. Vessels Pip. 27 (1987) 91–135.

[7-17] K. Fukuya, J. Nucl. Sci. Technol. 50 (2013) 213–254.

[7-18] N. Soneda, S. Ishino, A. Takahashi, K. Dohi, J. Nucl. Mater. 323 (2003) 169–180.

[7-19] N. Soneda, K. Dohi, A. Nomoto, K. Nishida, S. Ishino, J. ASTM Int. 7 (2010) 1–20.

[7-20] A. Barbu, E. Clouet, Solid State Phenom. 129 (2007) 51–58.

[7-21] D.J. Larson, T.J. Prosa, R.M. Ulfig, B.P. Geiser, T.F. Kelly, Local Electrode Atom Probe Tomography: A User's Guide, 2013 edition, Springer, New York, 2013.

[7-22] J.M. Hyde, C.A. English, MRS Proc. 650 (2000).

[7-23] M.K. Miller, Atom Probe Tomography: Analysis at the Atomic Level, Kluwer

Academic/Plenum Publishers, New York, 2000.

Chapter 8 Concluding remarks

In the present thesis, effects of solute elements, including Ni, Mn, and Si, on formation and growth of solute clusters in RPV were studied using neutron irradiation following thermal ageing experiments and high dose ion irradiation experiment. The model alloys Fe-Cu, Fe-Cu-Ni, Fe-Cu-Ni-Mn, and Fe-Cu-Si were used for neutron irradiation following thermal ageing experiments. Additionally, the model alloy Fe-Ni-Si was used for high dose ion irradiation experiment. Microstructural analyses of the alloys were conducted using APT. The major conclusions are summarized as follows:

(1) Mn is found to be critical for the formation of Cu-rich clusters. The addition of Mn to Fe-Cu-Ni reduced the ageing time required to achieve a similar microstructure of Cu-rich clusters from 225 to 90 h. This indicates that Mn can accelerate solute diffusion via thermal vacancies, thereby accelerating kinetic process of solute clustering. Different from thermal ageing condition, Mn significantly increased the number density of Cu-rich clusters during the neutron irradiation. It is suggested that Mn may bind with irradiation produced SIAs to form SIA-Mn clusters. These SIA-Mn clusters can server as the nuclei of Cu-rich clusters, thus enhancing the formation of Cu-rich clusters.

(2) A strong thermodynamic relationship between Ni and Mn is found. In the alloys Fe-Cu-Ni-Mn, an increase of Ni alloying content from 0.6% to 0.8% enhanced the Mn concentration in the clusters as well as the Ni concentration. The addition of Mn to Fe-Cu-Ni also enhanced the Ni concentration in the clusters. These results can suggest attractive binding between Ni and Mn, which would be a driving force for enhanced concentrations of Ni and Mn in the clusters. Moreover, for the alloys Fe-Cu-Ni-Mn with different Ni alloying contents, in the clusters the concentrations of Ni and Mn exhibited 1:1 relationship. The 1:1 Ni-Mn concentration relationship in

the clusters remained unchanged from thermal ageing condition to neutron irradiation condition. This indicates that the 1:1 Ni-Mn relationship, probably 1:1 Ni-Mn binding, can be thermodynamically favoured.

(3) Si atoms hardly cluster with Cu, but largely cluster with Ni. Si may refine Cu clusters into small radius under thermal ageing condition. Except this, evidence for Si to have effect on nucleation and growth of Cu clusters was not detected. Moreover, the Si concentration in the clusters in Fe-Cu-Si was very low and was comparable to the Si alloying content, indicating that Si atoms hardly cluster with Cu. However, Si should interact with Ni to form Ni-Si clusters, and their number density can reach as high as the order of 10^{24} m^{-3}.

(4) The role of solutes and the embrittlement prediction for long-term operation of RPV are discussed. The mechanisms identified in the present study are represented using prediction formulas. To sophisticate the prediction formulas including fitting parameters, APT database is proposed.

Solute clusters are one dominant microstructure for RPV embrittlement. Even in the RPV steels irradiated to high fluences, pertinent to long-term operation, both growth of existing clusters and formation of new clusters have been observed, which need careful consideration for accurate prediction of RPV embrittlement. The present study showed effects of Ni, Mn, and Si on formation and growth of solute clusters in a good manner, and threw light on the direction for future studies. The interesting issues suggested based on the present study include:

(1) Quantitative discussion on nucleation and growth of Cu-rich clusters. It is desired to quantitatively separate the group of grown clusters from the group of new clusters

after the neutron irradiation. This separation can facilitate the further understanding of how solute elements and irradiation affect the nucleation and growth of Cu-rich clusters. The statistical analysis of cluster size distribution using normal distribution fitting in chapter 4 showed a practice to categorize the clusters. However, the use of normal distribution or other probability distribution for fitting needs further consideration before the quantitative discussion. In addition, radiation induced segregation should be evaluated for quantifying the growth of pre-existing clusters.

(2) Further study on formation mechanisms of Ni-Si clusters. According to the literature, this study should be the first time to find the formation of Ni-Si clusters at RPV temperature in ferritic material in absence of Cu and Mn. However, the knowledge on the formation of Ni-Si clusters obtained in present study is limited. For future study, it is desired to clarify how Ni, Si, and fluence determine the formation of Ni-Si clusters and the relative significance of these effects.

(3) Study on effect of Si on the interaction of Ni and Mn. The present study finds the 1:1 Ni-Mn thermodynamic relationship. Also, Si is found to interact with Ni. The cluster composition in RPV steels may depends on the competition of these effects.

Appendix A

A.1 Number density, volume fraction, mean radius, and mean composition of the clusters in all alloys aged to maximum hardness

Alloy	Number density ($\times 10^{23}$ m^{-3})	Volume fraction ($\times 10^{-3}$)	Mean radius (nm)	Mean composition (at.%)				
				Cu	Si	Ni	Mn	Fe
Fe-0.5Cu	0.74 (0.63/0.84)	1.50 (1.05/2.11)	1.56	45.2	-	-	-	37.6
Fe-0.5Cu-0.6Ni	0.61 (0.56/0.74)	1.08 (0.81/1.15)	1.54	38.0	-	4.0	-	38.8
Fe-0.5Cu-0.8Ni	0.95 (0.90/1.13)	1.45 (1.24/1.76)	1.45	41.7	-	4.8	-	37.2
Fe-0.5Cu-0.6Ni-1.4Mn	0.81 (0.62/0.91)	1.48 (0.96/1.92)	1.50	36.5	-	4.1	4.1	40.0
Fe-0.5Cu-0.8Ni-1.4Mn	0.77 (0.59/0.90)	1.51 (1.18/1.72)	1.51	34.3	-	5.0	3.8	38.3
Fe-0.5Cu-0.1Si	0.78 (0.60/0.91)	1.24 (0.95/1.47)	1.45	44.5	0.2	-	-	36.7
Fe-0.5Cu-0.2Si	1.21 (1.17/1.36)	1.52 (1.24/1.98)	1.34	45.7	0.4	-	-	34.2

*Note that in the table, the values of number density and volume fraction are the weighted means of various measurements, where the weight for each measurement is the total number of atoms in the reconstructed tip. The minimum and maximum of various measurements are given in parenthesis. The mean radius and mean composition represent the mean of the radius and composition data collected from all measurements for various clusters. The mean radius refers to a simple mean, while the mean composition refers to a weighted mean, where the weight for each cluster is the total number of atoms contained in the cluster. This weighted mean approach for the cluster composition limits the contribution of very small clusters as their compositions may be skewed because of the small number of atoms in them.

A.2 Number density, volume fraction, mean radius, and mean composition of the clusters in all alloys first aged and then irradiated

Alloy	Number density ($\times10^{23}$ m^{-3})	Volume fraction ($\times10^{-3}$)	Mean radius (nm)	Mean composition (at.%)				
				Cu	Si	Ni	Mn	Fe
Fe-0.5Cu	1.39 (1.34/1.55)	2.66 (2.46/2.79)	1.46	48.4	-	-	-	36.7
Fe-0.5Cu-0.6Ni	1.58 (1.49/1.82)	3.06 (3.00/3.54)	1.47	39.6	-	6.4	-	37.4
Fe-0.5Cu-0.8Ni	1.71 (1.68/1.74)	3.16 (3.06/3.44)	1.44	39.6	-	6.6	-	36.5
Fe-0.5Cu-0.6Ni-1.4Mn	3.83 (3.63/4.56)	4.72 (3.83/5.07)	1.28	27.0	-	8.0	7.4	41.4
Fe-0.5Cu-0.8Ni-1.4Mn	4.21 (3.94/4.27)	5.11 (4.91/5.47)	1.30	24.5	-	10.2	9.4	41.1
Fe-0.5Cu-0.1Si	1.43 (1.31/1.55)	2.31 (2.15/2.36)	1.38	46.7	0.4	-	-	38.5
Fe-0.5Cu-0.2Si	1.28 (1.24/1.32)	2.24 (1.70/2.43)	1.40	47.0	0.6	-	-	35.3

*Note that the definitions of the values given in the table refer to A.1.

Acknowledgments

First, I would like to thank my supervisor, Prof. Naoto Sekimura for his great instruction over a period of three years. He has endeavored to help me grow as a researcher. He not only taught me skills for scientific research, but also continuously motivated me to do research in depth, which would benefit me forever. I am extremely grateful for this. I want also to thank the members of my committee, Dr. Kenji Dohi, Prof. Tatsuya Itoi, Prof. Hiroaki Abe and Prof. Takayuki Terai for their helpful advices throughout completing this thesis.

I am extremely grateful to Prof. Kenta Murakami. He taught me how to do a qualified research. He is always kind for any discussion. I would like to thank Prof. Tatsuya Itoi for his helpful suggestions throughout my PhD study. I would also like to thank Dr. Dongyue Chen for many helpful discussions.

I would like to thank Dr. Kenji Dohi, Mr. Kenji Nishida and Dr. Tomohiro Kobayashi in the Central Research Institute of Electric Power Industry (CRIEPI) for fruitful discussions with them and their continuous support and very kind help for my PhD research.

I would like to thank the other members in Sekimura-Itoi laboratory. I would like to thank CRIEPI staffs: Mr. Tanaka, Mr. Ikemoto, Mr. Miyamoto, Mr. Watanabe, Mr. Ukai, Mr. Itoigawa for their important help when preparing atom probe specimens and doing atom probe analysis. I would like to thank Mr. Omata, HIT staff for his help when using ion

irradiation facility.

I would like to thank Prof. Zhengcao Li in Tsinghua University for his helpful advices and encouragement throughout my PhD study.

Last but not the least, I would like to thank my family for supporting me spiritually throughout my life.

Publications and awards

Journal publications

1. L. Chen, Z. C. Li, H. Schut, N. Sekimura, Positron annihilation study of Fe-ion irradiated reactor pressure vessel model alloys, Journal of Physics: Conference Series 674 (2016) 012012.

2. L. Chen, K. Nishida, K. Murakami, T. Kobayashi, Z. C. Li, N. Sekimura, Evaluation of hardening under ion irradiation in reactor pressure vessel model alloys by nano-indentation techniques, E-Journal of Advanced Maintenance, accepted with minor revision.

3. L. Chen, K. Nishida, K. Murakami, L. Liu, T. Kobayashi, Z. C. Li, N. Sekimura, Effects of solute elements on microstructural evolution in Fe-based alloys during neutron irradiation following thermal ageing, Journal of Nuclear Materials, accepted with minor revision.

Conference presentations

1. L. Chen, Z. C. Li, H. Schut, N. Sekimura, K. Nishida, Positron annihilation Doppler broadening study of Fe-ion irradiated reactor pressure vessel model alloys, 18th meeting of the International Group on Radiation Damage Mechanisms in Pressure Vessel Steels (IGRDM18), November 2014, Miyazaki, Japan, Oral presentation.

2. L. Chen, K. Nishida, K. Murakami, K. Dohi, L. Liu, N. Sekimura, Evaluation of the relationship between microstructure and hardness in neutron irradiated reactor pressure vessel model alloys following thermal ageing, Annual Meeting of Atomic Energy Society of Japan, March 2016, Sendai, Japan, Oral presentation.

3. L. Chen, K. Nishida, K. Dohi, K. Murakami, Z. C. Li, L. Liu, D. Y. Chen, N. Sekimura, Effects of solutes on microstructure evolution and hardening in neutron irradiated reactor pressure vessel model alloys following thermal ageing, 19th meeting of the International Group on Radiation Damage Mechanisms in Pressure

Vessel Steels (IGRDM19), April 2016, Asheville, the United States, Oral presentation.

4. L. Chen, K. Nishida, K. Murakami, T. Kobayashi, L. Liu, N. Sekimura, Effects of solutes on microstructure evolution in neutron irradiated reactor pressure vessel model alloys following thermal ageing, Autumn Annual Meeting of The Japan Institute of Metals and Materials, September 2016, Osaka, Japan, Oral presentation.

5. L. Chen, K. Nishida, K. Murakami, T. Kobayashi, Z. C. Li, N. Sekimura, Evaluation of hardening under ion irradiation in reactor pressure vessel model alloys by nano-indentation techniques, 3rd International Conference on Maintenance Science and Technology (ICMST 2016), November 2016, Shenzhen, China, Oral presentation.

6. L. Chen, Safety and assessment of material systems for nuclear power plants, The World Association of Nuclear Operators (WANO) Tokyo Centre 2016 Plant Manager's Meeting, November 2016, Tokyo, Japan, Invited presentation.

Awards

1. Inaugural WANO Nuclear Safety Scholarship winner, The World Association of Nuclear Operators (WANO), Ceremony: WANO Biennial General Meeting, October 2015, Toronto, Canada.